Non–equilibrium ionization of metals in 3D numerical models of the solar atmosphere

by

Kosovare Olluri

Submitted
in partial fulfilment of the requirements
for the degree of

Philosophiæ Doctor

Institute of Theoretical Astrophysics
Faculty of Mathematics and Natural Sciences
University of Oslo
Oslo, Norway
November, 2013

Series of dissertations submitted to the
Faculty of Mathematics and Natural Sciences, University of Oslo
No. 1457

ISSN 1501-7710

Cover: Inger Sandved Anfinsen.
Printed in Norway: AIT Oslo AS.

Produced in co-operation with Akademika Publishing.
The thesis is produced by Akademika Publishing merely in connection with the thesis defence. Kindly direct all inquiries regarding the thesis to the copyright holder or the unit which grants the doctorate.

Acknowledgements

I would like to begin by thanking my supervisor Boris Gudiksen, because he suggested this interesting project and always believed that I was strong enough to handle any obstacle I encountered through this fantastic journey.

Viggo Hansteen also deserves praise, because he has been a counselor, a mentor and a friend since the beginning, first as my supervisor on my master thesis and then as the co-supervisor for the Ph.D.

A special thanks to my dear friend Nicolaas, who encouraged me to apply for the Ph.D position to such a high degree that he more or less wrote the application for me (well, mostly because he wanted me to finish so I could attend a party!). I can not forget Nuno, Juan, Jorrit and Eamon, as well as my awesome office mates Sandro, Dan, Patrick and Bhavna, who made my time at the institute a great pleasure. They have always been there for me through thick and thin, both at some of the greatest times but also at moments of utter despair.

I would also like to take the opportunity to thank my dearest friend Mathilde, for still remaining my friend, after years of negligence, and at times even divided by continents. I could always count on you to keep me grounded and completely take my mind of my troubles, with lots of laughs and a new adventure ready at hand. Some of the same things can be said about my old flatmates Lillian and Tuva, and the newcomer Kristin. Being scientists themselves, they always understood and supported me. I will always cherish the time in Torggata, and never forget the epic parties we had, so many fun memories!! You really are the *bestest* friends.

I want to thank my parents Selman and Shpresa, brother Besart, my sisters Arta and Shkurta, and my brother in law Afrim, for standing by me through all the years before and during my Ph.D. I am truly grateful for being blessed with such a loving and supporting family. And of course my dearest niece Elona, for being a light in my life always.

Finally, thank you Thomas, for putting up with me during my crazy times, in both the positive and the negative sense. For you are really the only one that have truly witnessed this entire journey. I am grateful to have you by my side.

It ain't about how hard you can hit. Its about how hard you can get hit, and how much you can take, and keep moving forward.

Rocky Balboa - From The Rocky Balboa Movie.

Preface

The motivation for the topic is the quite simple, the computational power to do what we want to do is finally here. Non–equilibrium ionization in the solar atmosphere have been studied by many before us. This is because the observational evidence for the disruption of the ionization equilibrium have been well known for at least the last two decades. We know that there are large velocities is the solar atmosphere, and we know that there is a very steep temperature gradient in the solar atmosphere – the solar transition region. It has also been revealed that the chromosphere and transition region are very dynamic layers of the solar atmosphere, characterized by timescales shorter than the ionization equilibrium timescales of many ions dominating emission in these regions. The fast changes in the properties of the atmosphere combined with the long ionization and recombination times can lead these ions to being found far from their equilibrium temperatures. The spectral lines of these ions can therefore not be expected to reflect information about the local quantities such as the density or temperature. Spectroscopic investigations therefore need to be interpreted with the help of numerical modeling in order to produce reliable results. Previous modeling efforts have been done in 1D, but 1D models have many free parameters, and they can typically only be used to test the possible importance of a physical effect. Their conclusions have intrinsic uncertainties, and can not be used to disprove or verify the importance of the physical effect in the actual 3D atmosphere. Due to the fast changes in the properties of the atmosphere, long ionization- and recombination times can lead these ions to being found far from their equilibrium temperatures. The recent development in computing technology and atmospheric modeling makes it possible to study the full 3D effect of non–equilibrium ionization. With the solar atmosphere model Bifrost, we have a 3D platform for calculating and following the ionization degree of important ions radiating in this highly dynamical region of the solar atmosphere.

I will begin with a tale of the Sun, and a general description of the solar interior and atmosphere in the first chapter. In chapter 2 I will give you an introduction of spectroscopy and spectral line formation. I have dedicated a section to timescales in the solar atmosphere, because they are important when spectral lines are used for diagnostics of the solar atmosphere. There

is a vast set of assumptions on the physical conditions of the emitting region made a priory to spectroscopic diagnostics, and a review of these is presented in the last section of chapter 2. The 3rd chapter is dedicated to a review of the information of the transition region obtained from observations, and a presentation of some remaining puzzles regarding these. Solar atmospheric modeling has been done for decades, and the 4th chapter is dedicated to a review of previous modeling efforts, with focus on previous 1D models which have included non–equilibrium ionization. In chapter 5 I present the work done for this dissertation. The three-dimensional solar atmosphere code Bifrost is presented, together with a description of the developed non–equilibrium ionization solver I have made as part of the Ph.D work. I discuss the assumptions I have made and the numerical methods I have used for the implementation of the rate equations. The Ph.D work has accumulated to three papers, two of them are published in international peer–reviewed journals, while the third paper was submitted to The Astrophysical Journal on the 27th of November 2013. A summary of each paper is included in the last section of chapter 5.

Contents

Part I

Introduction

Chapter 1

The Sun

The Sun has had an important place in astronomy and to the human race for a long time, because of its prominent position in the sky. About 2450 years ago Anaxagoras suggested that the Sun is not all that special. He postulated that the Sun was a star like all the others, claiming that all stars were fireballs, and reasoned that the proximity of the Sun made it possible for us to feel its heat. However, his ideas were so controversial compared to the general believes at the time that he was sentenced to lifetime in prison. 200 years later, Aristarchus of Samos put the Sun in the center with the planets revolving around it, and was the first to postulate what later became known as the heliocentric cosmology. This theory was lost in time, until Copernicus repostulated it 1545. The philosopher Giordano Bruno extrapolated this idea: If the Earth is merely a planet revolving around the Sun, then the Sun could not be any more special either. It must be a star like the other stars seen on the night sky, in the infinite universe of stars, with equal number of worlds as ours. But his controversial ideas were met with brutality by the church, and he was burned at the stake for his blasphemous thoughts.

The idea had been sowed, and only needed to go through Galilei, Kepler, Huygens and Newton, to Friedrick Bessel, who in 1838 was the first one to calculate the distance to another star - finding it to be enormous! Some years before, Joseph Fraunhofer had discovered that stars display different spectra, and together this led to hundreds of thousands of distance calculations of other stars, and by the aid of spectroscopy to their respective surface temperatures and chemical compositions. Finally, the proof was here that the Sun is a star.

In the beginning of the 20th century stellar data was collected and tabulated according to spectral class and surface temperature, which was later expanded to include luminosity. This was pictorially presented in what is today known as the Hertzprung–Russel (HR) diagram, presented in figure 1.

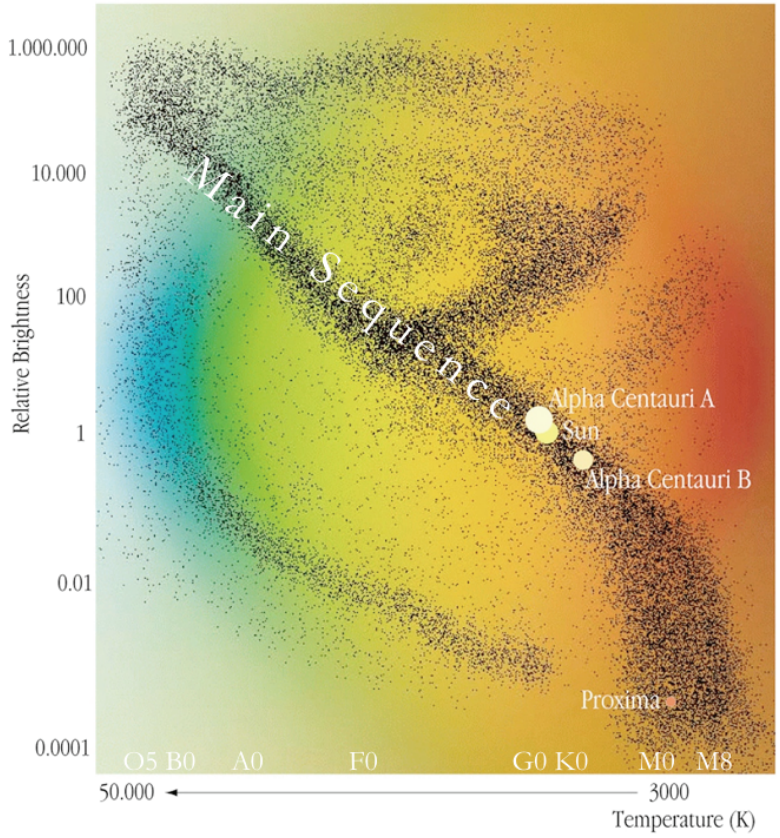

Figure 1.1: The location of Alpha Centauri A and B, Proxima Centauri and the Sun in the Hertzsprung-Russell (HR) diagram. Credit: ESO

The Sun has a surface brightness of 1 with a surface temperature of ca. 5000 K, and is therefore classified as a G2 star. The HR diagram shows the lifetime evolution of stars, where the Sun is a part of the main sequence, which means that it is fully developed as a star, and is in a stable phase of hydrogen burning. The Sun is currently halfway through its life, and will exit the main sequence in about 5 billion years.

90 % of the visible stars are in the main sequence stage of their lives, and by studying and understudying the Sun, we can gain insight into the properties of most of the stars in our Universe.

1.1 The solar interior

The Sun is in hydrostatic equilibrium. The gravitational force pulls matter inwards. The pressure therefore increases inward toward the core, and a pressure force is created by the internal pressure, balancing gravity exactly.

The Sun's energy output comes from the conversion of matter into energy, which is mostly done through fusion of hydrogen to helium in its core. The core extents to approximately one tenth of the solar radius where the temperature is 15.5×10^6K.

Photons created by nuclear fusion in the core lose energy by repeatedly colliding with and being scattered by particles on their journey to the solar surface, an odyssey that typically takes 170 000 years. The process is called radiative transport, and is the dominant means of energy flow in the radiative zone, which extends from the core out to 70% of the solar radius. At this point, the temperature gradient becomes superadiabatic, and convection becomes the more efficient means of energy transport in the remaining 30% of the solar interior, called the convective zone. Here, hot gas convects up to the solar surface, where photons are emitted into space, resulting in a cooling of the gas, which thereby settles back into the Sun. A schematic overview of the Sun, including the interior, is presented in figure 1.2.

Another important notion of the Sun is the rotation and consequently the magnetic field. The Sun exhibits differential rotation, where equatorial regions rotate with a period of 27 days, with increasing period toward the poles, which rotate with periods of 34 days. The differential rotation has been measured to continue inward through the convective zone. The rotation from the inner core through the radiative zone, on the other hand, is close to uniform. The shearing motions between these two layers is said to be the origin of the magnetic fields on the Sun, where electric currents generated by the flow of ionized plasma produce magnetic fields that extend out to the solar surface.

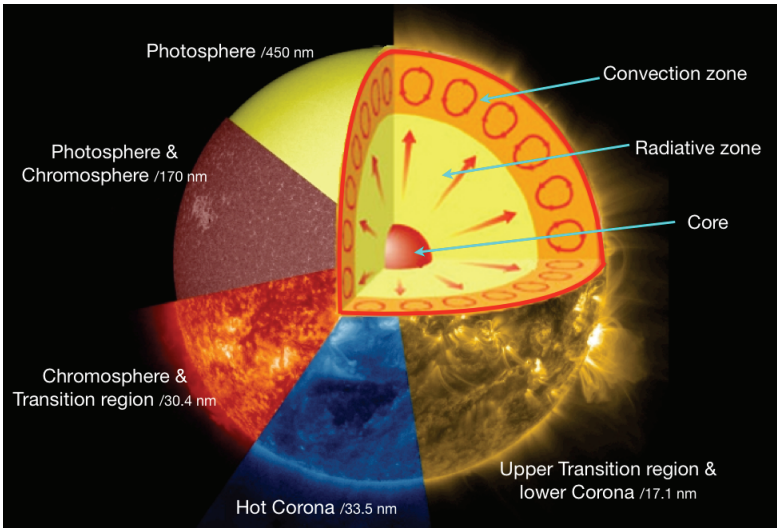

Figure 1.2: Schematic overview of the Sun showing a cartoon of the solar interior structure together with actual images of the different layers of the solar atmosphere observed with the Solar Dynamics Observatory. The figure was produced using images created with the ESA and NASA funded Helioviewer Project.

1.2 The solar atmosphere

This chapter consists of a short summary of the solar atmosphere, which is the only region of the Sun that we can directly observe. The typical characteristics of the main regions of the atmosphere will be presented, namely the photosphere, chromosphere, transition region and corona.

1.2.1 The photosphere

The photosphere is the region of the Sun that is usually referred to as the solar surface, where the atmosphere becomes optically thin, and the photons escape the solar interior and travel unimpeded through space with a range of energies and hence wavelength. The Sun's visible spectrum therefore results in a curve that closely resembles that of a black body curve, with a peak at 5800 K, which is referred as the surface temperature of the Sun. The temperature drops with increasing height, to a minimum of 4400 K, defining the end of the photosphere, resulting in a spatial extent of about 500 km.

When studying the visible radiation of the Sun, we see a structure called granulation. This effect is caused by the underlying convection, and it is basically the convective cells that we observe. The bright regions show the hot pockets of gas emerging, which cool down and fall back into the interior, seen as the dark lanes surrounding the granules. The granular cells typically have a spatial extent of 0.7 to 1.5 Mm and lifetime of 5 to 15 minutes.

Magnetic flux emerges with the convective cells, but because the pressure force is much larger than the magnetic force in the photosphere, the magnetic flux is swept to the cell walls, and one observes what is known as bright points, where the magnetic flux gets concentrated in the intergranular lanes and the magnetic force dominate. This power struggle is described by the plasma β, defined as the ratio between the gas pressure, P, and the magnetic pressure, given by

$$\beta = \frac{\mathrm{P}}{\mathrm{B}^2/2\mu_0} \tag{1.1}$$

where B and μ_0 are the magnetic field and the magnetic permeably in vacuum. Even though the overall photosphere is considered to be in a high β regime, the magnetic field can be highly variable. One example where the magnetic force is very strong is in sunspots, which have a lifetime ranging from a few days to several months. These features are therefore continually appearing on the solar disk and decay relatively quickly, however they appear to follow a 22 year cycle caused by the Sun's global dynamo, which affects the latitude and density of the sunspot phenomenon.

1.2.2 The chromosphere

The chromosphere is defined as the region starting at the temperature minimum and extending up to temperatures of some 20 000 K. The spatial extent can vary quite severely; in general defined as an envelope of 2000 km surrounding the photosphere, but can shoot up to the Mm range in what is known as spicules, cold jets of matter shooting up to coronal heights. The chromosphere is by far the most complicated part of the solar atmosphere and is poorly understood. Furthermore, its influence and importance in understanding the overlaying regions of the solar atmosphere has therefore for the greater part been underestimated.

The chromosphere is highly dynamic, and shocks and waves in various forms are present at all times, where the dynamical timescales are very small. The chromosphere deviates strongly from local thermodynamical equilibrium and radiative transfer therefore has to be included when studying the origins of both emission and absorption lines of the region. Additionally, the chromosphere is partially ionized and non–equilibrium ionization effects due to the short dynamical timescales of the region play an important role.

The dominant gas pressure at the base of the chromosphere gradually loses its power, changing to a magnetic pressure dominated region halfway through the chromosphere, *i.e.* going from a high β regime to a low β regime. This means that in the upper part of the chromosphere the magnetic pressure controls the dynamical behaviour of the matter. Magnetic flux tubes rooted deep in the photosphere expand with height as a result of this shift and form what is known as the magnetic canopy.

In the chromosphere the mass density falls from $10^{-4}\mathrm{kg\,m^{-3}}$ to $10^{-11}\mathrm{kg\,m^{-3}}$, and the pressure decreases from $10^{2}\mathrm{Pa}$ to $10^{-2}\mathrm{Pa}$, and extreme amounts of energy are therefore required to increase the temperature by an order of magnitude, as is observed. However, the mechanism behind the chromospheric heating is poorly understood.

1.2.3 The transition region

Just above the chromosphere lies the transition region, where the temperature rises by 2 orders of magnitude, from $2 \times 10^{4}\mathrm{K}$ to $10^{6}\mathrm{K}$, over only a few hundred kilometers. Since the transition region is in a low β regime, the spatial extent of it is dominated by the dynamical behavior of the gas, and is not a well-defined layer at a particular altitude. Regions of high magnetic field concentration would therefore have a transition region located at deeper layers of the atmosphere, and vice versa.

While an energy release in the chromosphere goes into ionizing hydrogen or increasing the temperature, hydrogen is fully ionized in the transition region and radiative losses from hydrogen are inefficient. Energy release therefore goes into raising the temperature, until thermal heat conduction

($\propto T^{5/2}\nabla_{\parallel}T$) becomes strong enough to balance the energy input, and we reach the corona.

Helium becomes fully ionized in the lower transition region, whereas heavier elements ionize with the increasing temperature. With the decreasing gas density the atmosphere goes from being optically thick in the upper chromosphere to optically thin in the transition region, and the spectra of the transition region is dominated by emission lines of heavier elements, emitting in the ultraviolet (UV) part of the electromagnetic spectrum.

The dynamical timescales of the region are very small, where the ionization and recombination times of the heavier elements increase due to the rapid changes in temperature.

The transition region is an important region of the solar atmosphere because it plays a crucial role in transferring energy and momentum from the photosphere and chromosphere to the corona.

1.2.4 The corona and beyond

Above the transition region lies the corona, where temperatures vary from 1 million kelvin to several million kelvin, depending on the dynamics and the activity observed. The high temperatures of the corona has puzzled scientists since their discovery (Grotrian, 1939; Edlén, 1943), because thermodynamical principles state that the temperature should drop with distance from the energy source, which in this case is the solar core. It follows that some other energy source therefore has to be responsible for the heating of the corona. The convective motions in the photosphere have enough mechanical energy to heat the corona, however the mechanism required to transport and dissipate the energy is still a mystery. Alfén waves, a buffeting of magnetic flux tubes called AC-heating, have been invoked as a possible mechanism to transport magneto-convective energy upwards along magnetic field lines. Another possibility is the constant shuffling of the magnetic flux tubes by the convection in the photosphere, causing a buildup of stress in the magnetic field. This consequently leads up to episodically release of energy through reconnection called nano-flares, and what is known as a DC-heating mechanism.

Typical signatures of the corona are the huge loops observed in EUV and X-ray connecting regions of opposite magnetic polarity, that are usually found with sunspots or regions of high magnetic flux at their footpoints. The loops are highly structured, have a wide variety of temperatures and spatial extent, and are filled with hot solar plasma. They exist throughout the solar disc, both in quiet Sun regions and in active regions (highly dynamic sources of explosive events). Some such loops are shown in the golden part of the Sun in figure 1.2, which represent the upper transition region and lower corona.

Other characteristics are small active regions associated with small bipo-

lar regions of the magnetic field, producing bright points observed X-ray, and are evenly distributed throughout the solar disk.

Flares are another corona phenomena, characterized by a sudden increase in radiative flux and release of matter, connected to magnetic field reconnection. These events last on average 15 minutes, where a rapid increase in density and temperature is observed. Flares lead to filament eruption and CMEs (coronal mass ejection), that supply the solar wind with high speed plasma and electromagnetic flux. If the bursts are sufficiently large and directed towards Earth, they cause geomagnetic storms and can be observed as auroras at the Earth's poles. CMEs can also be caused by prominences, which are often seen in loops of cold matter, with temperatures equivalent to those in the solar chromosphere, that are suspended above the corona.

When observing the corona one also sees large dark patches, known as coronal holes. These are regions of open magnetic flux tubes, that reach far into the corona and are usually associated with the fast solar wind. One such region can bee seen as the dark patch in the blue field in figure 1.2, which represents the hot corona.

Chapter 2

Studying the Sun

This chapter is dedicated to presenting the available means and methods for investigating the Sun. We begin with a review of the discovery of the electromagnetic spectrum and spectroscopy, followed by a description of basic spectral analysis, and review the physical processes behind the creation of emission and absorption lines. We continue with a discussion of the timescales in the solar atmosphere because they are important if we are to use spectroscopy for atmospheric diagnostics. Many assumptions of atmospheric conditions are made a priori to spectral analysis of the solar atmosphere, and in the last section of this chapter a review of the assumptions concerning transition region spectra are given.

2.1 Spectroscopy

Late in the 16th century sir Isaac Newton discovered the chromatic spectrum by passing a beam of sunlight through a glass prism, spreading white light into all the colors of the rainbow, and recollecting it to white light by the use of another prism. William Herschel extended the spectrum beyond the red end of the spectrum in 1800, to include what was later dubbed infrared

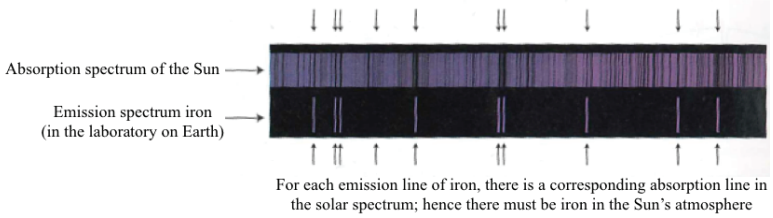

Figure 2.1: Example of spectral line identification.

radiation. In the following year Johann Wilhelm Ritter demonstrated the existence of ultraviolet radiation.

Solar spectroscopy was born when Wollaston, and later Fraunhofer, discovered the existence of dark lines in the solar spectrum. While Fraunhofer was only interested in these lines from an optical perspective, Robert Wilhelm and Gustav Kirchhoff established the empirical basis needed for the identification of the dark lines in the late 1850s by showing that bright emission lines in heated gases coincide with dark absorption lines seen when white light shines through the same cool gas. By careful comparison with emission lines seen in the laboratory for various gases Kirchhoff demonstrated the existence of a large number of chemical elements in the Sun, as can be seen in figure 2.1 showing an example of iron lines absorbed in the Sun and emitted in the laboratory.

A spectroscope is an instrument that observes in a restricted range in wavelength, and was first utilized by Norman Lockyer and Jules Janssen to study prominences in 1868. For the first time an instrument was available which made it possible to observe the Sun in broad daylight, but in spite of this technological advance most solar observations were carried out during total solar eclipses for a long time afterwards. In fact, one of the greatest discoveries in 19th century solar physics was made during a total eclipse by these scientists. They discovered an emission line in the yellow part of the spectrum, which did not correspond to any line of any known element, suggesting that the line belonged to an unknown element. This new element was named Helium (from the greek god Helios), and was subsequently isolated in the laboratory much later.

During a solar eclipse in 1864, a faint emission line in the green part of the spectrum was noticed, in the otherwise featureless corona spectrum. One of the discoverers suggested that "the green line" might come from a previously unknown element called "coronium". Little did they know that this discovery would lay the basis for the greatest enigmas in solar physics of all time, a mystery still unresolved.

Even though spectroscopy was a well established science, the process of line formation was not quantitatively understood until the rise of atomic physics and quantum mechanics in the 1920s, when Meghnad Saha developed a theory allowing the calculation of atomic ionization states in terms of thermodynamic variables such as temperature and pressure. This led to the conclusion that hydrogen, which had been spectroscopically identified by A. Ångstrøm in 1862, followed by helium were the dominant constituents in the solar atmosphere.

Evidence of the high coronal temperatures was first established by the spectroscopic work of atom physicists Walter Grotrian and Bengt Edlén in 1939, who identified"the green line" and other unidentified coronal emission lines to in fact be associated with high ionization stages of iron and nickel. Edlén further showed that 90% of the coronal lines could be attributed to

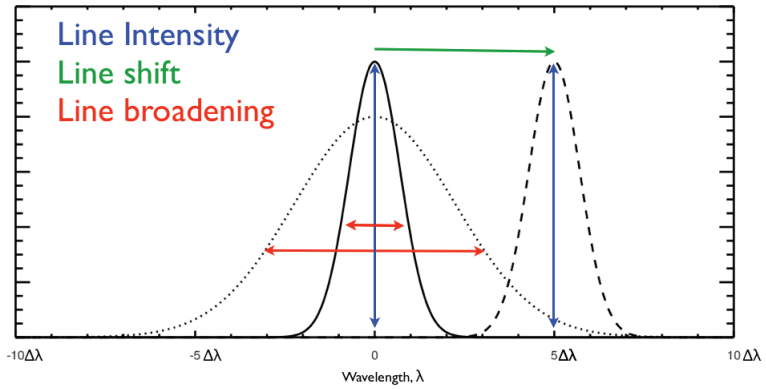

Figure 2.2: Spectral line representation, showing line intensity, line shift and line broadening.

Fe X, Fe XI, Fe XIII and Fe XIV. However, to ionize iron to such a high degree requires temperatures in the million kelvin range, thereby proving the high corona temperatures and laying the foundation for the coronal heating problem we still work on today.

2.2 Basic spectral line analysis

A spectral line can provide an incredible amount of information about the region of which it originated, where only the presence and intensity give us information of the temperature and composition. As can be seen in figure 2.2, a spectral line is not infinitely narrow, its width may vary and it can be Doppler shifted. These additional parameters provide information about the dynamics of and conditions in the emitting region, such as temperature, density, magnetic and/or electric fields, turbulence and rotation speed of the star we are observing. We will here give a short explanation of how the line is shifted and some different broadening mechanisms.

Doppler shift. A radiating particle moving with a velocity u along the line of sight produces a Doppler shift , $\frac{\Delta\nu}{\nu} = -\frac{\Delta\lambda}{\lambda} = \frac{u}{c}$, where the sign of the velocity is taken to be positive toward the observer, giving a blueshift for upward motion in the stellar atmosphere. The photon (with frequency ν' in its rest frame) is therefore detected as blueshifted to the frequency; $\nu = \nu'(1 + \frac{u}{c})$. The observed spectra is red/blue-shifted due to the orbital rotation of the Sun, but this is usually subtracted before initializing spectral line analyses.

Natural broadening (natural damping) is caused by the limited

n	name	profile	atom, ion	pertubers	conditions
2	linear Stark	Holtsmark	hydrogen, hydrogenic	ions	hot
2	linear Stark	Lorentz ?	hydrogen, hydrogenic	electrons	hot
3	resonance	Lorentz	hydrogen	hydrogen	solar
4	quadratic Stark	Lorentz	non – hydrogenic	electrons, ions	hot
6	van der Waals	Lorentz	non – hydrogenic	hydrogen	cool

Table 2.1: Collision broadening mechanisms, adaptation from Rutten (2003).

lifetimes of excited states and hence as a consequence of the Heisenberg uncertainty principle, defined by the spontaneous de-excitation rate, where the broadening is given by a Lorentz damping profile.

Thermal broadening is caused by the thermal motions in the plasma, where the distribution of velocities in the line of sight are given by the component form of the Maxwell distribution. The line of sight velocity is then $u_{th} = \frac{\nu-\nu_0}{\nu}c$, with variance $u_o = \sqrt{2k_BT/m}$ and Doppler width $\Delta\nu_{th} = \frac{\nu_0}{c}\sqrt{2k_BT/m}$.

Collisional/pressure broadening is the general term for all broadening mechanisms caused due to collisions with and/or perturbations by other particles, which is caused due to the neighboring particles and their charge effecting the emitting/absorbing ion through Coulomb interactions. The atomic level energy of interest is disturbed as a function of the separation, R, between the pertuber and the emitting/absorbing ion. This relationship can be approximated to a power law given by $\Delta\nu \propto 1/R^n$. The power index n defines the name and type of the interaction, which are all listed in table 2.2.

Turbulent broadening is caused by other motions besides the microscopic thermal motions and the macroscopic rotation of the Sun, such as waves and turbulent motions. These are included by introducing two fudge parameters, called micro and macro turbulence. Micro turbulence is ξ, when redefining the Doppler width $\Delta\nu_D = \frac{\nu_0}{c}\sqrt{\frac{2k_BT}{m} + \xi^2}$ and macro turbulence is ξ_{macro}, found by convolving the commuted emergent intensity profile with a gaussian velocity distribution; $(I_c - I_\lambda)/I_c = ((I_c - I_\lambda)/I_c)_{comp} * \frac{1}{\xi_{macro}\sqrt{\pi}} e^{-\xi^2/\xi^2_{macro}}$. Even though the name implies random motions, they are used as ad-hoc fitting parameters that serve to correct any deficiencies in the radiation treatment, including collisional broadening, dynamical effects, inhomogenities and other complicated contributions to the spectral line formation and broadening such as hyperfine splitting, isotope splitting, and Zemann splitting.

In spectroscopic investigations of the transition region the line broadening is divided in two parts, where one part is the thermal broadening and all other broadening mechanisms are collected in the general term non–thermal

broadening defined as the micro turbulence broadening here. Any model (usually 1D atmospheres) deficiencies, and resulting synthetic spectra are therefore also included in this term.

2.3 Processes of emission line formation

There are many processes that lead to the formation of emission and absorption lines, and depending on the atmospheric conditions the radiative field itself can play a significant role. Ionization and recombination processes will change the degree of ionization of ions, producing or absorbing photons and leading to new spectroscopic fingerprints. Additionally, there are scattering processes that change the paths of both photons and electrons, contributing to the continuum emission we observe. A schematic overview of some of these processes is presented in figure 2.3.

The atomic transitions leading to emission and absorption lines lines have transition rate probabilities that depend on the quantum mechanical properties of the electron configurations in the different ions. Transition rate probabilities are additionally dependent on local quantities of the emitting region such as temperature, pressure, electron density, and electric and magnetic fields. The calculation of transition rate probabilities therefore become extremely difficult, but atomic physicists have developed simplified methods for these calculations valid under different atmospheric conditions, given a set of assumptions. We will go into more detail regarding our objective and hence the appropriate assumptions and simplifications in section 5.3, where the necessary transition rate probabilities will be discussed.

2.4 Timescales

To be able to use spectroscopy for diagnostic purposes of the solar atmosphere some knowledge about the ionization state of the emitting ion is required. It the equilibration timescales are sufficiently short compared to the dynamical timescales of the region of emission ionization equilibrium can be assumed. The ionization and excitation relaxation timescales are dictated by the slowest process in the emission line formation, which is usually collisional ionization. Following Rutten (2003), the collisional ionization rate can be expressed as

$$C \approx 2.7 \left(\frac{E_0}{kT}\right)^{-2} T^{-3/2} e^{E_0/kT} N_e \ \ \mathrm{s}^{-1}, \tag{2.1}$$

where E_0 is the collisional ionization energy, N_e the electron density, T the temperature and k the Boltzmann constant.

Using the typical ionization energy for transition region ions, $\approx$ 50 eV, and the Fal C model atmosphere (Fontenla et al., 1993) electron density

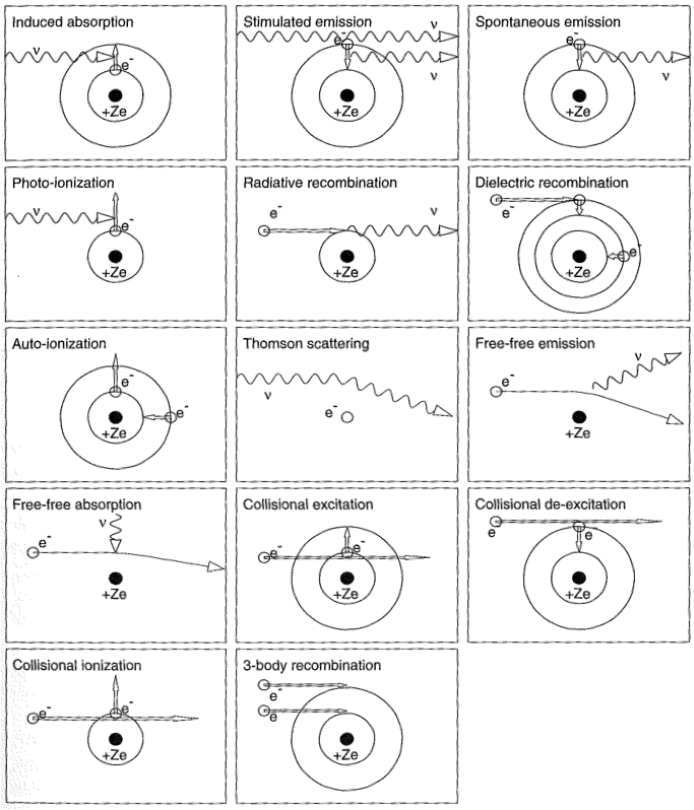

Figure 2.3: Schematic overview of different photon/electron/ion interactions responsible in emission and absorption line formation. A description of the processed can be found in appendix A. Credits: Aschwanden (2004)

6.665 10^9cm^{-3} at 10^5K , gives a typical equilibration time;

$$\tau_i = \frac{1}{C} \approx 20 \text{ s.} \tag{2.2}$$

An estimate of the dynamical timescale can be calculated using the sound speed ($c_s = \sqrt{kT/m_H}$) and a typical length scale of the transition region, say L =200km, resulting in

$$\tau_d = \frac{L}{c_s} \approx 7 \text{ s.} \tag{2.3}$$

The equilibration timescales are clearly longer than the dynamical timescales. However, the ionization timescales are strongly dependent on the temperature, and reduce to ∼1 s when increasing the temperature by a factor of 2, compared to the dynamical timescales reducing to ∼ 5 s. This means that the emitting ions are only in equilibrium with the local quantities if the ionization and recombination times are smaller than the dynamical timescales. Otherwise, the temperature and density information the observer receives through the spectral line intensity is not the same as the temperature and density at the region of emission. Spectroscopic investigations can therefore not be trusted if the ionization and recombination timescales of the emitting ion of interest are longer than the dynamical timescales of the region of emission.

2.5 Assumptions

The solar spectrum includes lines of many different atoms and ions, carrying information about their emitting (or absorbing) regions. A classical overview of the formation heights of many spectral lines is presented in figure 2.4. We are interested in the spectral lines of the heavier ions, formed in high temperature regions, that carry information about the transition region and corona, as demonstrated by blue rings in figure 2.4. Traditionally, a set of approximations are used when modeling theses lines.

The optically thin approximation: The plasma along the line of sight to where a line forms has low enough density that the emitted photons travel unimpeded through space. This allows for scattering and absorption processes to be ignored when analyzing the spectra. The assumption is valid when the optical depth, τ_ν, of the spectral line under scrutiny is smaller than 1:

$$\tau_\nu = \int_0^z \alpha_\nu dz \leqslant 1 \,, \tag{2.4}$$

where α_ν is the monochromatic line extinction coefficient.

The other important assumption is that of statistical equilibrium (SE). This means that all transitions that populate and depopulate an energy

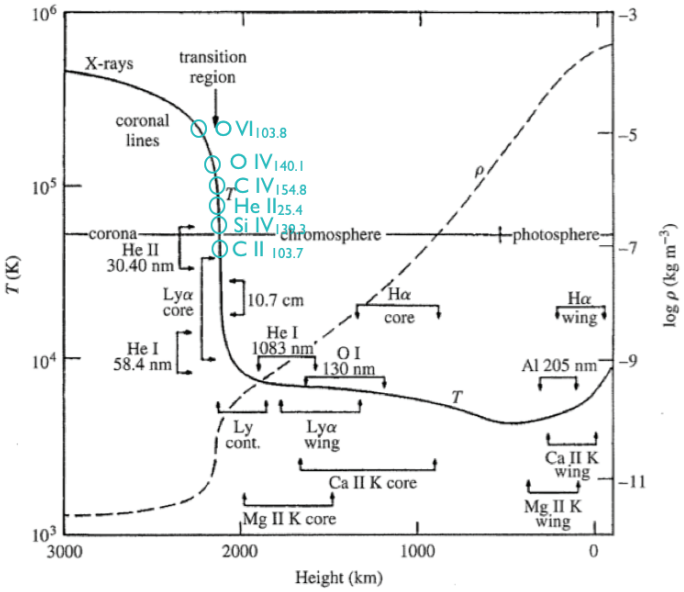

Figure 2.4: Logarithmic plot of the temperature structure and mass density structure of the solar atmosphere, with the source of some spectral lines included. Adapted from Carroll and Ostlie (2006), and modified to include transition region lines.

and/or ionization level are instantaneous equilibrated with the local environment. Together with the optically thin approximation, where the transitions are only functions of the local temperature and mass density of the plasma, this leads to:

$$\begin{aligned} \frac{\partial n_i}{\partial t} + \nabla \cdot (n_i \mathbf{u}) &= \sum_{j \neq i}^{N_l} n_j P_{ji} - n_i \sum_{j \neq i}^{N_l} P_{ij} \\ &\Downarrow \\ \sum_{j \neq i}^{N_l} n_j P_{ji} &- n_i \sum_{j \neq i}^{N_l} P_{ij} = 0 \,, \end{aligned}$$

where n_i is the population density of ion level i, N_l is the total number of levels in the model atom, P_{ij} represents the transition rate coefficient between level i and j, and $\mathbf{u}$ the macroscopic velocity. The time dependence and advection of the ion populations can be ignored by assuming statistical equilibrium. One therefore assumes that the ionization and recombination timescales are smaller then the dynamical timescales so the ions have time to equilibrate themselves with the local environment.

By considering the low densities and weak radiation field of the transition region and corona a third assumption can be made, namely the corona approximation, which states that the typical timescales of collisional processes are shorter than for the ionization and recombination processes. It follows that the collisional excitation determines the population of excited states. Spontaneous radiative de-excitation processes overwhelm the stimulated emission and collisional de-excitation processes, resulting in a balance between the collisional excitations and the spontaneous radiative de-excitation;

$$n_u A_{ul} = n_l n_e C_{lu}(T) \,, \tag{2.5}$$

where A_{ul} is the Einstein decay probability coefficient, $C_{lu}(T)$ the collisional excitation rate at temperature T, n_e the electron density, n_l and n_u are the population numbers of the lower and upper level of the transition, respectively. These factors determine the intensity through,

$$I_\nu = \frac{h\nu}{4\pi} \int_0^z n_u A_{ul} \mathrm{d}z \,, \tag{2.6}$$

where z is the line of sight and ν is the frequency of the spectral line. With a bit of rearranging the emission line intensity can be written as

$$I_\nu = A b_x \int_0^z n_e n_H G(T, \nu, n_e) \mathrm{d}z \,, \tag{2.7}$$

where $G(T, \nu, n_e)$ is the contribution function, which is strongly dependent on the electron temperature an weakly dependent on the electron density.

Additional isothermal assumptions (Raymond and Doyle, 1981) makes it possible to determine both temperature and electron density from a set of any two observed spectral lines.

However, the method breaks down when strong temperature gradients are present in the line of sight and equation 2.7 is redefined as

$$I_\nu = Ab_x \int_0^T G(T, \nu, n_e) DEM \mathrm{d}T \,, \tag{2.8}$$

where the differential emission measure ($DEM = n_e n_H \frac{dz}{dT}$) is a measure of the amount of plasma along the line of sight that contributes to the emitted radiation in the temperature interval between T and $T + \Delta T$ (Pottasch, 1964).

There are additional methods that take advantage of the scenario when the corona approximation breaks down. These methods consider spectral line ratios to introduce an electron density dependency or a temperature dependency, depending on the lines. For example, using two spectral lines of the same isoelectronic sequence, where only one of the lines follows the corona equilibrium, the resulting emissivity ratio becomes

$$\frac{\epsilon_{\nu i}}{\epsilon_{\nu k}} = \frac{\nu_{gi}}{\nu_{gk}} \frac{C_{gi}(T)}{C_{gk}(T)} \left(1 + n_e \frac{C_{km}(T)}{A_{kg}}\right) \,, \tag{2.9}$$

where ν_{gi} and ν_{gk} are the frequencies of the respective spectral lines, formed from the transition from level i to g and from level k to g, respectively. By assuming statistical equilibrium ionization and an identity between the emissivity and the intensity one can directly measure the electron density of the region of emission in the atmosphere. Similar derivations can isolate a temperature dependence in an emissivity ratio, and hence be used in temperature diagnostics.

These assumptions and approximations have been successfully implemented for more or less all spectroscopic analysis of the solar transition region and corona. However, a large number of open questions remain.

Chapter 3

Observations of the transition region

The solar transition region emits in the ultraviolet part of the electromagnetic spectrum, which cannot be observed by ground based telescopes because Earth's atmosphere absorbs or reflects a great part of the solar UV emission. This means that space based observatories are required for the task. Examples of space borne instruments that have observed or are still observing the transition region are the UVSP on SMM (Woodgate et al., 1980), the rocket borne HRTS instrument (Brueckner et al., 1986; Bartoe et al., 1986), SUMER (Wilhelm et al., 1995) and CDS (Harrison et al., 1995) on the SOHO satellite, TRACE (Handy et al., 1999), and EIS (Culhane et al., 2007) onboard the Hinode satellite.

The observational facts and modeling efforts of the pre-SOHO era were well summarized by Mariska (1992), while Wilhelm et al. (2007, 2004) have done a tremendous amount of work in collecting and summarizing the findings for the remaining two decades of data and research on the subject. The general understanding so far is that transition region emission mainly comes from structures connected via the magnetic field to the hot corona above, and where the temperature profile is determined from the properties of thermal conduction along the magnetic field. But despite the tremendous amount of data available, most models are not able to reproduce even the average lower moments of the observations, *i.e.* the intensity, doppler shift, and linewidth of the region. This is a strong indication that the general understanding of the transition region is incorrect or must be modified in some way.

The observed solar DEM displayed by the solid line in figure figure 3.1, is a compilation of many emission lines, and represents the amount of emitting material along the line of sight as function of the temperature. Several studies using spectral synthesis from one-dimensional models have been performed (Klimchuk et al., 2012; Chitta et al., 2013; Warren, 2006) by com-

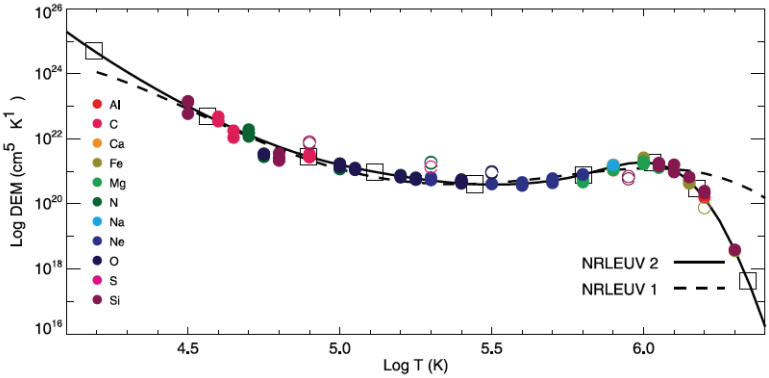

Figure 3.1: Quiet Sun DEM, derived from Harvard Skylab (dotted line) and SOHO (solid line) observations. Adapted from Warren (2006).

paring the models with the observed DEM. However, as of yet no one has managed to recreate a synthetic DEM that entirely matches the observed DEM, where the models usually fail at the low and high temperature ends. The negative slope at low transition region temperatures implies that there is much more material emitting at these temperatures than 1D models readily can reproduce, *i.e.* the models predict smaller than observed line intensities for lines formed below 2×10^5K. Partly successful attempts have been made with multi threaded models, where each thread represents a 1D loop model of varying loop parameters. The method is based on the assumption that a given observation comprises of very many threads at different phases of the heating and cooling cycle. The basic idea being that each thread is heated impulsively by a 'nanoflare' like event and subsequently cooled. There is presently a vigorous debate in the solar physics community on whether the reoccurrence of heating events is faster or slower than the characteristic cooling time of the loops under consideration (Bradshaw and Klimchuk, 2011). However, Judge et al. (1995) found large systematic discrepancies in the emission measure analysis of transition region lines, which can only be accounted for by a breakdown of one or more standard assumptions.

Observed Doppler shifts, presented in the right-hand panel of figure 3.2, show a persistent redshift for lines formed at transition region temperatures (Doschek et al., 1976), with a maximum average redshift of approximately 10 km/s found for lines formed at some 10^5 K. At greater temperatures the redshifts decrease, with indications of average blueshifts for coronal lines (Peter, 1999). Explanations for this finding, based on the idea of cooling, returning, spicular material, have abounded (Athay, 1984; Doyle et al., 2002a; Hansteen and Wikstøl, 1994; Mariska et al., 1978; Bradshaw and Cargill,

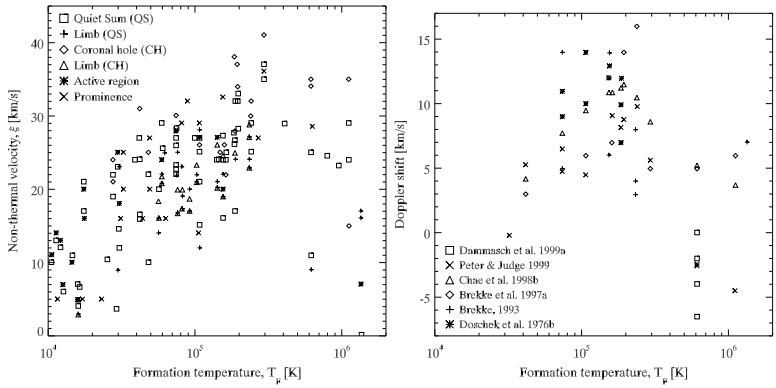

Figure 3.2: The non–thermal velocity (left) and the Doppler velocity(right) collected by Wilhelm et al. (2007) from various referenced representing data from various solar conditions.

2010) but it has proven very difficult to reproduce the observational values with 1D hydrodynamic models.

The spectral lines formed in the middle transition region show large unresolved velocities resulting in large linewidths. The non–thermal velocities vary from 10 km s^{-1} in the cooler transition region ($\sim 10^4$K) to 30 km s^{-1} in the mid-transition region (2×10^5K) and decrease for higher temperatures (Chae et al., 1998, and references therein). A collection of the reported non–thermal linewidths is presented in the left panel of figure 3.2. Linewidths also seem to depend on region in the solar atmosphere, with high values found at loop footpoints in disk center observations (where the loop footpoints presumably are oriented along the line of sight) (Hara et al., 2008). However, collecting the data of several studies (Wilhelm et al. (2007), figure 3.2) demonstrates no systematic difference in the non–thermal line broadening for the various solar conditions. In general, models give much smaller linewidths than those observed, leading to the conclusion that the Sun is dynamic on much smaller scales than both what is currently observable and for that matter resolvable by numerical models.

Finally we note that the atmospheric conditions change on timescales of only a few minutes (Brekke, 1999; Berger et al., 1999) and that line intensities and profiles show strong time variabilities, with short timescales especially prevalent in the middle transition region (Hansteen et al., 2000; Brković et al., 2003). The solar atmosphere has proven to be much more complicated than initially assumed.

The facts discussed above, discovered after the development of the diagnostics methods, make the initial assumptions in spectral analysis question-

able. With so many unresolved issues related with the observations there is clear evidence that better models are required.

Chapter 4

Modeling the solar atmosphere

In order to understand the physical driving mechanisms of the solar emission many different models have been put forth.

Empirical models transform spectroscopic data from a range of instruments with different spatial, spectral and temporal resolutions, to a model of the solar atmosphere. Using different inversion techniques including many assumptions, they attempt to deduce the temperature and density as function of the height. These models usually assume that the atmosphere is static, thereby applying simple geometry to structures we know are highly complex. While they manage to reproduce the observed DEM, they fail to explain the separate structures we observe, and there are clear discrepancies between the empirical models and the observed emission (Mariska, 1992). This is why a great amount of time have been invested in developing theoretical models that can describe the structure of the solar atmosphere, and the solar transition region.

4.1 1D models

Because of the high temperatures and the large degree of ionized elements, the solar atmosphere can be described as a plasma, where observations clearly show that the magnetic field plays an important role. The goal is therefore to model the thermodynamical as well as the magnetic properties of the solar atmosphere and to reproduce the observed emission.

Due to computational limitations, the solar atmospheric modeling has for the most part been done assuming 1D geometry. In such models the atmospheric plasma is confined within loops, where the magnetic field only contributes by confining the loop. The models are usually assumed to be static, with constant loop cross-sections, and by neglecting gradients across the field. Further, they are assumed to inherit a large degree of free parame-

ters, where the most important is a predefined heating mechanism. Studies of 1D solar models of varying degree of complexity are plentyful, for example studies by Klimchuk et al. (1997), Walsh and Galsgaard (2000), Spadaro et al. (2003), Warren (2006), Reale (2010) and Winebarger et al. (2011) to name but a few.

The environment in the outer solar atmosphere is highly dynamic, where atmospheric conditions change significantly on timescales of only a few minutes (Brekke, 1999; Berger et al., 1999). It consists of inhomogeneous, highly dynamic plasma with strong vertical stratification, and is characterized by rapid changes on many size scales. The short dynamical timescales present puts the assumption of ionization equilibrium in question. This is because the UV radiation from the transition region predominately originates from highly ionized heavy elements, which have ionization and recombination timescales that might be much longer than the typical dynamical timescales. Griem (1964) stated specifically the case of flows through temperature gradients, such as the solar transition region, where ionization equilibrium easily can get disrupted.

Several studies have considered non–equilibrium ionization under steady state conditions, in which case advection through a temperature gradient leads to the disruption of ionization equilibrium. Raymond and Dupree (1978) and Dupree et al. (1979) showed that electron density diagnostics are underestimated in the presence of strong down flow velocities when non–equilibrium ionization is ignored. Joselyn et al. (1979b,a) investigated the consequences of a steady flow through a range of temperature gradients on the ionization equilibrium, and concluded that the assumption breaks down for flow speeds above 20 km s^{-1} for iron and above 1 km s^{-1} for carbon and oxygen. Borrini and Noci (1982) found deviations from ionization equilibrium, with a pronounced effect for the cooler loops due to having steeper temperature and density gradients in their loop model. Noci et al. (1989a,b) calculated the number densities of carbon ions in 1D coronal loop models in the case of siphon flow, showing evidence of non–equilibrium ionization, for velocities of only a few km s^{-1} at the loop top and for 10 times slower flows at the base. Spadaro et al. (1994) found reduced intensities for lines emitting from the C IV and O IV-O VI ions for both up and down flows, which results in an overestimation of the plasma temperature by as much as an order of magnitude when ignoring non–equilibrium ionization. Edgar and Esser (2000) studied the first ionization potential (FIP) effect, and found that including non–equilibrium ionization enhances the population of ions of low FIP relative to those of high FIP.

A sudden temperature increase can also be caused by other phenomenon, such as nanoflares (i.e. magnetic reconnection) or shocks, where changes in the local properties (such as temperature, density, pressure) occur on much shorter timescales than the equilibration times of the emitting ions. It is therefore important to consider the plasma as a whole by taking into account

the plasma velocities, as well as the local variables and their time evolution. Several analyses have been performed in order to study the effect of a sudden energy release in the atmosphere on the ionization balance: Hansteen (1993) developed a 1D numerical loop model that solves the hydrodynamic equations, including the rate equations (equation 2.5), computing the non–equilibrium ionization effects on the radiative losses and on the evolution of the plasma's internal energy. By studying the dynamic response of a coronal loop to energy released as heat near the loop apex, it was found that the radiative loss may change by a factor of 2 during the loop evolution, as a result of flows and waves, confirming the importance of non–equilibrium ionization in the line forming process. The model was the first to numerically reproduce the persistent redshifts in transition region lines first reported by Doschek et al. (1976), where the amplitude of the predicted line shift was shown to depend on the ionization timescale of the emitting ion.

Similar one-dimension loop models using the radiative losses due to EUV line emission based on time–dependent ionization and the response of impulsive heating events, are plentiful. For instance, Doyle et al. (2002b) found that the delay in the response of the Doppler shifts of mid transition region lines depends on the temperature where the energy release occurs. Bradshaw and Mason (2003a,b) found that the intensities of transition region and corona line remain steady in spite of a great temperature increase, and concluded that broad/narrow-band imaging instruments can miss small-scale heating events entirely, due to the weak temperature sensitivity of the non–equilibrium emissivity. By studying flare evolution, Bradshaw et al. (2004) showed that the longevity of observed loops in the TRACE 171 Å and 195 Å filters can potentially be reconciled with non–equilibrium populations of the emitting ions. In the same model, Bradshaw and Cargill (2006) found that even though the plasma temperature reaches > 10 MK, the emission would never show this, due to the delayed response of the emitting ions, and the onset of fast cooling by thermal conduction. In contrast to what is predicted by models assuming ionization equilibrium, their synthesized emission in the wavelength range of Hinode-EIS shows no hot (>10 MK) component of the plasma, in agreement with observations. Using a multi–thread loop model, Bradshaw and Klimchuk (2011) concluded that small-scale impulsive heating inducing non–equilibrium ionization leads to predictions for observable quantities that are entirely consistent with what is actually observed. With increased knowledge, it has become obvious that the assumption of statistical equilibrium ionization does not hold for the dynamic transition region and explosive corona. 1D models can primarily be used to investigate the possible relevance of a physical effect, however they cannot verify or disprove the importance of that effect in the fully 3D solar atmosphere. Even though 1D models have given us an undeniable insight in understanding the hot solar atmosphere, they have their obvious limitations. Generally, 1D loop models include gravitational stratification and hydrostatic equilibrium, how-

ever, EUV loop observations reveal density deviations of up to two orders of magnitude along the loop, super-hydrostatic density scale heights, near-isothermality along loops, and dynamical loop behavior. In spite of having included complex physics, one of the biggest problems with the models is inconsistency with the temperature evolution, where observations show significantly longer cooling times compared to the model predictions. In other words, it seems that studying separated individual loops, and thus ignoring the complex three dimensional (3D) background that contains myriads of competing other loop structures and magnetohydrodynamic plasma will only get us so far. In order to achieve a more complete description of the solar atmosphere, we have to delve into more complex 3D reality of the solar atmosphere.

4.2 3D models

In the last decade or so high performance 3D numerical models of the solar atmosphere have become available, spanning the entire solar atmosphere from the upper convection zone to the corona. The codes solve the time–dependent magnetohydrodynamic (MHD) equations, including complex physics such as non–gray, non–LTE radiative transport in the photosphere as well as magnetic field aligned heat conduction in the corona. Some codes, like CO^{5}BOLD (Freytag et al., 2010), Stagger (Nordlund and Galsgaard, 1995), and MURaM (Vögler et al., 2005), handles the deeper layers of the solar atmosphere while others focus on the outer visible part we are able to observe (Brandenburg and Dobler, 2002; Robinson et al., 2003; Heinemann et al., 2006; Abbett, 2007; Muthsam et al., 2010; Stein and Nordlund, 1998; Gudiksen et al., 2011). The numerical and physical obstacles are dealt with in a variety of manners which are all to complex to delve into here. CO^{5}BOLD, Stagger, and MURaM have been compared by Beeck et al. (2012), concluding that they are highly reliable in computing comprehensive simulations which can be used as a tools for studying stellar atmospheres and surface convection. Because 3D solar atmosphere models are constructed from first principles, they have enabled astronomers to predict various observables such as solar granulation properties and spectral line profiles (Carlsson et al., 2004; Asplund et al., 2000), and reproducing the observed center-to-limb variations to astonishing precision (Pereira et al., 2013; Asplund et al., 2009). See Magic et al. (2013) for a thorough discussion about the advancements in 3D numerical simulations of the solar atmosphere.

Now, taking a step back to the observational riddles presented in chapter 3, 3D numerical simulations of the solar atmosphere seem to do a good job toward an answer to these puzzles.

The overall shape of the DEM was first produced by Peter et al. (2006)

from their 3D MHD model, but they failed to reproduce the high- and low- temperature ends of the curve. In the same paper they report on average redshifts of their synthetic transition region lines, with significant time variations in the Doppler shifts of the synthesized spectra, while the DEM only slowly varies in time. Only Peter et al. (2006) have performed analysis of the non–thermal linewidths derived from synthesized spectra, but they generally obtain much smaller linewidths than what are observed and are unable to reproduce the reported peak at 2×10^5K. In the same paper they explicitly discuss ionization balance when synthesizing the spectra from their models, and refer to "post-MHD" models which should include non–equilibrium ionization.

In recent years the computational power to solve the full 3D radiative MHD model of the solar atmosphere, including the rate equations, has become available. Not long ago, Hansteen et al. (2010) found that 3D simulations, using the Bifrost code, reproduces the average redshifts at lower transition region temperatures, in addition to also finding blueshifts in hotter coronal emission, as reported from observations (Peter, 1999). In a follow-up paper, Guerreiro et al. (2013) explained this as a result of the preponderance of low lying cool loops, which is a dynamic version of Antiochos (1982) idea of low lying loops dominating lower transition region emission.

The Ph.D candidate has constructed a Bifrost module that can be used to compute the ionization state of the most important radiating ions in the transition region, which is the topic of this thesis. The method for solving the ionization rate equations and the computational implementation will be presented in the next chapter, together with a presentation of the results.

Chapter 5

Non–equilibrium ionization in 3D numerical models

The previous chapters have given an introduction to the Sun and provided the motivation for the candidates contribution to three-dimensional non–equilibrium ionization models. This chapter will focus on the candidate's scientific contribution, starting with a short summary of the stellar numerical code Bifrost. This will be followed by a discussion of the method of solving the rate equations, together with the numerical implementation into the Bifrost structure. This thesis consists of three papers, and a short summary of each will be given.

5.1 The numerical framework: Bifrost

The Bifrost code (Gudiksen et al., 2011) is a high performance multiprocessor solver for three-dimensional stellar atmospheres, written to span the entire solar atmosphere from the upper convection zone to the lower corona.

The basic idea is to solve the MHD equations:

$$\frac{\partial \rho}{\partial t} = -\nabla \cdot (\rho \mathbf{u}) \tag{5.1}$$

$$\frac{\partial \epsilon}{\partial t} = -\nabla \cdot (\epsilon \mathbf{u}) - P \nabla \cdot \mathbf{u} + Q \tag{5.2}$$

$$\frac{\partial \rho \mathbf{u}}{\partial t} = -\nabla \cdot (\rho \mathbf{u}\mathbf{u} - \tau) - \nabla P + \mathbf{J} \times \mathbf{B} + \rho \mathbf{g} \tag{5.3}$$

$$\mu \mathbf{J} = \nabla \times \mathbf{B} \tag{5.4}$$

$$\mathbf{E} = \eta \mathbf{J} - \mathbf{u} \times \mathbf{B} \tag{5.5}$$

$$\frac{\partial \mathbf{B}}{\partial t} = -\nabla \times \mathbf{E} \tag{5.6}$$

where the density, the velocity vector, the internal energy per unit volume

and the magnetic flux density vector are represented by ρ, $\mathbf{u}$, ϵ, $\mathbf{B}$, respectively. τ, P, $\mathbf{J}$, $\mathbf{g}$, μ, $\mathbf{E}$ and η are the stress tensor, the gas pressure, the electric current density vector, the gravitational acceleration, the vacuum permeability, the electric field vector and the magnetic diffusivity, respectively. The Q quantity can contain a number of terms, depending on the individual experiment. For example, it may encompass the energy contributions from the thermal conduction, radiative transfer and equation of state (EOS).

Bifrost resembles a skeleton in many ways, with a high degree of modularity. The different procedures or methods are contained in a number of modules, and each module may contain a variety of algorithms to be used for solving the same physical problem for example like the time stepping and the complexity of the physics required for the experiment of choice. The code is described in detail in Gudiksen et al. (2011), and therefore only a short summary will be presented here. The solution of the rate equations is included as a separate module added to the Bifrost skeleton.

Bifrost solves the full radiative MHD equations on a staggered grid. The radiative flux divergence in the photosphere and chromosphere, which is included in Q, is obtained using the method of opacity binning, developed by Nordlund (1982), and 3D scattering is solved by methods developed by Skartlien (2000). Non–LTE radiative losses in the upper chromosphere and lower TR are modeled using the recipes derived by Carlsson and Leenaarts (2012) and contribute as sink sources in Q, while optically thin radiative cooling is assumed in the TR and corona. As the plasma temperature rises, thermal conduction becomes an important contributor in the energy equation, and is included following the method introduced by Spitzer (1956).

The experiment setup selected when developing and running with the non–equilibrium solver to be presented in section 5.4 includes the module for the EOS which assumes local thermodynamic equilibrium (LTE) for atomic level populations and instantaneous molecular dissociation equilibria, based on tables generated with the Uppsala Opacity Package (Gustafsson et al., 1975). The pressure and the temperature are retrieved from tabulated values given the particular ϵ and ρ.

The time stepping module chosen for this experiment was a third-order predictor-corrector Hyman time stepping scheme (Hyman, 1979), also described in Gudiksen et al. (2011). This leap-frog scheme is applied in order to obtain a 3rd order accuracy in time when solving the MHD equations.

The boundaries are periodic in the horizontal dimensions. Characteristic boundary conditions are applied at the top vertical boundary, representing the corona boundary. Outflowing materials are allowed to leave the bottom vertical boundary of the box, while the entropy of the inflowing material is fixed.

5.2 Atomic models

Before presenting the numerical scheme it is important to discuss the atoms, ions, energy levels and transition rate probabilities necessary for solving the rate equations;

$$\frac{\partial n_i}{\partial t} + \nabla \cdot (n_i \mathbf{u}) = \sum_{j \neq i}^{N_l} n_j P_{ji} - n_i \sum_{j \neq i}^{N_l} P_{ij} \tag{5.7}$$

where n_i is the population density of ion level i, N_l, is the total number of levels in the model atom, P_{ij} is the transition rate coefficient between level i and level j, and $\mathbf{u}$ the macroscopic velocity. The number of levels N_l is the first obstacle that must be overcome, because the rate equations are a coupled set of N_l equations. If all the energy levels of every ion of an atom were to be included alone, even if the transition rate probabilities where fixed, the solution vector would still include $N_l \times N_l$ numbers of unknowns at every grid point in the computational domain, and the problem would quickly become unfeasible. This is solved by using the atomic diagnostic package DIPER (HAO Spectral Diagnostic Package For Emitted Radiation, Judge and Meisner (1994)). This database consists of a set of atomic data collected from various sources (Arnaud and Rothenflug, 1985; Shull and van Steenberg, 1982, along with many others listed in the DIPER reference guide), providing a collection of data for the atom of interest. The database supplies the energy levels of every ion of the specified atom, together with transition probability data and other level information for these levels. The unique aspect of DIPER is that it gives the user the ability to manipulate the datasets, and makes it possible to construct specified atomic data files.

The purpose is to construct an atomic model which includes all the necessary ionization stages and energy levels required to maintain the ionization equilibrium fractions, but which consist of only a few of the energy levels of the native data in the database. The most important level is the ground state of the ion, because all excited electrons will eventually fall down to this state, but there are levels that have such a short lifetime, that the de-excitation to the ground state is very rapid, and hence do not affect the the ionization fraction of the mother ion. However, forbidden (or meta stable) levels of ions can play an important role in the population density of an ion, because transitions from metastable excited levels typically corresponds to those forbidden by electric dipole selection rules, and are hence relatively unlikely to occur. An electron that happens to find itself in a metastable configuration is essentially trapped there. Of course, since transitions away from a metastable state are not impossible, the electron will eventually be able to decay to a less energetic state by spontaneous emission. This is the reason why these levels have a long lifetime and can therefore be major contributors to the total population density of the ion. It is therefore impor-

tant to keep these levels when constructing the atomic model. By utilizing DIPER, the levels to be included in the new atomic model can be specified. Other possible methods of reducing the number of levels are to merge levels of doublet or triplet states by creating one single 'new' synthetic state. This is done by constructing a weighted mean spontaneous decay rate and level energy, based on the statistical weights of the original levels. Since the lower levels of these transitions are the same, the upward collisional transition rate for the newly created upper level is computed by summing the native collisional transition rates.

By solving the statistical equilibrium equations and keeping track of the level reduction to ensure that statistical equilibrium is maintained, the amount of levels can be reduced by approximately an order of magnitude.

5.3 Transition rate probabilities

The transition rate probabilities P_{ij} entering the rate equations (5.7) are composed of two parts, namely the collisional rates and the radiative rates. The collisional rates are only dependent on the temperature and electron density, whereas the radiative rates depend on the radiation field, which thereby introduces global coupling, meaning that a radiative transfer equation at every frequency has to be solved for each rate equation. This has to be done simultaneously for all grid points, because of the global coupling. The problem very quickly becomes unfeasible to solve, even on the largest supercomputers, since the solution vector at every time step would have $N_\nu \times N_l \times N_d$ number of unknowns, where N_ν , N_l and N_d are the number of frequencies, rate equations and grid points, respectively.

The main reason it is possible to continue with these calculations is due to the fact that the transition region and corona are more or less optically thin, where radiation and matter largely decouple. The problem can therefore be simplified according to the optically thin approximation, which reduce the number of unknowns to N_l by neglecting scattering and absorption processes when calculating transition rate probabilities.

The processes included in the transition rate probabilities are spontaneous emission, direct ionization and recombination, collisional ionization, auto–ionization, radiative recombination, and three–body recombination as well as bound-bound transitions such as collisional excitation/de–excitation. The method of calculating the transition rate probabilities using the atomic files created with DIPER is described in Paper I (Olluri et al., 2013b).

5.4 The non–equilibrium ionization solver

The non–equilibrium ionization solver is included in Bifrost as a separate module, solving the rate equations at every time step of a simulation. The

module can be attached to the Bifrost skeleton, and hence included in any numerical experiment. In this section the basic algorithm is described, and some of the objectives for the implementation and the numerical scheme are presented.

5.4.1 Initial conditions

When an experiment including the non–equilibrium ionization solver is initiated, the atomic data file is read and sorted into arrays containing the different type of transition rate parameters and level information. These array are later used when calculating the transition rate probabilities.

The calculations of the transition rate probabilities are well summarized in Paper I (Olluri et al., 2013b), with exception of the direct ionization from equation 9 in the paper, where the calculations are done in advance and stored in a large table as function of logarithmic temperature values during the initiation of the simulation, following linear interpolations in the table for every level at every time step later. This modification was necessary because of the very computationally expensive recipe for calculating the direct ionization rate, which among other involve multiple evaluations of the exponential integral. With this workaround the computational time was reduced to somewhere between 10% and 20%.

The initial population densities are set by solving the statistical equilibrium equations:

$$\sum_{j\neq i}^{N_l} n_j P_{ji} - n_i \sum_{j\neq i}^{N_l} P_{ij} = 0 \tag{5.8}$$

which represent a set linear equations $\mathbf{An} = \mathbf{0}$, where $\mathbf{A}$ is the rate matrix with elements $A_{ii} = \sum_{j\neq i} P_{ij}$ and $A_{ij} = -P_{ji}$,

The equation of particle conservation is utilized to close the system and to achieve a unique solution;

$$n_X = \sum_i n_i \quad \text{and} \quad n_X = \frac{\rho}{m_{av}} \frac{10^{A_X - 12}}{\sum_Y (10^{A_Y - 12})} \tag{5.9}$$

where the element population density, n_X, is dictated by Asplund et al. (2009) solar abundance values, ρ is the mass density from the simulation, m_{av} is the average mass per particle and A_X is the corresponding abundance of element X, and the sum over Y, sums over all the abundances in the Asplund et al. (2009) table.

5.4.2 The algorithm

The left hand side of the rate equations (equation 5.7) represent a continuity equation for each ion population density, while the right hand side represent

sink and source terms due to transitions between the different levels included in the atom model.

It is possible to use explicit finite difference schemes to solve the rate equations since such schemes are relatively fast and simple, but the solutions quickly become unstable and begins to oscillate due to the courant condition. Considering that the transition rate probabilities can be very large, say $10^{19}\mathrm{s}^{-1}$, it would make it necessary to use very small time steps, of the order of 10^{-19}s, and an unfeasible amount of computational power would be necessary to obtain a reasonable realtime solution. Implicit schemes on the other hand are more stable and there is no time step condition to follow. The loss of accuracy is significant due to the properties of the equations, where the transition rate probabilities can vary substantially. This can be demonstrated by setting up one of the rate equations for a two level atom;

$$\begin{aligned} \frac{\partial n_1}{\partial t} + \nabla \cdot (n_1 \mathbf{u}) &= n_2 P_{21} - n_1 P_{12} \\ \frac{n_1^{k+1,m} - n_1^{k,m}}{\Delta t} + u \frac{n_1^{k,m} - n_1^{k,m-1}}{\Delta x} &= n_2^{k,m} P_{21}^{k,m} - n_1^{k,m} P_{12}^{k,m} \end{aligned}$$

$$n_1^{k+1,m} = n_1^{k,m} + \Delta t \left(n_2^{k,m} P_{21}^{k,m} - n_1^{k,m} P_{12}^{k,m} - u \frac{n_1^{k,m} - n_1^{k,m-1}}{\Delta x} \right)$$

where the k and m indices represent the time and space discretization, respectively. The advection term is discretized following a first order upwind scheme, in conjunction with the positive velocity u. If either $P_{12}^{k,m}$ or $P_{21}^{k,m}$ is very large, they will give rise to very dominating terms in the equations and overtake the equation more or less completely. Hence, to achieve better accuracy it is necessary to reduce the time step Δt, and the problem again becomes unfeasible time wise. The problem is solved by separating the equations using operator splitting, solving the lefthand side of the equations using implicit schemes and then using the solution in an explicit scheme to achieve a final solution.

Before each time step in the simulation, and for each level i, the continuity equation

$$\frac{\partial n_i^o}{\partial t} = -\nabla \cdot (n_i^o \mathbf{u}) \tag{5.10}$$

is solved using a first- order upwind scheme, where n_i^o are the old values of n_i. The reason for choosing this scheme is to prevent negative population densities of the level constituents due to the steep gradients in the level populations, where higher order schemes would not. Equation 5.10 is then explicitly advected in time:

$$n_i^* = \frac{\partial n_i^o}{\partial t} \Delta t + n_i^o \tag{5.11}$$

with timestep Δt.

The radiative MHD equations are then solved for the next timestep, resulting in a new Δt, which is utilized to solve the second part of the operator splitting,

$$\frac{\partial n_i}{\partial t} = \sum_{j \neq i}^{N_l} n_j P_{ji} - n_i \sum_{j \neq i}^{N_l} P_{ij}. \tag{5.12}$$

Here, the result of equation 5.11, n_i^*, and a first order forward difference method is used to discretize $\frac{\partial n_i}{\partial t} = \frac{n_i - n_i^*}{\Delta t}$, result in the set of equations:

$$n_i(1 - \Delta t \sum_{j \neq i}^{N_l} P_{ij}) - \Delta t \sum_{j \neq i}^{N_l} n_j P_{ji} = n_i^*. \tag{5.13}$$

Which is a set of linear equations $\mathbf{n} = \mathbf{A}^{-1}\mathbf{n}^*$, with a $N_l \times N_l$ rate matrix $\mathbf{A}$ with elements $A_{ii} = (1 + \Delta t \sum_{j \neq i} P_{ij})$ and $A_{ij} = -\Delta t P_{ji}$.

Particle conservation is enforced by replacing the rate equation which holds the largest ion concentration, with the equation of particle conservation (5.9). By doing so the total element population density of the model atom is kept coupled to the overall mass density in the experiment. This provides additional stability and accuracy to the solution, however, it is not necessary to achieve a unique solution of the equations.

The rate matrix is found at every grid point in the computational domain using the temperature and mass density of the cell to calculate the respective population and depopulation probabilities, P_{ij}, following the methods presented in section 2.3 in Paper I (Olluri et al., 2013b).

The rate matrix $\mathbf{A}$ is inverted using the **LAPACK** (Anderson et al., 1999) routine **DGESV** for general matrix inversion.

n_i^o is now n_i, and the procedure is repeated for every time step.

The level population densities, $\mathbf{n}$, are written to file in separate snapshots, parallel with the other Bifrost MHD variables (ρ, $\mathbf{u}$, e, $\mathbf{B}$), at time intervals dictated by the experiment setup file.

There is additional flexibility implemented:

- Instead of starting the experiment from an SE solution, it is possible to start from an existing set of $\mathbf{n}$ from already made snapshots.
- The level population densities can be saved in the auxiliary file together with the Bifrost associated variables (temperature, joule heating, etc).

- After sufficient time is achieved including non–equilibrium ionization, it might be of interest to study the departure from equilibrium by comparing the non–equilibrium population densities with the equivalent SE solution. It is therefore possible to to solve the SE equations additionally post run, from an existing set of Bifrost snapshots and auxiliary files.

5.4.3 Post run evaluation

An important fact to remember when using the non–equilibrium ionization solver is to consider the original approximation in the code, the optically thin approximation, which translates to the assumption of no contribution from radiation in the source and sink terms in Eq. 5.7. The assumption is only valid as long as the optical depth is less than 1. For purely Doppler broadening in the line profile, the optical depth τ_ν of a ray of light traveling a distance z is

$$\tau_\nu = \frac{\pi e^2}{m_e c} f_{lu} \frac{c}{\nu} \sqrt{\frac{m}{2\pi k_B}} \int_0^z \frac{n_l}{\sqrt{T}} dz. \tag{5.14}$$

where e is the electron charge, m_e the electron mass, f_{lu} the oscillator strength between the upper and lower level, m the mass of the emitting ion, c the speed of light, ν the frequency of the spectral line, n_l the lower level of the transition, and T the temperature. By using T and n_l resulting from a simulation, the assumption can be validated. It is therefore possible to justify the assumption by calculating the optical depth of the emission line under consideration, hence, making sure that the optical depth is smaller then 1 before initiation further analysis on the data.

5.5 Project results

Most of the time of this Ph.D work has gone in developing the numerical scheme and implementing the non–equilibrium solver into the Bifrost structure. However, the product in which the candidate will be evaluated on is the "fruit of" this labor; which are three scientific papers published (or in the process of being) in international peer-reviewed journals.

5.5.1 Paper I :

The first paper (Olluri et al., 2013b) is a methodology paper, where the non–equilibrium (NEQ) ionization solver is presented: The implementation of the rate equations in Bifrost, how the transition probabilities are calculated using the DIPER atomic files and test the optical thin approximation on the results. The implementation is validated through a set of tests designed to reproduce previous reported results.

The first test considers a 1D scenario, where the C IV ion is studied in a static atmosphere with advection through a temperature gradient. By varying the advection velocity between 1 ms^{-1} and 100 kms^{-1} in both up flow and down flow cases through the temperature gradient, the results of Joselyn et al. (1979b) are reproduced, that ionization equilibrium is disrupted already from relatively low velocities (1 km s^{-1}).

The next set of test considers 2D atmosphere models of previous well tested snapshots from experiments designed to be fairly close to solar parameters. The implementation of the rate equations is tested by comparing the NEQ ionization results with equivalent SE results solving the SE equations of the same model, when using CHIANTI SE contribution functions and when using the empirical atmosphere model Fal–C. The resulting emissivities, ion fractions and optical depths for all test cases mentioned are investigated, concluding that the solution holds for all optically thin ions of choice. The importance of the optical thin approximation test of the solutions is emphasized, due to ions originally assumed to be from optically thin regions of the atmosphere, may be advected to regions where the assumption does not hold due to the proper treatment of the ionization balance.

The last test considers the effect of a simplified nano-flare in the corona on the transition region C IV ion population density and the coronal Fe XII ion population density, in a 2D loop model similar to the one presented in Gudiksen et al. (2011). Significant differences when comparing the SE and NEQ population densities of the ions are found.

The C IV ion population density is unaffected by the nano-flare in the region of heat deposition, but the emerging chromospheric evaporation have an effect in the transition region through the emerging velocities, causing the resulting emission to originate from a wider region of the atmosphere when the ionization balance is treated properly than what is otherwise found in SE.

The Fe XII ion population density, on the other hand, is directly effected by the nano-flare. While the Fe XII ion population density instantaneously react to the local changes in the environment, ionizing to higher ionization stages in SE, the long ionization times in NEQ cause a lag, allowing the temperature to increase and then decrease due to thermal conduction, before they have time to ionize to higher ionization stages. The emerging velocities due to chromospheric evaporation makes advection important in the rate equations, leading to formation of ionization fronts. NEQ ionization lead to lower population densities of Fe XII, originating from higher layers of the atmosphere, when compared to similar SE results.

The authors conclude that the implementation in Bifrost is completely general, and can be run in 1D, 2D as well as 3D, and that the implementation of the NEQ ionization solver behaves as expected and give correct solutions of the rate equations.

5.5.2 Paper II:

In the second paper (Olluri et al., 2013a) of this compilation the electron density diagnostic technique of intensity line ratios developed by Munro et al. (1971) is investigated. The method exploits the scenario where the corona approximation break down, and consider the ratio of the emissivity of a spectral line formed by a stable level transition to a spectral line formed by a metastable level transition. The method assumes statistical equilibrium (SE) conditions, and an identity between the emissivity ratio and intensity ratio. Spectral lines from the beryllium-isoelectronic sequence and the boron-isoelectronic sequence are usually used because the temperature variations of the level populations are negligible compared to the changes in ion concentration, hence suited for electron density diagnostics.

Many previous studies has criticized the method, and found it to also be critically dependent on temperature (Loulergue and Nussbaumer, 1974), with misleading results from the assumption of the identity between the observed intensity and calculated emissivity (Flower and Nussbaumer, 1975). Additionally, 1D models have shown large NEQ effects on the emission and hence also in the density diagnostics of this method (Raymond and Dupree, 1978; Feldman, 1992b; Feldman et al., 1992; Doyle et al., 2012).

Due to the many assumptions in the method the resulting electron density has several interpretations; the density at the particular temperature for which the comparing emissivity ratio is calculated at (Keenan et al., 2009), the density in the volume where the contribution function for the particular spectral line peaks (Loulergue and Nussbaumer, 1974) or a weighted mean electron density over the line of sight (Munro et al., 1971).

The advanced, highly realistic solar atmosphere model Bifrost makes it possible to study the solar atmosphere as a whole, hence, giving an appropriate tool to understand the emerging emission throughout the line of sight and the diagnostics techniques usually implemented in observational studies. The NEQ ionization solver developed in Olluri et al. (2013b) makes it is possible to also investigate the techniques including a proper treatment of the ionization balance. The results of the 3D solar atmosphere simulation, which also solves the rate equations of a 14 level atomic model of oxygen, show that all oxygen ions are out of ionization equilibrium, and a high ion fraction of all ions are found at both lower and higher temperatures than their equilibration temperature.

The study considers the method of intensity ratio electron density diagnostics using the O IV 140.1 nm and 140.4 nm spectral lines from the beryllium-isoelectronic sequence;

$$\text{ratio} = \frac{2s^2 2p^2\, P_{3/2} - 2s2p^2\, {}^4P_{5/2}}{2s^2 2p^2\, P_{3/2} - 2s2p^2\, {}^4P_{3/2}}. \tag{5.15}$$

This makes it possible to construct an emissivity ratio curve at the equilibra-

tion temperature of O IV, $\log_{10}$ T= 5.15 as function of the electron density. Because the O IV ion is out of ionization equilibrium, the deduced electron density obtained with this method is up to an order of magnitude higher than the electron density at $\log_{10}$ T = 5.15 from the 3D model. The method is, on the other hand, able to produce more or less identical electron densities as the electron density at formation temperature if the ion populations are calculated under SE conditions.

The derived NEQ electron density from the line ratio technique is not the electron density from the peak of the contribution functions of the two spectral lines considered. The electron densities derived from the contribution functions are found to be more or less identical in SE and NEQ, where the NEQ effects entering the contribution function through the emissivity rapidly vanish as the electron density increase. The weighted mean electron densities from the simulation are very similar to the one derived from the line ratio, and reproduces the NEQ results when NEQ emissivities are used as weights, as well as the SE results for SE emissivity weights. This consistency is due to the fact that the NEQ effects do not disappear in the averaging of the electron density along each column due to the weighting by the NEQ emissivity. The results lead to the conclusion that the best explanation for the electron density derived using line ratio diagnostics is a weighted mean electron density of the particular spectral lines involved in the ratio. This technique of line ratio analyses for electron density diagnostics gives information about the electron density of the region where the emission emerge from and is not related to the formation temperature of the spectral line.

The methods used for observational data analysis are usually developed under certain conditions and assumptions. The results of the paper demonstrates the importance of numerical modeling in atmospheric diagnostics of the Sun, specially when including NEQ ionization, because the assumption of SE is so fundamental in these methods.

5.5.3 Paper III:

The last paper (Olluri et al., 2013c) produced for this Ph.D work deals with synthetic spectra of 3D numerical models, where the goal is to see how well the models are able to reproduce solar observables formed in the TR and lower corona, and therefore show that they are tools that can be used to model solar emission, and thereby also a tool that can be used for improving the general understanding of the phenomena that occur in this region of the atmosphere. The line intensities, the linewidths, and the line shifts are investigated, and a report on how well the results reproduce observed data from HRTS, SUMER and EIS is given. This is done by constructing synthetic spectra of the SUMER C II 133.4 nm, Si IV 139.3 nm, Si IV 140.2 nm, O IV 139.9 nm, O IV 140.1 nm, O IV 140.4 nm, O IV 140.7 nm, and

Fe XII 134.9 nm lines, which are also in the wavelength range of the newly launched Interface Region Imaging Spectrograph (IRIS). Additionally, the study include the EIS EUV lines He II 25.6 nm and Fe XII 19.5 nm lines, and the O VI 103.1 nm line connecting the middle TR to the corona. The investigations are first performed under statistical equilibrium assumptions, and then by including effects of NEQ ionization.

By setting the silicon abundance to its deduced 'coronal' value (Feldman, 1992a) and reducing the oxygen abundance to $A_O = 8.69$ *i.e.* the Asplund et al. (2009) value, the emerging synthetic intensity of the models described here are able to reproduce the observed absolute intensities to within a factor two for the most important SUMER lines formed in the transition region. Using these abundance values it is found that the silicon to oxygen intensity ratios lies close to that which is observed.

The non–thermal linewidths reproduce the well known turnoff point around $2 - 3 \times 10^5$K, but with much lower values. The synthetic non–thermal linewidths are very sensitive to resolution, resulting in much smaller values than what is observed when considered at the native, 48 km, resolution of the numerical simulation. By coursing the resolution to the typical 'observed' resolution of 1 ″ the synthetic linewidths increases by some 20 %, increasing additionally when the data is convolved with a Gaussian point spread function (PSF), and thus lying closer to what is observed. Structure on the Sun is found on much smaller scales than what is possible to model at the resolution of the presented simulations, and therefore it is believed that the discrepancy in Doppler width is real. However, the result does to some extent imply that observational linewidths reported so far are a consequence of their 1″ resolution. It is thus expected that the IRIS instrument, with a spatial resolution of $^1/_3$″ will produce narrower lines on average.

Observed Doppler shifts show a persistent redshift for lines formed at TR temperatures (Doschek et al., 1976), peaking at 10 km s^{-1} at temperatures of 10^5 K while decreasing towards higher temperatures with indications of average blueshifts for coronal lines (Peter, 1999). The average synthetic Doppler shifts reproduce this and are more or less independent of the resolution chosen to compute them. It is worth noticing that the average Doppler shifts are quite dependent on the type of region considered, where footpoint emission seems to be shifted significantly towards the blue as compared to the rest of the computational domain.

The Doppler shift correlations reported by Doschek (2006) for the TR lines and the Doppler shift to non–thermal linewidth correlations of the Fe XII 19.5 nm line reported by Doschek et al. (2008) are reproduced. Additionally, the reported correlation between the non–thermal linewidth of any two TR line studies as reported by Chae et al. (1998) are reproduced, however, the intensity to linewidth correlations only match after a PSF is applied to the data. Correlation studies can thus lead to misinterpretations of atmospheric conditions, due to photon leakage (here represented by the

PSF) in the detectors.

By solving the rate equations it is found that all ions considered (Si IV, C IV and O IV), except the Fe XII ions, are out of ionization equilibrium for the tested model atmosphere, and that they on average emit at lower temperatures than what is assumed in SE. The resulting synthesized spectra, averaged over the full numerical box, show overall higher (roughly 20 %) intensities for the TR lines than what is found in SE.

The large NEQ effects on the intensity maps, non–thermal linewidths and Doppler shifts are almost lost with large integration times combined with low resolution, which at times can make the spectra appear similar to that found under the assumption of SE, but the NEQ effect are obvious when considering single snapshots at full resolution.

The fact that the ions are found at much lower temperatures means that the ions are emitting from deeper layers of the atmosphere, resulting in consequently sampling larger volumes along the line of sight, which lead to higher non–thermal linewidths in the spectra. The thermal linewidhs are overestimated by assuming thermal widths at the peak of formation temperature in SE, consequently underestimating the non–thermal linewidths.

The consequences of NEQ ionization are severe for diagnostics of the TR, as discussed for the electron density diagnostics using O IV lines in paper II (Olluri et al., 2013a) where an overestimation of more than one magnitude of the electron density was found. NEQ ionization will probably lead to misdiagnoses of the temperature as well, were it is common to use Si IV lines.

The findings shown that simulations can be trusted to produce data similar enough to observations to make meaningful and instructive comparisons with real solar observations. This study have demonstrated that the stellar atmosphere code Bifrost is able to reproduce observables compatible and comparable to observed solar data of the transition region.

List of included publications

Paper I : Olluri, K., Gudiksen, B. V. and Hansteen, V.
Non–equilibrium ionization in the Bifrost stellar atmosphere code
Astromomical Journal, Volume 145, Page 72 (2013)

Paper II : Olluri, K., Gudiksen, B. V. and Hansteen, V.
Non–equilibrium ionization effects on the density line ratio diagnostics of O IV
Astrophysical Journal, Volume 767, Page 43 (2013)

Paper III : Olluri, K., Gudiksen, B. V., Hansteen, V. and De Pontieu, B.
Synthezided spectra of optically thin emission lines produced by the Bifrost stellar atmosphere code, including non–equilibrium ionization effects: A study of the intensity, non–thermal linewidths and Doppler shifts
Submitted to The Astrophysical Journal (2013)

Other publications and presentations of the project results

Refereed Journals

Judge, P. G., de Pontieu, B., McIntosh, S. W. and Olluri, K
The Connection of Type II Spicules to the Corona
Astrophysical Journal, Volume 747, Page 158 (2012)

Conferences, Workshops and Schools

(O): Oral Presentation
(P): Poster Presentation

- *Non–equilibrium ionization of metals in the solar atmosphere*, Olluri, K., Solar Magnetism – USO Sumer School. ASTRON, Dwingeloo – The Netherlands, June 28-July 4, 2009 (O)
- *Non–equilibrium ionization of transition region elements in 3D numerical models*, Olluri, K., Hansteen, V. and Gudiksen, B. V., Fourth Hinode Science Meeting, Palermo – Italy, 11-15 October 2010 (P)

- *Non–equilibrium ionization in 3D numerical models*, Olluri, K., Hansteen, V. and Gudiksen, B. V., ESPM–13 Meeting, Rhodes – Greece, 12-16 September 2011 (P)

- *Non–equilibrium ionization in 3D numerical models*, Olluri, K., Hansteen, V. and Gudiksen, B. V., Fifth Hinode Science Meeting, Cambridge, Massachusetts – USA, 10-15 October 2011 (O)

- *New techniques and new insights into Solar Coronal Heating.* Olluri, K. and Hansteen, V., Transatlantic Science Week, Berkeley, CA – USA, 25-28 October 2011 (O)

- *Non–equilibrium ionization in 3D numerical models.* Olluri, K., Gudiksen, B. V. and Hansteen, V. SDO-4 / IRIS / Hinode Workshop, Monteray, CA – USA, 12-16 March 2012 (P)

- *Numerical models as tools for spectroscopy and diagnostics of the solar atmosphere.*Olluri, K., Gudiksen, B. V. and Hansteen, V. 1st SOLARNET - 3rd EAST/ATST meeting. Oslo – Norway, 5-8 August 2013 (O)

- *Synthezided spectra of optically thin emission lines produced by the Bifrost stellar atmosphere code*, Olluri, K., Gudiksen, B. V., Hansteen, V. and De Pontieu, B. Seventh Hinode Science Meeting, Takayama – Japan, 12-15 November 2013 (P)

Appendices

Appendix A

Line formation processes

Without going to much into detail we list a few of these of the line formation processes:

Induced absorption is the process when an incoming photon excite an electron in an atom or ion to a higher energy state; $\chi_l + h\nu \rightarrow \chi_u$, where χ is the energy of lower (l) and upper (u) level, and $h\nu$ the energy of the incoming photon of frequency ν.

Stimulated emission is the process when a bypassing photon from the radiation field stimulate a bound electron in a excited state, causing the electron to decay to a lower energy state and simultaneously emit an additional photon; $\chi_u + h\nu_i \rightarrow \chi_l + h\nu_i + h\nu_j$, where ν_i is the frequency of the incoming photon and ν_j the frequency of the emitted photon.

Spontaneous emission is the process when an excited electron spontaneously decays to a lower energy state, emitting a photon in the process; $\chi_u \rightarrow \chi_l + h\nu_i$.

Photo − ionization is the process when an incoming photon, with energy higher than the ionization energy of the ion (in ionization stage m), interacts with a electron of the ion, causing the electron to break from the bound state of the ion and become free; $\chi_i^m + h\nu \rightarrow \chi_j^{m+1} + e^{-1}$, where the indices i and j represent different energy states of the ions.

Radiative recombination is the process when a free electron is captured by an ion into one of the available energy states, χ_i, and the excess energy is emitted as a photon; $\chi_j^{m+1} + e^{-1} \rightarrow \chi_j^m + h\nu$.

Dielectronic recombination is a process involving two electrons: A free electron is captured by an ion, landing in an excited state and simultaneously a bound electron in the ion becomes excited. This doubly excited configuration stabilizes when one or both of the electrons falls back into vacancies of the lowest available states and emitting a photon; $\chi_{ij}^{m+1} + e^{-1} \rightarrow \chi_{gj}^m + h\nu$.

Dielectronic recombination can also result in **autoionization**, which is the process when an ion in a doublet excited state, spontaneously ionizes

without a influecing photon or particles; $\chi_{ij}^{m} \rightarrow \chi_{gj}^{m+1} + e^{-1}$.

Collisional ionization is the process when a free electron interacts with an ion, removing a bound electron from the ion configuration; $\chi_{i}^{m} + e^{-1} \rightarrow \chi_{j}^{m+1} + e^{-1} + e^{-1}$.

Three – body recombination is the opposite of collisional ionization. Here, two incoming electrons interact with an ion, one is catered by the ion while the other carries away the excess energy; $\chi_{j}^{m+1} + e^{-1} + e^{-1} \rightarrow \chi_{i}^{m} + e^{-1}$.

Collisional excitation is the process when a free electron interact with an ion, if the incoming electron has less energy then the ionization energy of the ion it will only excite one of the bound electrons in the ion, and scatter away with less energy; $\chi_{i}^{m} + e^{-1} \rightarrow \chi_{j}^{m} + e^{-1}$. While **collisional de–excitation/decay** happens when the incoming electron interacts with a bound electron in the ion, causing the bound electron to decay to a lower energy state, and scatter away from the interaction with more than the original energy; $\chi_{j}^{m} + e^{-1} \rightarrow \chi_{i}^{m} + e^{-1}$.

Coherent scattering is the easiest way of photon scattering, it is both isotropic and monochromatic, where the interacting bodies leave the scattering process in a new direction but with the same energy. An example is **Thomson scattering** where the incoming photon transfer momentum with the colliding free electron, changing the path of both while remaining with their original energy.

Non–coherent scattering processed are all inelastic scattering processes, where there is a energy transfer between the interacting bodies. An example is **Bremsstrahlung**, where electrons are inelastically scattered by ions, emitting a photon in the process. $\chi_{i}^{m} + e^{-1} \rightarrow \chi_{j}^{m} + e^{-1} + h\nu$.

Bibliography

Abbett, W. P. (2007). The Magnetic Connection between the Convection Zone and Corona in the Quiet Sun. *ApJ* , 665:1469–1488.

Anderson, E., Bai, Z., Bischof, C., Blackford, S., Demmel, J., Dongarra, J., Du Croz, J., Greenbaum, A., Hammarling, S., McKenney, A., and Sorensen, D. (1999). *LAPACK Users' Guide*. Society for Industrial and Applied Mathematics, Philadelphia, PA, third edition.

Antiochos, S. K. (1982). A dynamic model for the transition region. *NASA STI/Recon Technical Report N*, 83:29163.

Arnaud, M. and Rothenflug, R. (1985). An updated evaluation of recombination and ionization rates. *Astron. Astrophys. Suppl. Ser.*, 60:425–457.

Aschwanden, M. J. (2004). *Physics of the Solar Corona. An Introduction*. Praxis Publishing Ltd.

Asplund, M., Grevesse, N., Sauval, A. J., and Scott, P. (2009). The Chemical Composition of the Sun. *ARAA* , 47:481–522.

Asplund, M., Nordlund, Å., Trampedach, R., Allende Prieto, C., and Stein, R. F. (2000). Line formation in solar granulation. I. Fe line shapes, shifts and asymmetries. *A&A* , 359:729–742.

Athay, R. G. (1984). The origin of spicules and heating of the lower transition region. *ApJ* , 287:412–417.

Bartoe, J.-D. F., Brueckner, G. E., Cook, J. W., Dere, K. P., and Morrison, M. D., editors (1986). *Results from the NRL instruments on Spacelab 2*.

Beeck, B., Collet, R., Steffen, M., Asplund, M., Cameron, R. H., Freytag, B., Hayek, W., Ludwig, H.-G., and Schüssler, M. (2012). Simulations of the solar near-surface layers with the CO5BOLD, MURaM, and Stagger codes. *A&A* , 539:A121.

Berger, T. E., de Pontieu, B., Schrijver, C. J., and Title, A. M. (1999). High-resolution Imaging of the Solar Chromosphere/Corona Transition Region. *ApJL* , 519:L97–L100.

Borrini, G. and Noci, G. (1982). Non-equilibrium ionization in coronal loops. *Sol. Phys.* , 77:153–166.

Bradshaw, S. J. and Cargill, P. J. (2006). Explosive heating of low-density coronal plasma. *A&A* , 458:987–995.

Bradshaw, S. J. and Cargill, P. J. (2010). A New Enthalpy-Based Approach to the Transition Region in an Impulsively Heated Corona. *ApJL* , 710:L39–L43.

Bradshaw, S. J., Del Zanna, G., and Mason, H. E. (2004). On the consequences of a non-equilibrium ionisation balance for compact flare emission and dynamics. *A&A* , 425:287–299.

Bradshaw, S. J. and Klimchuk, J. A. (2011). What Dominates the Coronal Emission Spectrum During the Cycle of Impulsive Heating and Cooling? *ApJS* , 194:26.

Bradshaw, S. J. and Mason, H. E. (2003a). A self-consistent treatment of radiation in coronal loop modelling. *A&A* , 401:699–709.

Bradshaw, S. J. and Mason, H. E. (2003b). The radiative response of solar loop plasma subject to transient heating. *A&A* , 407:1127–1138.

Brandenburg, A. and Dobler, W. (2002). Hydromagnetic turbulence in computer simulations. *Computer Physics Communications*, 147:471–475.

Brekke, P. (1999). Observations of Transition Region Plasma. *Sol. Phys.* , 190:379–408.

Brković, A., Peter, H., and Solanki, S. K. (2003). Variability of EUV-spectra from the quiet upper solar atmosphere: Intensity and Doppler shift. *A&A* , 403:725–730.

Brueckner, G. E., Cook, J. W., and Dere, K. P. (1986). Results from the High Resolution Telescope and Spectrograph (HRTS) Experiment. In *Bulletin of the American Astronomical Society*, volume 18 of *Bulletin of the American Astronomical Society*, page 675.

Carlsson, M. and Leenaarts, J. (2012). Approximations for radiative cooling and heating in the solar chromosphere. *A&A* , 539:A39.

Carlsson, M., Stein, R. F., Nordlund, Å., and Scharmer, G. B. (2004). High resolution limb images synthesized from 3D MHD simulations. In Stepanov, A. V., Benevolenskaya, E. E., and Kosovichev, A. G., editors, *Multi-Wavelength Investigations of Solar Activity*, volume 223 of *IAU Symposium*, pages 233–234.

Carroll, B. W. and Ostlie, D. A. (2006). *An introduction to modern astrophysics and cosmology*.

Chae, J., Schühle, U., and Lemaire, P. (1998). SUMER Measurements of Nonthermal Motions: Constraints on Coronal Heating Mechanisms. *ApJ* , 505:957–973.

Chitta, L. P., Kariyappa, R., van Ballegooijen, A. A., DeLuca, E. E., Hasan, S. S., and Hanslmeier, A. (2013). Observations and Modeling of the Emerging Extreme-ultraviolet Loops in the Quiet Sun as Seen with the Solar Dynamics Observatory. *ApJ* , 768:32.

Culhane, J. L., Harra, L. K., James, A. M., Al-Janabi, K., Bradley, L. J., Chaudry, R. A., Rees, K., Tandy, J. A., Thomas, P., Whillock, M. C. R., Winter, B., Doschek, G. A., Korendyke, C. M., Brown, C. M., Myers, S., Mariska, J., Seely, J., Lang, J., Kent, B. J., Shaughnessy, B. M., Young, P. R., Simnett, G. M., Castelli, C. M., Mahmoud, S., Mapson-Menard, H., Probyn, B. J., Thomas, R. J., Davila, J., Dere, K., Windt, D., Shea, J., Hagood, R., Moye, R., Hara, H., Watanabe, T., Matsuzaki, K., Kosugi, T., Hansteen, V., and Wikstol, Ø. (2007). The EUV Imaging Spectrometer for Hinode. *Sol. Phys.* , 243:19–61.

Doschek, G. A. (2006). Doppler Shift Correlations in the Solar Transition Region. *ApJ* , 649:515–528.

Doschek, G. A., Bohlin, J. D., and Feldman, U. (1976). Doppler wavelength shifts of transition zone lines measured in SKYLAB solar spectra. *ApJL* , 205:L177–L180.

Doschek, G. A., Warren, H. P., Mariska, J. T., Muglach, K., Culhane, J. L., Hara, H., and Watanabe, T. (2008). Flows and Nonthermal Velocities in Solar Active Regions Observed with the EUV Imaging Spectrometer on Hinode: A Tracer of Active Region Sources of Heliospheric Magnetic Fields? *ApJ* , 686:1362–1371.

Doyle, J. G., Giunta, A., Singh, A., Madjarska, M. S., Summers, H., Kellett, B. J., and O'Mullane, M. (2012). The Diagnostic Potential of Transition Region Lines Undergoing Transient Ionization in Dynamic Events. *Sol. Phys.* , 280:111–124.

Doyle, J. G., Madjarska, M. S., Roussev, I., Teriaca, L., and Giannikakis, J. (2002a). Temporal variability in the Doppler-shift of solar transition region lines. *A&A* , 396:255–267.

Doyle, J. G., Madjarska, M. S., Roussev, I., Teriaca, L., and Giannikakis, J. (2002b). Temporal variability in the Doppler-shift of solar transition region lines. *A&A* , 396:255–267.

Dupree, A. K., Moore, R. T., and Shapiro, P. R. (1979). Nonequilibrium ionization in solar and stellar winds. *ApJL* , 229:L101–L105.

Edgar, R. J. and Esser, R. (2000). Nonequilibrium Ionization and First Ionization Potential Effect Diagnostics. *ApJL* , 538:L167–L170.

Edlén, B. (1943). Die Deutung der Emissionslinien im Spektrum der Sonnenkorona. Mit 6 Abbildungen. *Zeitschrift für Astrophysik*, 22:30.

Feldman, U. (1992a). Elemental abundances in the upper solar atmosphere. *Physica Scripta*, 46:202–220.

Feldman, U. (1992b). Transitions from metastable levels emitted during short-duration bursts - How valid are their calculated intensities? *ApJ* , 385:758–762.

Feldman, U., Laming, J. M., Mandelbaum, P., Goldstein, W. H., and Osterheld, A. (1992). A burst model for line emission in the solar atmosphere. II - Coronal extreme ultraviolet lines. *ApJ* , 398:692–697.

Flower, D. R. and Nussbaumer, H. (1975). On the extreme ultraviolet solar emission of B-like ions - O IV. *A&A* , 45:145–150.

Fontenla, J. M., Avrett, E. H., and Loeser, R. (1993). Energy balance in the solar transition region. III - Helium emission in hydrostatic, constant-abundance models with diffusion. *ApJ* , 406:319–345.

Freytag, B., Steffen, M., Wedemeyer-Böhm, S., Ludwig, H.-G., Leenaarts, J., Schaffenberger, W., Allard, F., Chiavassa, A., Höfner, S., Kamp, I., and Steiner, O. (2010). CO5BOLD: COnservative COde for the COmputation of COmpressible COnvection in a BOx of L Dimensions with l=2,3. Astrophysics Source Code Library.

Griem, H. R. (1964). *Plasma spectroscopy.* New York: McGraw-Hill.

Grotrian, W. (1939). Sonne und Ionosphäre. *Naturwissenschaften*, 27:569–577.

Gudiksen, B. V., Carlsson, M., Hansteen, V. H., Hayek, W., Leenaarts, J., and Martínez-Sykora, J. (2011). The stellar atmosphere simulation code Bifrost. Code description and validation. *A&A* , 531:A154.

Guerreiro, N., Hansteen, V., and De Pontieu, B. (2013). The Cycling of Material between the Solar Corona and Chromosphere. *ApJ* , 769:47.

Gustafsson, B., Bell, R. A., Eriksson, K., and Nordlund, A. (1975). A grid of model atmospheres for metal-deficient giant stars. I. *A&A* , 42:407–432.

Handy, B. N., Tarbell, T. D., Wolfson, C. J., Korendyke, C. M., and Vourlidas, A. (1999). Calibrated H I Lyman α Observations with TRACE. *Sol. Phys.* , 190:351–361.

Hansteen, V. (1993). A new interpretation of the redshift observed in optically thin transition region lines. *ApJ* , 402:741–755.

Hansteen, V. H., Betta, R., and Carlsson, M. (2000). Rapid intensity and velocity variations in solar transition region lines. *A&A* , 360:742–760.

Hansteen, V. H., Hara, H., De Pontieu, B., and Carlsson, M. (2010). On Redshifts and Blueshifts in the Transition Region and Corona. *ApJ* , 718:1070–1078.

Hansteen, V. H. and Wikstøl, Ø. (1994). Transition region line-shifts in the rebound shock spicule model. *Space Sci. Rev.*, 70:103–106.

Hara, H., Watanabe, T., Harra, L. K., Culhane, J. L., Young, P. R., Mariska, J. T., and Doschek, G. A. (2008). Coronal Plasma Motions near Footpoints of Active Region Loops Revealed from Spectroscopic Observations with Hinode EIS. *ApJL* , 678:L67–L71.

Harrison, R. A., Sawyer, E. C., Carter, M. K., Cruise, A. M., Cutler, R. M., Fludra, A., Hayes, R. W., Kent, B. J., Lang, J., Parker, D. J., Payne, J., Pike, C. D., Peskett, S. C., Richards, A. G., Gulhane, J. L., Norman, K., Breeveld, A. A., Breeveld, E. R., Al Janabi, K. F., McCalden, A. J., Parkinson, J. H., Self, D. G., Thomas, P. D., Poland, A. I., Thomas, R. J., Thompson, W. T., Kjeldseth-Moe, O., Brekke, P., Karud, J., Maltby, P., Aschenbach, B., Bräuninger, H., Kühne, M., Hollandt, J., Siegmund, O. H. W., Huber, M. C. E., Gabriel, A. H., Mason, H. E., and Bromage, B. J. I. (1995). The Coronal Diagnostic Spectrometer for the Solar and Heliospheric Observatory. *Sol. Phys.* , 162:233–290.

Heinemann, T., Dobler, W., Nordlund, Å., and Brandenburg, A. (2006). Radiative transfer in decomposed domains. *A&A* , 448:731–737.

Hyman, J. M. (1979). A method of lines approach to the numerical solution of conservation laws. In *Advances in Computer Methods for Partial Differential Equations - III*, pages 313–321.

Joselyn, J., Munro, R. H., and Holzer, T. E. (1979a). Mass flow and the validity of ionization equilibrium on the sun. *Sol. Phys.* , 64:57–69.

Joselyn, J. A., Munro, R. H., and Holzer, T. E. (1979b). The validity of ionization equilibrium in highly ionized astrophysical plasmas. *ApJS* , 40:793–813.

Judge, P. G. and Meisner, R. W. (1994). The 'HAO spectral diagnostics package' (HAOS-Diaper). In J. J. Hunt, editor, *Solar Dynamic Phenomena and Solar Wind Consequences, the Third SOHO Workshop*, volume 373 of *ESA Special Publication*, pages 67–+.

Judge, P. G., Woods, T. N., Brekke, P., and Rottman, G. J. (1995). On the Failure of Standard Emission Measure Analysis for Solar Extreme-Ultraviolet and Ultraviolet Irradiance Spectra. *ApJL* , 455:L85.

Keenan, F. P., Crockett, P. J., Aggarwal, K. M., Jess, D. B., and Mathioudakis, M. (2009). Ultraviolet and extreme-ultraviolet line ratio diagnostics for O IV. *A&A* , 495:359–362.

Klimchuk, J. A., Ofman, L., and Davila, J. M. (1997). A Self-Consistent Model for the Resonant Heating of Coronal Loops: the Effects of Coupling with the Chromosphere. In *AAS/Solar Physics Division Meeting #28*, volume 29 of *Bulletin of the American Astronomical Society*, page 909.

Klimchuk, J. A., Tripathi, D., Bradshaw, S. J., and Mason, H. E. (2012). Understanding Coronal Heating with Emission Measure Distributions. In *American Astronomical Society Meeting Abstracts #220*, volume 220 of *American Astronomical Society Meeting Abstracts*, page #423.02.

Loulergue, M. and Nussbaumer, H. (1974). The Chromosphere-corona Transition Region as Seen in C M. *A&A* , 34:225.

Magic, Z., Collet, R., Asplund, M., Trampedach, R., Hayek, W., Chiavassa, A., Stein, R. F., and Nordlund, Å. (2013). The Stagger-grid: A grid of 3D stellar atmosphere models. I. Methods and general properties. *A&A* , 557:A26.

Mariska, J. T. (1992). *The solar transition region*. Cambridge Astrophysics Series. Cambridge University Press, New York.

Mariska, J. T., Feldman, U., and Doschek, G. A. (1978). Measurements of extreme-ultraviolet emission-line profiles near the solar limb. *ApJ* , 226:698–705.

Munro, R. H., Dupree, A. K., and Withbroe, G. L. (1971). Electron Densities Derived from Line Intensity Ratios: Beryllium Isoelectronic Sequence. *Sol. Phys.* , 19:347–355.

Muthsam, H. J., Kupka, F., Löw-Baselli, B., Obertscheider, C., Langer, M., and Lenz, P. (2010). ANTARES - A Numerical Tool for Astrophysical RESearch with applications to solar granulation. *New A* , 15:460–475.

Noci, G., Spadaro, D., Zappala, R. A., and Antiochos, S. K. (1989a). Mass flows and the ionization states of coronal loops. *ApJ* , 338:1131–1138.

Noci, G., Spadaro, D., Zappala, R. A., and Antiochos, S. K. (1989b). Subsonic mass flows and ionization state in coronal loops. *memsai*, 60:55–64.

Nordlund, A. (1982). Numerical simulations of the solar granulation. I - Basic equations and methods. *A&A* , 107:1–10.

Nordlund, . and Galsgaard, K. (1995). A 3D MHD code for parallel Computers. http://www.astro.ku.dk/ kg.

Olluri, K., Gudiksen, B. V., and Hansteen, V. H. (2013a). Non-equilibrium Ionization Effects on the Density Line Ratio Diagnostics of O IV. *ApJ* , 767:43.

Olluri, K., Gudiksen, B. V., and Hansteen, V. H. (2013b). Non-equilibrium Ionization in the Bifrost Stellar Atmosphere Code. *AJ* , 145:72.

Olluri, K., Gudiksen, B. V., Hansteen, V. H., and De Pontieu, B. (2013c). Synthesized spectra of optically thin emission lines produced by the Bifrost stellar atmosphere code, including non equilibrium ionization effects: A study of the intensity, non-thermal linewidths and Doppler shifts. *submitted*.

Pereira, T. M. D., Asplund, M., Collet, R., Thaler, I., Trampedach, R., and Leenaarts, J. (2013). How realistic are solar model atmospheres? *A&A* , 554:A118.

Peter, H. (1999). Doppler shifts of solar UV emission lines and the source region of the (fast) solar wind. In Suess, S. T., Gary, G. A., and Nerney, S. F., editors, *American Institute of Physics Conference Series*, volume 471, pages 281–284.

Peter, H., Gudiksen, B. V., and Nordlund, Å. (2006). Forward Modeling of the Corona of the Sun and Solar-like Stars: From a Three-dimensional Magnetohydrodynamic Model to Synthetic Extreme-Ultraviolet Spectra. *ApJ* , 638:1086–1100.

Pottasch, S. R. (1964). On the Interpretation of the Solar Ultraviolet Emission Line Spectrum. *Space Sci. Rev.*, 3:816–855.

Raymond, J. C. and Doyle, J. G. (1981). Emissivities of strong ultraviolet lines. *ApJ* , 245:1141–1144.

Raymond, J. C. and Dupree, A. K. (1978). C III density diagnostics in nonequilibrium plasmas. *ApJ* , 222:379–383.

Reale, F. (2010). Coronal Loops: Observations and Modeling of Confined Plasma. *Living Reviews in Solar Physics*, 7:5.

Robinson, F. J., Demarque, P., Li, L. H., Sofia, S., Kim, Y.-C., Chan, K. L., and Guenther, D. B. (2003). Three-dimensional convection simulations of the outer layers of the Sun using realistic physics. *MNRAS*, 340:923–936.

Rutten, R. J. (2003). *Radiation Transfer in Stellar Atmospheres*.

Shull, J. M. and van Steenberg, M. (1982). The ionization equilibrium of astrophysically abundant elements. *ApJS* , 48:95–107.

Skartlien, R. (2000). A Multigroup Method for Radiation with Scattering in Three-Dimensional Hydrodynamic Simulations. *Astrophysical Journal*, 536:465–480.

Spadaro, D., Lanza, A. F., Lanzafame, A. C., Karpen, J. T., Antiochos, S. K., Klimchuk, J. A., and MacNeice, P. J. (2003). A Transient Heating Model for Coronal Structure and Dynamics. *ApJ* , 582:486–494.

Spadaro, D., Leto, P., and Antiochos, S. K. (1994). Observational tests for nonequilibrium ionization in the solar corona. *ApJ* , 427:453–458.

Spitzer, L. (1956). *Physics of Fully Ionized Gases*.

Stein, R. F. and Nordlund, A. (1998). Simulations of Solar Granulation. I. General Properties. *ApJ* , 499:914.

Vögler, A., Shelyag, S., Schüssler, M., Cattaneo, F., Emonet, T., and Linde, T. (2005). Simulations of magneto-convection in the solar photosphere. Equations, methods, and results of the MURaM code. *A&A* , 429:335–351.

Walsh, R. W. and Galsgaard, K. (2000). Modelling the Sun's Magnetic Carpet: Energy Release in the Corona due to the Relative Motion of Magnetic Fragments. In *AAS/Solar Physics Division Meeting #31*, volume 32 of *Bulletin of the American Astronomical Society*, page 845.

Warren, H. P. (2006). NRLEUV 2: A new model of solar EUV irradiance variability. *Advances in Space Research*, 37:359–365.

Wilhelm, K., Curdt, W., Marsch, E., Schühle, U., Lemaire, P., Gabriel, A., Vial, J.-C., Grewing, M., Huber, M. C. E., Jordan, S. D., Poland, A. I., Thomas, R. J., Kühne, M., Timothy, J. G., Hassler, D. M., and Siegmund, O. H. W. (1995). SUMER - Solar Ultraviolet Measurements of Emitted Radiation. *Sol. Phys.* , 162:189–231.

Wilhelm, K., Dwivedi, B. N., Marsch, E., and Feldman, U. (2004). Observations of the Sun at Vacuum- Ultraviolet Wavelengths from Space. Part I: Concepts and Instrumentation. *Space Sci. Rev.*, 111:415–480.

Wilhelm, K., Marsch, E., Dwivedi, B. N., and Feldman, U. (2007). Observations of the Sun at Vacuum-Ultraviolet Wavelengths from Space. Part II: Results and Interpretations. *Space Sci. Rev.*, 133:103–179.

Winebarger, A. R., Schmelz, J. T., Warren, H. P., Saar, S. H., and Kashyap, V. L. (2011). Using a Differential Emission Measure and Density Measurements in an Active Region Core to Test a Steady Heating Model. *ApJ* , 740:2.

Woodgate, B. E., Brandt, J. C., Kalet, M. W., Kenny, P. J., Tandberg-Hanssen, E. A., Bruner, E. C., Beckers, J. M., Henze, W., Knox, E. D., and Hyder, C. L. (1980). The Ultraviolet Spectrometer and Polarimeter on the Solar Maximum Mission. *Sol. Phys.* , 65:73–90.

Part II

Papers

Paper I

Non–equilibrium ionization in the Bifrost stellar atmosphere code
Olluri, K., Gudiksen, B. V. and Hansteen, V.
AJ, 145, 72 (2013)

The Astronomical Journal, 145:72 (16pp), 2013 March doi:10.1088/0004-6256/145/3/72

NON-EQUILIBRIUM IONIZATION IN THE BIFROST STELLAR ATMOSPHERE CODE

K. Olluri[1,2], B. V. Gudiksen[1,2], and V. H. Hansteen[1,2]
[1] Institute of Theoretical Astrophysics, University of Oslo, P.O. Box 1029, Blindern, NO-0315 Oslo, Norway; kosovare.olluri@astro.uio.no
[2] Center of Mathematics for Applications, University of Oslo, P.O. Box 1053, Blindern, NO-0316 Oslo, Norway
Received 2012 September 17; accepted 2012 December 21; published 2013 February 8

ABSTRACT

The chromosphere and transition region have for the last 20 years been known to be quite dynamic layers of the solar atmosphere, characterized by timescales shorter than the ionization equilibrium timescales of many of the ions dominating emission in these regions. Due to the fast changes in the properties of the atmosphere, long ionization and recombination times can lead these ions to being found far from their equilibrium temperatures. A number of the spectral lines that we observe can therefore not be expected a priori to reflect information about local quantities such as the density or temperature, and interpreting observations requires numerical modeling. Modeling the ionization balance is computationally expensive and has earlier only been done in one dimension. However, one-dimensional models can primarily be used to investigate the possible importance of a physical effect, but cannot verify or disprove the importance of that effect in the fully three-dimensional solar atmosphere. Here, using the atomic database package DIPER, we extend one-dimensional methods and implement a solver for the rate equations of the full three-dimensional problem, using the numerical code Bifrost. We present our implementation and report on a few test cases. We also report on studies of the important C IV and Fe XII ions in a semi-realistic two-dimensional solar atmosphere model, focusing on differences between statistical equilibrium and non-equilibrium ionization results.

Key words: atomic processes – magnetohydrodynamics (MHD) – methods: numerical – Sun: atmosphere – Sun: transition region – techniques: spectroscopic

1. INTRODUCTION

The outer solar atmosphere consists of inhomogeneous plasma with strong vertical stratification. It is a region with many dynamic events and it is characterized by rapid changes on many size scales. Temperatures can vary from a minimum of a couple of thousand degrees in the chromosphere, to several million degrees in the corona, while the mass density decreases rapidly from the photosphere toward the upper chromosphere, flattening out in the corona as a result of the large coronal scale height. The magnetic field is rooted deep in the convection zone, and when it reaches the photosphere, it has been frayed by convective motions to the point where the majority of the flux is present in the form of small flux concentrations, the strongest of which can be observed as bright points in the spectral *G* band. Photospheric motions are able to advect these small flux concentrations, which send a wealth of Alfvénic and magnetosonic wave modes up into the chromosphere where most steepen into shocks, refract, or are reflected off the steep transition region temperature gradient; some percentage of the wave energy is transmitted into the corona. From above, energy is transported from the corona down into the transition region and upper chromosphere via thermal conduction. In this highly dynamic environment, where atmospheric conditions change significantly on timescales of only a few minutes (Brekke 1999; Berger et al. 1999), many ions will not be able to reach thermal equilibrium with the surroundings.

In 1964, Griem discussed the relaxation times for ionization and excitation of the plasma constituents, raising the concern that the plasma might be out of ionization equilibrium when the dynamical timescales are shorter than the recombination times of the ions. Griem (1964) states that significant flows through temperature gradients can disrupt ionization equilibrium. This work was taken one step further by Joselyn et al. (1979b), where the consequences of a steady flow through a range of temperature gradients were investigated, concluding that the validity of the ionization equilibrium must not be taken for granted. In their subsequent work on the validity of the ionization equilibrium on the Sun, they studied ionization equilibrium for the quiet Sun, coronal hole, and network. Analyzing emission lines from the transition region, they conclude that iron lines are generally in equilibrium for steady flows of up to 20 km s^{-1}, while for carbon and oxygen, ionization equilibrium is an invalid assumption for flow velocities as low as 1 km s^{-1}. All results are model independent, and given the vast range of velocities observed in the Sun, make inversions of temperatures and densities from spectroscopic diagnostics of transition region lines questionable.

Hansteen (1993) developed a one-dimensional numerical model solving hydrodynamic equations, including the effects of non-equilibrium (NEQ) ionization on radiative losses and on the evolution of the plasma's internal energy, studying the dynamic response of a coronal loop to energy released as heat near the loop apex. Hansteen (1993) found that the radiative loss may change by a factor of two during the loop evolution as a result of flows and waves, confirming the importance of NEQ ionization in the line-forming process. Similar one-dimensional loop models using radiative losses due to EUV line emission based on time-dependent ionization have been performed by Bradshaw & Mason (2003a, 2003b), Müller et al. (2003, 2004), Bradshaw & Cargill (2006), Reale & Orlando (2008), and Bradshaw & Klimchuk (2011).

To properly understand the full structure of the solar atmosphere, investigations should be carried out in three dimensions. Peter et al. (2006) studied EUV spectra based on a time-dependent three-dimensional model of the solar corona, but because of computational time constraints, had to assume ionization equilibrium. They also concluded that this simplification breaks down when cool transition region lines are investigated, and in general when flows become large.

In recent years the computational power to solve the full three-dimensional radiative MHD model of the solar atmosphere, including the rate equations, has become available. In this paper,

we present our method of implementing and solving the ionization rate equations in the three-dimensional numerical model Bifrost (Gudiksen et al. 2011). We present our results through a set of tests in one and two dimensions, studying the effect of advection on the rate equations as well as the consequences of rapid heating (e.g., mimicking nano-flares) in the corona, focusing on differences between statistical equilibrium (SE) ionization and NEQ ionization. We have deliberately chosen to present the result in one and two dimensions in this paper because it is easy to construct test cases showing the validity of our implementation of the rate equations and isolating the effect of NEQ ionization.

Full three-dimensional simulations of a realistic solar atmosphere including detailed investigations of the ionization balance of a number of elements will follow in a later paper.

2. METHOD

In this section, we describe the implementation of an ionization rate equation solver enabling the Bifrost code to follow ionization states of ions in simulations of the solar atmosphere.

Transition probabilities are calculated using atomic data parameters from atom models created with the atomic diagnostic package DIPER (HAO Spectral Diagnostic Package For Emitted Radiation; Judge & Meisner 1994), and the implementation of this is discussed along with the implementation of the rate equations in the numerical model.

2.1. The Numerical Model

The fully parallelized three-dimensional solar atmosphere model Bifrost has been used to solve the radiative MHD equations, modeling the solar atmosphere from the upper convection zone to the lower corona. The code includes non-gray, non-LTE radiative transport in the photosphere and lower chromosphere, and magnetic field aligned heat conduction in the transition region and corona. The numerical methods have been described in detail by Gudiksen et al. (2011) and an earlier version of the code by Martínez-Sykora et al. (2008, 2009). In short, the code functions as follows.

The MHD equations are solved on a staggered grid, using sixth-order accurate spatial derivatives and fifth-order interpolation to shift the variables when needed at positions other than their defined grid locations.

Thermal conduction along magnetic field lines is included, where the heat conduction operator from the energy equation is solved using an implicit Crank–Nicholsen scheme and a multigrid method. The time stepping is done by a modified explicit third-order predictor–corrector procedure developed by Hyman (1979). High-order artificial diffusion is added in the form of viscosity and magnetic diffusivity to restrain numerical noise.

In the photosphere and lower chromosphere the radiative flux divergence is obtained by angle and wavelength integration of the transport equation, assuming isotropic opacities and emissivities. Following Nordlund (1982), the spectrum is divided into four opacity bins, and a transport equation is solved for each mean opacity, calculating the mean source function in each bin. These source functions contain an approximate coherent scattering term and an exact contribution from thermal emissivity. The resulting three-dimensional scattering problems are solved using a method developed by Skartlien (2000), which uses iterations based on a one-ray approximation in the angle integral for the mean intensity.

In the mid and upper chromosphere, Bifrost includes non-LTE radiative losses from tabulated hydrogen continua, hydrogen lines, and lines from singly ionized calcium as a function of temperature and column mass. These radiative losses depend on the computed non-LTE escape probability as a function of column mass (Carlsson & Leenaarts 2012).

For the transition region and corona, optically thin radiative losses are assumed. The optically thin radiative loss function is based on the coronal approximation and atomic data from DIPER (Judge & Meisner 1994).

2.2. Implementation of the Rate Equations

To compute the NEQ ionization of our model atom we need to solve the rate equations

$$\frac{\partial n_i}{\partial t} + \nabla \cdot (n_i \mathbf{u}) = \sum_{j \neq i}^{N_l} n_j P_{ji} - n_i \sum_{j \neq i}^{N_l} P_{ij}, \tag{1}$$

where n_i is the population density of ion level i, N_l is the total number of levels in the model atom, P_{ij} is the transition rate coefficient between level i and level j, and $\mathbf{u}$ is the macroscopic velocity. The levels can be either excitation levels or ionization levels, and will be described in more detail in Section 2.4. The left-hand side represents a continuity equation for each ion population density, while the right-hand side represents the sink and source terms due to transitions between the different levels included in the atom model. Because the advection timescale is much longer than the typical atomic timescales we use operator splitting to solve the equation in two steps: first, the continuity equation for each level in the model atom is stepped forward in time explicitly, after which this solution is used to solve the time-dependent SE equations implicitly, as follows: for each level i, the continuity equation

$$\frac{\partial n_i^o}{\partial t} = -\nabla \cdot (n_i^o \mathbf{u}) \tag{2}$$

is solved using a first-order upwind scheme, where n_i^o are the old values of n_i. We advect this in time:

$$n_i^* = \frac{\partial n_i^o}{\partial t} \Delta t + n_i^o \tag{3}$$

with timestep Δt. Using the advected n_i^* value and discretizing dn_i/dt we find the new population density, n_i. The next part of the operator splitting is then

$$\frac{n_i - n_i^*}{\Delta t} = \sum_{j \neq i}^{N_l} n_j P_{ji} - n_i \sum_{j \neq i}^{N_l} P_{ij}, \tag{4}$$

where we have used a first-order forward difference method to discretize dn_i/dt, using the same timestep Δt as used in the rest of the code. To solve for n_i we then have

$$n_i \left(1 - \Delta t \sum_{j \neq i}^{N_l} P_{ij} \right) - \Delta t \sum_{j \neq i}^{N_l} n_j P_{ji} = n_i^*. \tag{5}$$

The total rate coefficients P_{ij} entering the rate equations are composed of two parts, radiative rates and collisional rates. The collisional rates are dependent on electron density and temperature, while the radiative rates introduce global coupling through the radiation field. To be able to solve the rate equations we need to solve a radiative transfer equation for every frequency

and a rate equation for every level, at every grid point simultaneously, because of the global coupling. For N_ν number of frequencies, N_l number of rate equations, and N_d numbers of grid points, we have a solution vector with $N_\nu \times N_l \times N_d$ number of unknowns, which has to be solved at every timestep. The problem very quickly becomes unfeasible to solve even on the largest supercomputers. Fortunately, the transition region and corona are very nearly optically thin, simplifying this problem as radiation and matter largely decouple allowing a nearly local solution at every grid point. Scattering and absorption processes can be neglected when calculating transition rate probabilities, and we reduce our unknowns to N_l, making the problem much more tractable. Equation (5) turns into a set of linear equations $\mathbf{n} = \mathbf{A}^{-1}\mathbf{n}^*$, with an $N_l \times N_l$ rate matrix $\mathbf{A}$ with elements $A_{ii} = (1 + \Delta t \sum_{j \neq i} P_{ij})$ and $A_{ij} = -\Delta t P_{ji}$. We discuss the validity of the assumption of an optically thin atmosphere in Section 3.

The element population density, n_X, is dictated by the Asplund et al. (2009) solar abundance values as follows:

$$n_X = \frac{\rho}{m_{\rm av}} \frac{10^{A_X - 12}}{\sum_Y (10^{A_Y - 12})}, \tag{6}$$

where ρ is the mass density from the simulation, $m_{\rm av}$ is the average mass per particle, A_X is the corresponding abundance of element X, and the sum over Y is the sum over all the abundances in the Asplund et al. (2009) table.

Particle conservation is then given by

$$n_X = \sum_i n_i \tag{7}$$

and is enforced by replacing the rate equation which holds the largest ion concentration with this equation, thus keeping the total element population density of our model atom coupled to the overall mass density in the experiment. This results in a new $N_l \times N_l$ matrix comprised of $N_l - 1$ rate equations and the particle conservation equation.

2.3. Transition Rate Probabilities

The transition rate probabilities are found using the DIPER database. This database consists of a set of atomic data collected from various sources such as the NIST spectroscopy database (Ralchenko 2005), CHIANTI 5.2 (Landi et al. 2006), along with many others (see the DIPER reference guide for a complete list of sources). DIPER provides a collection of data from these tables for the specified atom of interest, resulting in a set of fitting parameters for the rate coefficients.

For every transition between level i and j, the rate coefficients are found through functions of temperature T, electron density n_e, and fitting coefficients provided by DIPER. The rate coefficients are fit to the forms presented below.

Collisional ionization rate coefficients are calculated according to Shull & van Steenberg (1982):

$$C_{\rm coll} = A_{\rm coll} T^{1/2} \cdot \left(1\text{–}0.1\frac{T}{T_{\rm coll}}\right) e^{-T_{\rm coll}/T}, \tag{8}$$

where $A_{\rm coll}$ and $T_{\rm coll}$ are coefficients from our atomic model produced by DIPER. This formula is created to follow the decrease in ionization cross section at high temperatures, where the gas temperature T is higher than the ionization temperature $T_{\rm coll}$. Dielectronic ionization $C_{\rm di}$ is calculated according to Arnaud & Rothenflug (1985):

$$C_{\rm di} = \frac{6.66 \times 10^{-7}}{(k_B T)^{3/2}} \sum_j \frac{\exp(-x_j)}{x_j} F(x_j) \tag{9}$$

with $x_j = I_j / k_B T$, (I_j, k_{BT} in eV), and

$$\begin{aligned} F(x_j) = {} & A_j[1 - x_j f_1(x_j)] \\ & + B_j[1 + x_j - x_j(2 + x_j) f_1(x_j)] \\ & + C_j f_1(x_j) + D_j x_j f_2(x_j) \end{aligned}$$

$$f_1(x) = e^x \int_1^\infty \frac{dt}{t} e^{-t}$$

$$f_2(x) = e^x \int_1^\infty \frac{dt}{t} e^{-t} \ln(t),$$

where A_j, B_j, C_j, and D_j are coefficients provided by DIPER. The formula is constructed to give a good fit to the shape of the cross sections, linking the measured and the calculated cross sections in the same isoelectronic sequence so that both low-charge ions and high-charge ions are included in the same fit.

Excitation auto-ionization contributions are calculated according to the isoelectronic sequences, i.e., ions with the same number of electrons. This method is identical to the one presented in Arnaud & Rothenflug (1985) and we have considered the lithium sequence, the sodium sequence, and the magnesium to sulfur sequences.

Radiative recombination rate coefficients follow Shull & van Steenberg (1982):

$$C_r = A_r (T/10^4\ {\rm K})^{-X_r}. \tag{10}$$

The coefficients A_r and X_r are provided by DIPER.

Dielectronic recombination rate coefficients follow Shull & van Steenberg (1982):

$$C_d = A_d T^{-3/2} \exp(-T_0/T)(1 + B_d \exp(-T_1/T)) \tag{11}$$

with the coefficients A_d, B_d, T_0, and T_1 provided by DIPER.

Three-body recombination is the inverse process of collisional ionization, where in the initial state we have two free electrons and an ion, and in the final state an ion with a lower ionization degree and a free electron. The contribution to the transition rate probability due to three-body recombination enters in several steps.

First the contribution is calculated as in Burgess & Chidichimo (1983), where the transition probability per unit time is given by $n_e q$, where

$$\begin{aligned} q = {} & 2.3 \times 2.1725 \times 10^{-8} \sum_l \zeta_l (I_H/I_l)^{3/2} \\ & \times (I_l/k_B T)^{1/2} E_1(I_l/k_B T) w. \end{aligned} \tag{12}$$

With the summation over all shells l of the initial ion, ζ_l is the effective number of electrons in l, I_l is the ionization energy, I_H is the Rydberg energy, $E_1(x)$ is the exponential integral, and w is the Wannier factor, representing the deviation from a linear behavior near the ionization threshold, given by

$$w = [\ln(1 + k_B T/I_l)]^{\beta(1 + k_B T/I_l)}, \tag{13}$$

where $\beta = (1/4)[(100Z + 91)/(4Z + 3)]^{1/2} - 5$ represents the dependency on the charge number Z. w is only significant for ions of low charge and very small values of $k_B T/I_l$.

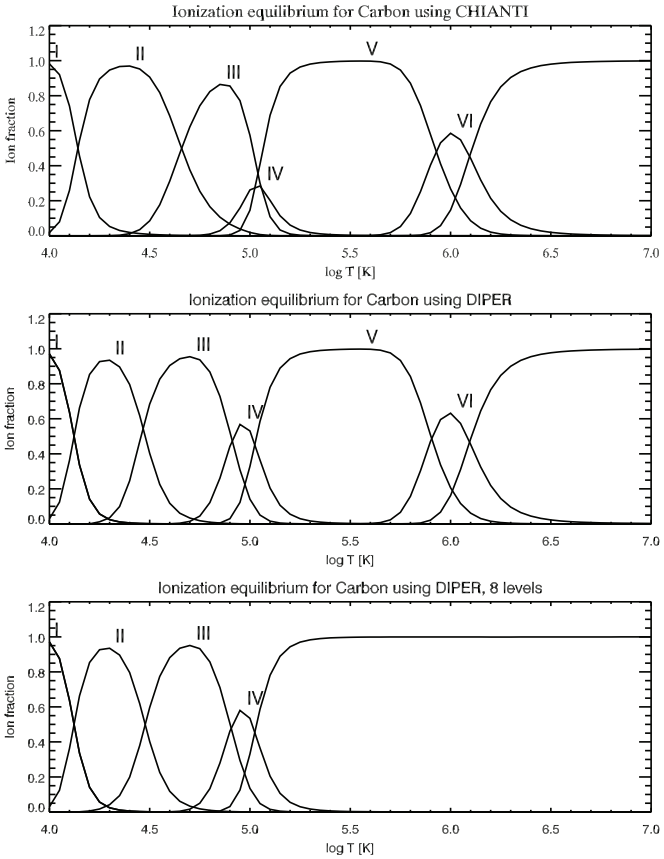

Figure 1. Top panel shows the carbon ion fractions when assuming ionization equilibrium as provided by CHIANTI, the middle panel the DIPER ion fractions when including 297 levels in the model atom, and the bottom panel the ion fractions from the atomic model created using the DIPER tools, now reduced to containing only eight levels.

Bound-Bound transitions with thermalized electrons contribute to the collisional rate probability through

$$C_{ji} = 8.63 \times 10^{-6} \frac{\Upsilon_{ji}(T)}{g_j} T^{-1/2} n_e, \qquad (14)$$

where $\Upsilon_{ji}(T)$ is the Maxwellian-averaged collisional strength at electron temperature T, and g_j is the statistical weight of level j. The collisional strengths are calculated through spline fitting from given bound–bound collisional data in the DIPER atomic model. This is the second contribution to the transition rate probability due to three-body recombination.

It is also possible to include fixed radiative rates to the transition probabilities, and in that way include an ad hoc term to mimic the effects of a radiation field irradiating the modeled atmosphere.

2.4. The Atomic Model

As an example we look closer at the carbon atom, and especially the ion C IV which one-dimensional models show to be especially sensitive to NEQ effects. The ion fractions for ionization equilibrium are plotted in Figure 1. CHIANTI (Dere et al. 2009) gives the ion fraction as a function of base 10 logarithmic temperature, from 4 to 8. The top panel shows the ion fractions from $\log_{10} T$ [K] = 4 to $\log_{10} T$ [K] = 7. In the middle panel the equivalent results from the full DIPER carbon data are presented; this includes all 297 levels stored in DIPER. In order to carry out this calculation one needs to specify the electron density as well: here, we have used $n_e = 10^{15}/T$ as the electron density. Working with so many levels is prohibited when solving the full time-dependent MHD problem, but given the tools of DIPER, it is possible to construct an appropriate smaller atomic model, consisting of only eight levels. This model is presented in the bottom panel of Figure 1. We find differences between the DIPER and CHIANTI ionization equilibrium ion fractions for C II, C III, and C IV. The ion fraction for C II is broader in temperature with CHIANTI than with DIPER, while C III is narrower and has a lower peak value. The C IV ion fraction is significantly lower in CHIANTI than in DIPER. At the same time, the C IV peak originates at temperature slightly above $\log_{10} T$ [K] = 5, whereas in DIPER it originates at temperatures slightly below $\log_{10} T$ [K] = 5.

We have chosen not to include C VI and C VII in our model, since these ions do not have any effect on the C IV ion population density at the modeled temperature.

The important C IV doublet, 154.82 nm and 155.08 nm, has been analyzed. To shorten the computational time, we represent the doublet using a single constructed line, 154.9 nm, in the model. This is done by using the statistical weights g_i for the two upper levels, constructing a weighted mean spontaneous decay rate and level energy. Since the lower level of the 154.82 nm spectral line and the 155.08 nm spectral line is the same, the upward collisional transition rate for the newly created line, 154.9 nm, is the sum of the 154.82 nm and 155.08 nm collisional transition rates.

The carbon model is now comprised of eight levels, where C I and C II are represented by one level each, their ground state. C III is represented by three levels, its ground state and two excited states. C IV is represented by its ground state and one excited state, and C V is represented by one level, its ground state.

3. VALIDATION

The implemented solver for the ionization levels has been tested and validated through a number of validation tests, some of which are presented here.

3.1. The Advection Test

The advection test serves as a validation to the solution of the rate equations. The study consists of testing the implemented method for several different advection velocities, while keeping the rest of the variables constant, isolating the effect of advection on the rate equations, and the consistency with an SE solution. The test is a one-dimensional hydrodynamic run with a large jump in temperature, akin to the solar transition region, and a constant velocity that advects gas across the jump in temperature. We perform tests by varying the direction and speed of the plasma. We require that the pressure be constant throughout the simulation, forcing the mass density to vary with changes in the temperature. A constant velocity is imposed which we vary from run to run.

To maintain a constant temperature and mass density with time we need to ensure that the time derivatives are zero in Bifrost. We accomplish this by adding a term to the time derivative for mass density, momentum, and internal energy of the following form:

$$\frac{\partial \rho}{\partial t} = \frac{\partial \rho}{\partial t} + \frac{\rho - \rho_0}{\Delta t} \tag{15}$$

$$\frac{\partial \rho \boldsymbol{u}}{\partial t} = \frac{\partial \rho \boldsymbol{u}}{\partial t} + \frac{\rho \boldsymbol{u} - \rho_0 \boldsymbol{u}_0}{\Delta t} \tag{16}$$

$$\frac{\partial e}{\partial t} = \frac{\partial e}{\partial t} + \frac{e - e_0}{\Delta t}, \tag{17}$$

where the subscript 0 is the initial value that varies in space. This is equivalent to setting the time derivatives of density, momentum, and internal energy to zero. In this process we break the conservation of momentum and internal energy. The model setup is consequently nonphysical and is created only for the purpose of isolating the advection term in the rate equations. In order to keep the mass density, momentum, and internal energy constant, Δt is chosen to be much smaller than any other typical timescale of the simulation. There is no gravity, radiation, convection, heating, or magnetic fields included in this model test.

The simulation setup is a one-dimensional model of 150 grid points with a temperature and mass density profile as presented in the topmost panels in Figure 2. The temperature in the model goes from 7400 K to 1.2 MK through a temperature gradient with a peak value of 2.1 K m^{-1} at 5.3 Mm. We follow the ideal gas law, where the internal energy $e = (1/\gamma - 1)(P/\rho)$. The pressure is kept constant throughout the atmosphere, as well as in time, at 10 Pa, resulting in a mass density of 4.0×10^{11} kg m^{-3} at $\log_{10} T\,[\mathrm{K}] = 5.0$.

We present the results of the C IV ion population density through 240 s of solar time for advection velocities ranging from 1 m s^{-1} to 100 km s^{-1} in Figure 2, and -1 m s^{-1} to -100 km s^{-1} in Figure 3. The C IV ion fractions are plotted on the four bottom panels of Figure 2, with the mass density and temperature plotted in the top panels. In all six panels of Figure 2, a new profile of the mass density, temperature, and C IV ion fraction is plotted, with a color given by the color bar at the bottom of the figure. The two top panels show that during all the runs, the temperature and mass density profiles are constant in time as forced by the artificial terms included in the model.

Joselyn et al. (1979a) presented calculations of flows and ionization equilibria for three different atmospheres: quiet Sun, coronal hole, and network, in which they find that C IV should be out of equilibrium for 1, 5, 10, and 20 km s^{-1} for all three atmospheric models. We chose to test our model with the 1, 10, and 100 km s^{-1} flow speeds and furthermore add a test with a very low flow speed of 1 m s^{-1}. A velocity of 1 m s^{-1} or -1 m s^{-1} is so low that it should not be able to advect ions to regions of significantly higher or lower temperature before they have time to readjust to the new local values of the temperature and mass density and should therefore reproduce the SE solution of the code.

The four bottom panels of Figure 2 show a pronounced peak in the ion fraction of C IV. For $u_z = 1$ m s^{-1} the C IV ion fraction stays the same throughout the run. At $u_z = 1$ km s^{-1} the ion fraction peak is shifted to higher temperature regions. With $u_z = 10$ km s^{-1} the C IV population is significantly higher at all temperatures above the equilibration temperature at $\log_{10} T\,[\mathrm{K}] = 5$, and the peak ion fraction moves to higher temperatures with time, creating a tail at corona temperatures. At $u_z = 100$ km s^{-1} the C IV ion fraction reaches a maximum only after a few seconds, and the ionization stage of C IV is frozen in.

The explanation can be found by calculating the ionization times for C III and the recombination times to C III. Figure 4 shows ionization and recombination times involving C IV, as functions of temperature. In this case the mass density is $\rho = P/k_B T$, with constant pressure, $P = 10$ Pa, creating a direct correspondence between temperature and mass density. The plot is made using DIPER and carbon data for an SE solution. For temperatures below $\log(T)\,[\mathrm{K}] = 4.9$, the recombination time is lower than the ionization time, keeping the C IV ion fraction very low at these temperatures, as seen in the $u = 1$ m s^{-1} plot in Figure 2. Above $\log_{10} T\,[\mathrm{K}] = 4.9$, the opposite is true and the C IV ion fraction increases sharply with temperature until the ionization times from C IV to C V become comparable to the recombination times from C V to C IV at temperatures above $\log_{10}\,[\mathrm{K}] = 5.2$, where the C IV population density then will find an equilibrium ratio with the C V population density for the region of constant temperature at a height above 5.5 Mm.

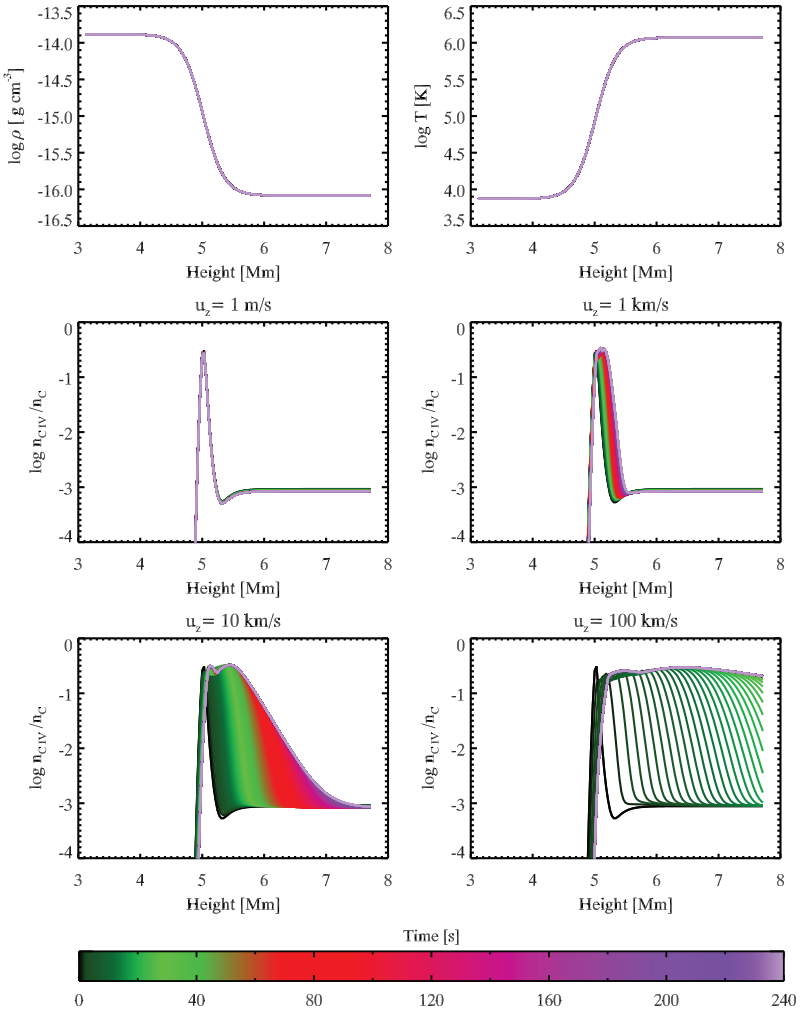

Figure 2. Variables from a 240 s one-dimensional run, where the values of the variables are displayed for every second, represented by a color starting with black at time 0 s and ending at pink as shown in the color bar. Mass density and temperature are shown in the top panels. The C IV population densities are plotted for four different velocities in the four bottom panels. A velocity of 1 m s^{-1}, shown in the left middle panel, has an SE solution over time. For a velocity of 1 km s^{-1}, middle right panel, NEQ changes to the population densities are seen. At velocities of 10 km s^{-1}, C IV populations stretch to higher layers of the atmosphere, forming a tail toward the corona that increases with time. At velocities of 100 km s^{-1}, bottom right panel, the C IV population is completely out of equilibrium, reaching a steady state only 26 s into the run.

To see a significant departure from SE, the advection velocity has to be high enough to bring an ion population to a region where the equilibrium population is significantly different within the ionization and recombination times. The ionization time from C III to C IV is less than 1 s at the equilibration temperature of C IV as plotted in Figure 4. Within that time, at a velocity of 1 m s^{-1}, the distance traveled would be 1 m, which would at most change the temperature by 2.1 K at the peak temperature gradient; this has hardly any effect on the equilibrium population densities of C III and C IV. For significantly higher velocities, the C III ions are able to travel into a region where the local temperature is significantly different, and so bring the ion populations out of equilibrium. That is clearly reproduced in Figure 2, where the plot for 1 m s^{-1} shows no development with time and the population is in SE. For higher velocities we can see that the population of C IV is advected to greater heights, to a degree where the C IV population density is higher than the equilibrium population density. It is also instructive to see that the populations return to SE at a height corresponding to the advection velocity times the largest recombination and ionization times. For $u = 100$ km s^{-1} the velocity is so high that we hardly see any decrease in the population density of C IV with distance from the temperature jump, and the ionization state is frozen, but that is only an effect of the very large velocity. For

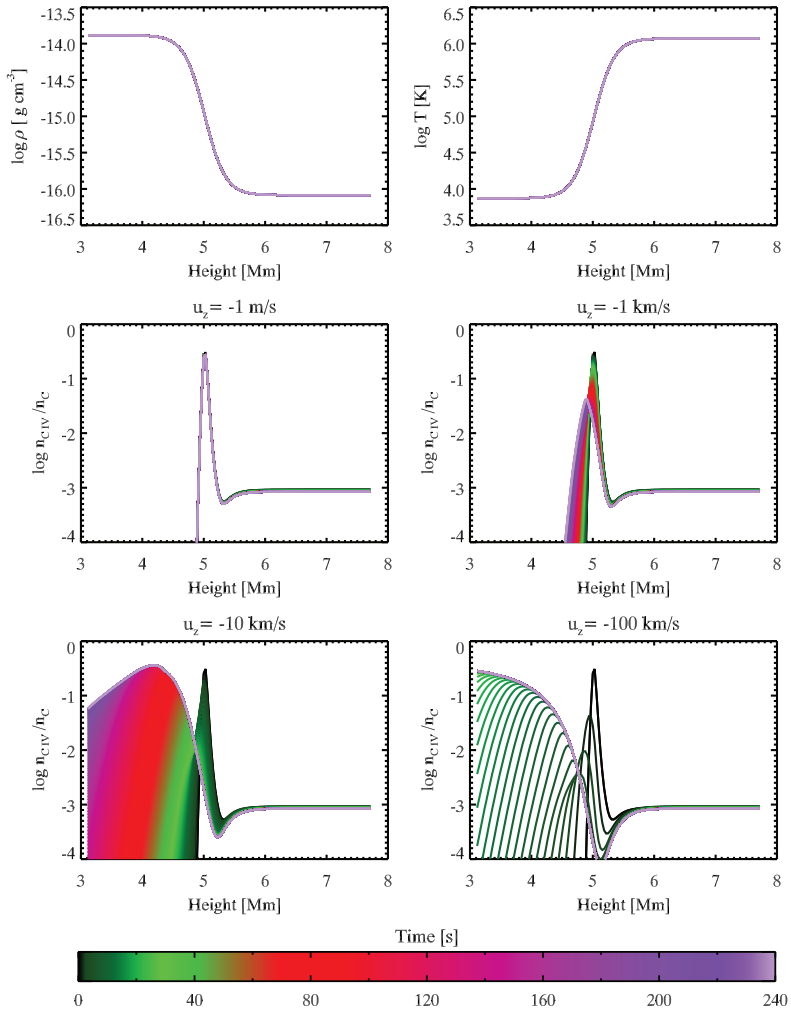

Figure 3. Same as Figure 2, but with negative velocities. The C IV ion fractions are plotted on the four bottom panels. With a velocity of -1 m s^{-1}, the results show an SE solution over time. For a velocity of -1 km s^{-1} we start observing NEQ changes to the ion fractions, where the gas is moved to lower temperature regions. Recombination of C V is the main reason for the C IV ion fraction to increase at low temperatures, as is evident in the -1 km s^{-1}, -10 km s^{-1}, and -100 km s^{-1} panels.

the 100 km s^{-1} simulation, the initial peak in the C IV population is also shifted to greater heights due to the advection of C III ions from the cold region at low heights.

The bottom four panels of Figure 3 show the ion fraction for negative velocities; here, hot material is advected to colder regions of the atmosphere. As we decrease the velocity, the peak of C IV ion fractions decreases toward lower temperature regions, as seen in the -1 km s^{-1} panel of Figure 3. This is because the temperature is too low to ionize C III to C IV, but just as the peak reaches some critical temperature, the ionization fraction of C IV starts to increase toward lower temperatures. This is because C V ions are moved to lower temperature regions as well, and start to recombine to C IV. With higher downward advection velocities, an increasing number of C V reach lower temperature regions, and the C IV ion fraction increases as observed in the two bottom panels of Figure 3. The process of ionizing C III to C IV is the main contributor to the C IV population density when we have high upward velocities, as presented in Figure 2, while the recombination process from C V to C IV is the main contributor when high downward velocities are present, as shown in Figure 3.

In making such a simple model, the effect of advection is clear. To disturb the ionization equilibrium, the advection velocities need not be large to have a large effect. The results of Joselyn et al. (1979a) are reproduced with this simple one-dimensional model.

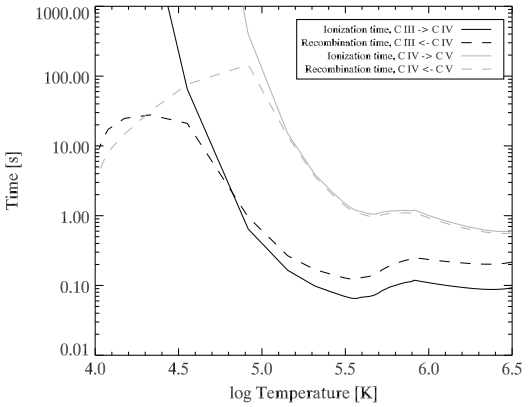

Figure 4. Ionization and recombination times involving C IV. According to these plots, C III would easily ionize to C IV at high temperatures, while it is more difficult to recombine C IV to C III with increasing temperature.

3.2. The Optically Thin Approximation

The solver for the ionization assumes that there is no contribution from radiation in the source and sink terms in Equation (1). This assumption is generally named the optically thin approximation. That assumption is not true for all lines at all depths. The optically thin approximation is relatively easy to test by calculating the optical depth for the line in question for a given solar atmosphere model. The assumption is only valid as long as the optical depth is small. The optical depth τ_ν of a ray of light traveling a distance z is

$$\tau_\nu = \int_0^z \alpha_\nu dz, \tag{18}$$

where α_ν is the monochromatic line extinction coefficient. The line extinction coefficient per particle, $\sigma_\nu = \alpha_\nu / n_l$, where n_l is the population density of ions with electrons in the lower energy state of the two states involved in the spectral line, can be expressed as

$$\sigma_\nu = \frac{\pi e^2}{m_e c} f_{lu} \varphi(\nu - \nu_0), \tag{19}$$

where e is the electron charge, m_e is the electron mass, f_{lu} is the oscillator strength between the upper and lower levels, and $\varphi(\nu - \nu_0)$ is the emission probability distribution around the line center due to line broadening.

The line-center amplitude is $\varphi(\nu = \nu_0) = 1/(\sqrt{\pi}\Delta\nu_D)$ for purely Doppler broadening, where the Doppler width is $\Delta\nu_D = \nu/c\sqrt{2k_B T/m}$, with m being the mass of the emitting particle. The optical depth becomes

$$\tau_\nu = \frac{\pi e^2}{m_e c} f_{lu} \frac{c}{\nu} \sqrt{\frac{m}{2\pi k_B}} \int_0^z \frac{n_l}{\sqrt{T}} dz. \tag{20}$$

The level populations n_l are given by calculating the NEQ populations or by other population density calculations assuming SE. Here we perform both SE and NEQ calculations directly from the code, and also perform calculations of the optical depth using DIPER and CHIANTI assuming SE, in addition to SE calculations with a Fal–C model atmosphere (Fontenla et al. 1993). In this test, a 256 × 256 grid point two-dimensional snapshot from one of our simulation runs designed to be fairly close to solar parameters is used, where we calculate the ion fractions and emissivities at each grid point. For the optical depth, we integrate over each vertical column in the two-dimensional snapshot. To do the DIPER and CHIANTI calculations, temperatures and electron densities at each grid point from the same snapshot are used. The simulation run is presented in more detail in Section 3.3, where the snapshot used here corresponds to the data at 45.0 s in Figures 7 and 9. The temperature, mass density, and vertical velocity of the snapshot are displayed as probability distribution functions in Figure 5, as functions of height. The photosphere of the Sun is roughly at 0 Mm, and the chromosphere continues up to 2 Mm. The transition region is displayed around 2 Mm in the left panel, going from $\log_{10} T$ [K] ≈ 4 to $\log_{10} T$ [K] ≈ 6 in only a few kilometers. The corona then continues up to 9 Mm. The mass density falls rapidly from 10^{-4} kg m^{-3} at the surface to ≈10^{-11} kg m^{-3} at the beginning of the corona, and then evens out at coronal heights. The velocity distribution is displayed on the right panel of Figure 5, where we see a high probability density of high velocities below 3 Mm.

The test has been performed for all the lines we report on here, C IV 154.9 nm and Fe XII 19.51 nm, which we investigate in Section 3.3. Here we show an example of the results for the test of the 154.9 nm C IV line. The ion fractions from DIPER, CHIANTI, SE Bifrost, and the NEQ Bifrost are plotted in the middle panel of Figure 6. The resulting SE ion fractions for DIPER and SE Bifrost are identical, with a peak value of 0.57 at $\log_{10} T$ [K] = 4.97. The CHIANTI ion fractions are different due to the difference in ion fractions in ionization equilibrium, as presented in Figure 1, where we see that the CHIANTI data give a different distribution of the ions in the carbon model compared to the DIPER data. In our calculation with CHIANTI we get a C IV ion fraction peak of 0.36 at $\log_{10} T$ [K] = 5.01. The NEQ ion fractions (NEQ Bifrost) reach a maximum at $\log_{10} T$ [K] = 5.13 with a peak value of 0.68, but there is a large spread, and when all grid points are considered, shows a majority that peak at the low temperature of $\log_{10} T$ [K] = 4.13, with a peak value equal to 0.35, followed by a slow decrease toward higher temperatures.

In addition to CHIANTI and DIPER, we test the semi-empirical model Fal–C. By using electron densities and temperatures from Fal–C, the carbon model we have created with DIPER, and the DIPER SE solver, we can retrieve the corresponding Fal–C carbon populations and emissivities. The ion fraction from the Fal–C model fit well with the SE results from DIPER and Bifrost as presented in the middle panel of Figure 6.

The equivalent optical depths are plotted on the bottom panel in the form of a histogram. Since the Fal–C atmosphere is a one-dimensional atmosphere we get only one data point, plotted as the red dot in the bottom panel of Figure 6. For the NEQ C IV the optical depth is higher than the other three SE C IV values. Nonetheless, the optical depths for all four examples are below 1 for our C IV calculation. We can thus conclude that the assumption of optically thin conditions holds for C IV.

It is instructive to calculate where the emission in this line primarily comes from. Since we solve the rate equations we have the level populations of both the upper and lower levels of the C IV 154.9 nm transition, making it possible to calculate the emissivity of the line in the simple form:

$$\epsilon_\nu = \frac{h\nu}{4\pi} n_u A_{ul}. \tag{21}$$

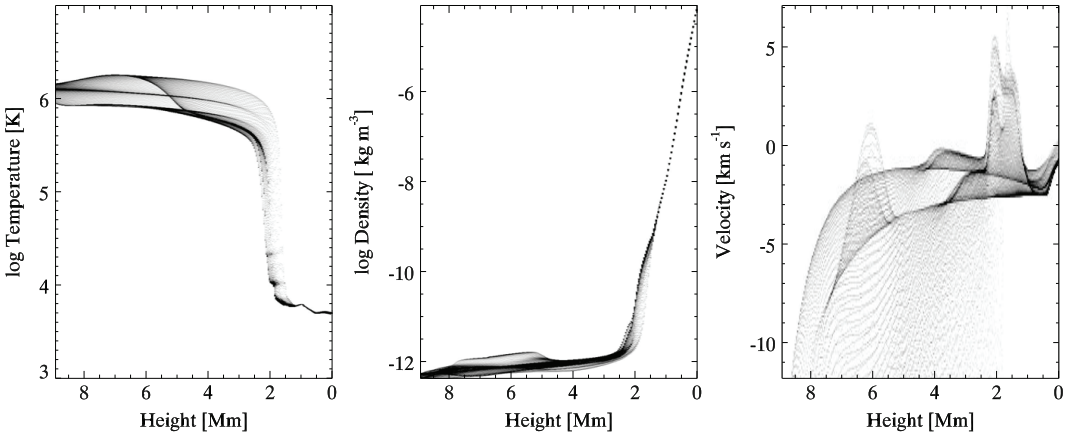

Figure 5. Probability density functions for the temperature, mass density, and velocity in the 45 s snapshot, as a function of height.

This method can be used to calculate the emissivities for Bifrost (SE and NEQ), DIPER, and by using the DIPER SE solver, Fal–C emissivities. These are plotted in the upper panel of Figure 6.

The DIPER emissivities (green) have slightly lower values than those found in our Bifrost formulation. This is due to the way the element abundance is calculated in DIPER:

$$n_H = \frac{0.8 n_e}{n_H^n / n_H^i}$$
$$n_X = n_H (10^{A_X - 12.}),$$

where n_H is the hydrogen population density, n_e is the electron density, n_H^n / n_H^i is the ratio of hydrogen neutral density to hydrogen ion density, n_X is the element density, and A_X is the element abundance value (here carbon). This is different from the way the element population densities are calculated in Bifrost (Equation (6)). When modifying the routines of DIPER to calculate the element population density the same way as in Equation (6), the results are identical to what we get in our SE Bifrost calculation, as plotted in yellow in the panels of Figure 6, where the SE Bifrost emissivities in black overlap with the modified DIPER (DIPER mod) values. The optical depth and ion fractions from the modified DIPER results are also plotted in Figure 6, showing identical results when compared with the SE Bifrost solution.

The emissivity is larger with the Fal–C data compared to the other models here, but is still within the distribution of SE points from our SE Bifrost solution and DIPER. The Fal–C model was created to fit as many line strengths as possible through the whole solar atmosphere. Based on the SE data produced by Bifrost, Figure 6 shows that our model of the solar atmosphere is similar to the Fal–C model when observing it in the C IV line, especially when used to calculate the SE ion fractions. But it is also clear that the emission does not only come from locations with temperatures which one would expect from an SE model, but also from regions of much lower temperature.

The emissivity can also be expressed as a function of the contribution function $G(T, \nu, n_e)$, $\epsilon_\nu = A_x n_e n_H G(T, \nu, n_e)$. The contribution function is provided by CHIANTI, and we use this expression to get the CHIANTI emissivity, which we have plotted in purple in the upper panel of Figure 6. The emissivities from CHIANTI are lower than the other five examples; this is due to the difference between the ionization fractions of the atomic models in CHIANTI and DIPER as presented in Figure 1, where the C IV fraction is lower for CHIANTI than for DIPER.

The emissivity of NEQ C IV arises from a broader temperature region, spanning from $\log_{10} T\,[\mathrm{K}] = 4$ to $\log_{10} T\,[\mathrm{K}] = 6$, than the SE results, and is on average significantly lower than the SE emissivity.

This test has shown that our method of solving the rate equations is consistent with both DIPER and CHIANTI in SE. The C IV population is located at a wider temperature region than assumed in SE, and is therefore also emitting from a broader region of the atmosphere. Nonetheless the optically thin approximation holds for the C IV 154.9 nm spectral line.

3.3. The Heating Test

Let us now consider the case of rapid heating of the coronal plasma in a magnetized atmosphere and study the reaction of the C IV and Fe XII population density to the heating event. The simulation setup is a two-dimensional model containing a photosphere, a chromosphere, and a corona with a horizontal extent of 16.5 Mm and a vertical extent of 9 Mm. The model presented is defined on a uniform grid of 256×256 grid points, with a grid spacing $\Delta x = 62.5$ km horizontally and $\Delta z = 35$ km vertically.

The model has solar gravity and a dipolar magnetic field. The magnetic field is formed by a potential extrapolation of a positive and a negative magnetic polarity of ± 1000 G field strength placed at the bottom boundary, each spanning 1 Mm and centered at $x = 2.5$ Mm and $x = 13.5$ Mm, respectively. Radiative losses are included through the optically thin and chromospheric approximations, but the full optically thick radiative transfer module is turned off. Thermal conduction is included and the corona is kept heated by maintaining the temperature at the upper boundary at 1.1 MK.

During the first 10 seconds of the model run we deposit 0.5 J m^{-3} over a region spanning 200×200 km^2, at location $x = 9$ Mm, $z = 6.3$ Mm. If we assume a depth of 200 km, this is sufficient energy to simulate a small nano-flare of 4×10^{16} J, comparable to Parker's original nano-flare of 6×10^{17} J (Parker 1988). During this period the temperature goes from 1.26 MK

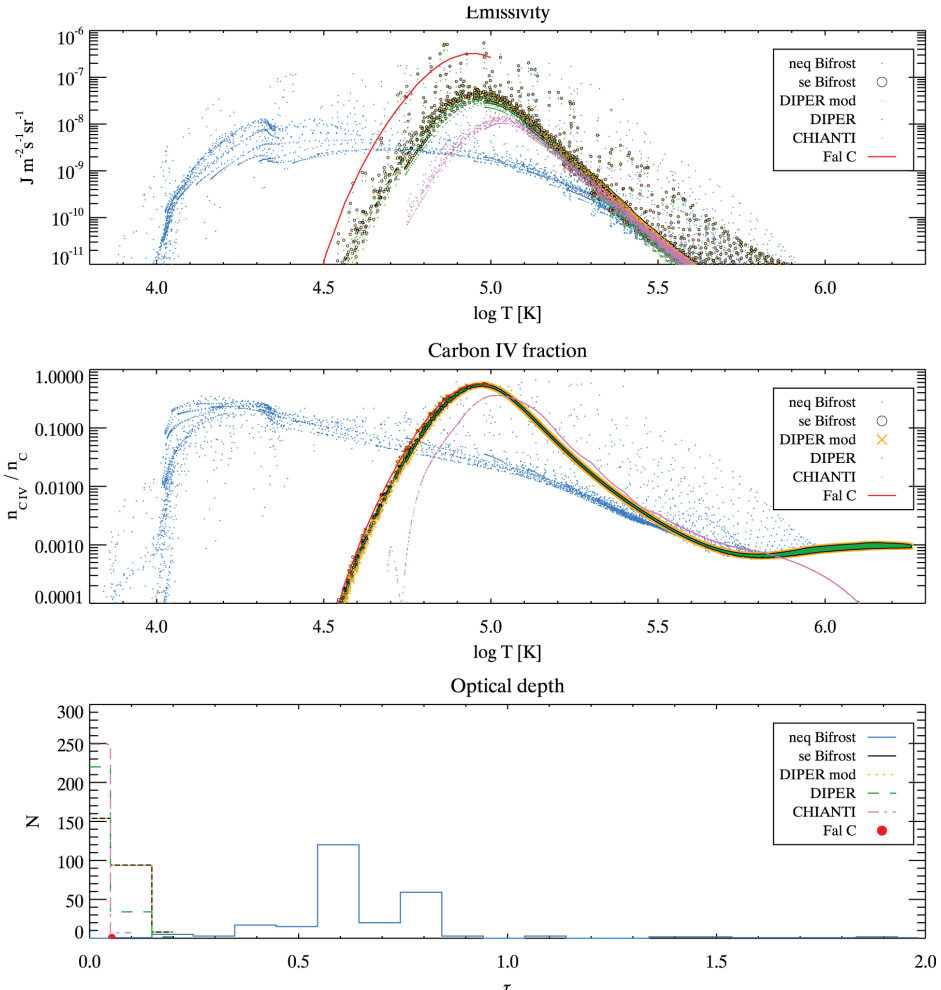

Figure 6. Comparison of Models. Data from a two-dimensional snapshot, 45 s into the run. The top panel shows the emissivity in logarithmic scale for Bifrost (SE and NEQ), Fal–C, DIPER, and CHIANTI, where DIPER mod is the results from the DIPER calculations when modified to take into account the carbon population density as presented in Equation (6). The middle panel shows the ion fractions and the bottom panel shows a histogram of the optical depths for these six cases.

to 3.98 MK. After the heat deposition, we allow the atmosphere to cool, where the simulation uses 80 s to cool to the original temperature.

Figure 7 shows the effect the nano-flare has on the electron density, temperature, and vertical velocity at times 0.1 s, 1.5 s, 7.8 s, 29.0 s, 45.0 s, and 71.0 s. The electron density and temperature have a direct effect on the ion population densities, and will affect the population densities in SE and NEQ, while the velocity will influence the NEQ population densities through advection. The development of the ion population densities of C IV and Fe XII is presented in Figure 9 for both NEQ and SE.

We have chosen to concentrate on C IV and Fe XII in this study because they are ions with important emission lines used for studying the transition region and lower corona. C IV has previously been studied closely by many instruments, among them the UV spectrograph Solar Ultraviolet Measurement of Emitted Radiation on board the *Solar and Heliospheric Observatory* (Brekke et al. 1996), mainly because this spectral line is representative for many transition region lines. The Fe XII ion is, among others, observed with EIS, on board the *Hinode* satellite (Culhane et al. 2007), and AIA. These ions are also interesting to study in this nano-flare experiment because we originally have a high Fe XII population density in the region where the energy is deposited, while C IV is a transition region ion, so the population density of this ion is low. Other differences between these ions are the ionization and recombination times of the ions, where C IV has an ionization time of less than 1 s at 1 MK; Fe XII has an ionization time of 100 s at 1 MK. The ions should consequently behave very differently, and the populations should be dominated by different terms in their rate equations. The ionization time of C III is about 100 s in the transition region but decreases to 0.1 s in the corona, as displayed in Figure 4. At the site of energy deposition the original temperature is about 1 MK, so C III has a very low

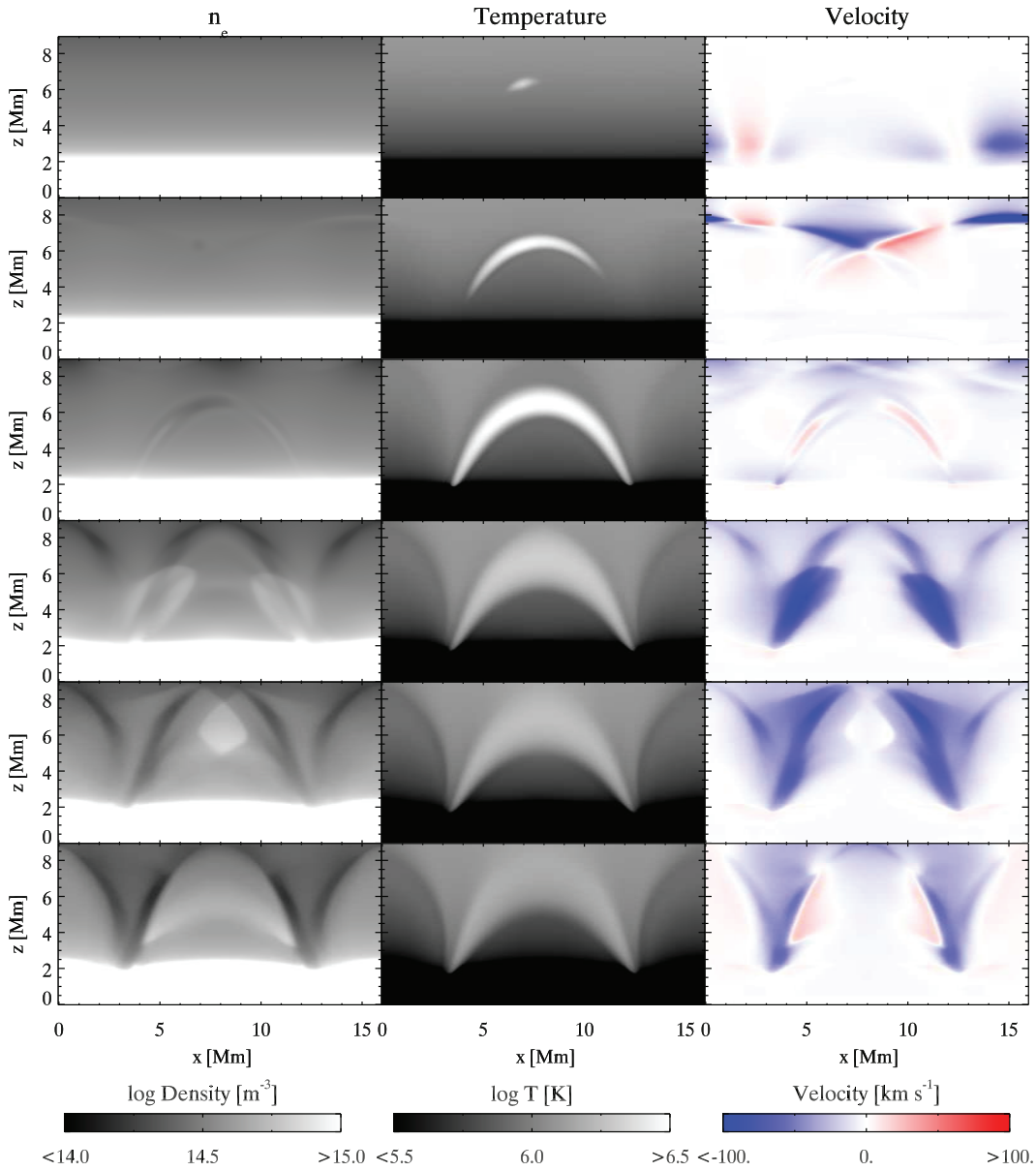

Figure 7. Time evolution of a two-dimensional model which is heated for 1 s at position $x = 9$ Mm, $z = 6.3$ Mm with 0.50 J m^{-3} over a region spanning 200 × 200 km^2. The panels show, from left to right, the electron density, temperature, and vertical velocity. Time increases downward, showing snapshots at times 0.1 s, 1.5 s, 7.8 s, 29.0 s, 45.0 s, and 71.0 s.

ionization time, and we can therefore expect the NEQ C IV population density in the corona to not change significantly, i.e., remain in SE.

After the initial heat input from the simulated nano-flare, the magnetic-field-directed thermal conduction raises the temperature in a loop-like structure dictated by the topology of the magnetic field. The temperature increase affects the pressure in the gas, and consequently we observe changes in the electron density as presented on the left column of panels in Figure 7. As the temperature increase reaches the dense magnetic foot points in the chromosphere, a large amount of gas evaporates from the chromosphere, creating a plume of gas that travels back up along the magnetic field lines. As the evaporation emerges, we observe a downflow as well, as presented in Figure 7. The

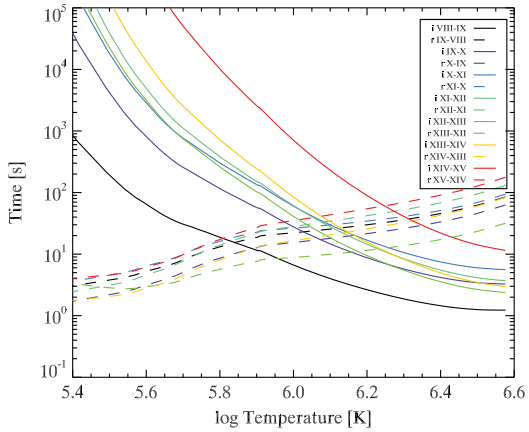

Figure 8. Ionization and recombination times of the ions in our Fe atomic model. In the caption, *i* represents ionization time and *r* recombination time.

evaporation velocity reaches a maximum speed of 108 km s^{-1} 14.4 s into the simulation time, while the downflow velocity reaches a maximum speed of 28 km s^{-1}. The emerging evaporation velocities change the pressure and mass density in the medium, and consequently the electron density, as can be seen on the left panels of Figure 7. At $t = 29.0$ s the plume has traveled to larger heights. The increase of velocity and consequently pressure forms pressure fronts in the electron density.

The fronts move higher, and meet at approximately 6 Mm, at the loop apex, mixing the material from both fronts, as can be seen in the 45 s panels in Figure 7. As the fronts meet, a shock is created, increasing the temperature as well. The fronts continue to mix, and eventually fall, as is observed in the velocity panels of Figure 7, with a maximum speed of 28 km s^{-1}.

3.3.1. Carbon IV

The SE C IV reaction to the heating is displayed in the second column of Figure 9. In SE, the reaction to the temperature increase on C IV is instantaneous, and we get a higher abundance of C IV ions in the region where heating is going on, as shown in the 0.1 s panel on the second column of Figure 9. The increase of electron density due to pressure change adds to the changes in the C IV population, as shown in the 7.8 s panel of Figure 9. As the emerging velocities from chromospheric evaporation change the pressure in the medium, and consequently the electron density, a plume of C IV travels back up along the magnetic field lines.

As the evaporation fronts meet, C IV ions from both fronts mix, as seen in the 45.0 s panel of Figure 9, increasing the C IV population density at the loop apex. The increase in electron density due to the pressure changes and the increase of temperature from the shock contribute to the increase of C IV. As the plasma falls back (as observed in the velocity panels of Figure 7), C IV ions react to the change in electron density and temperature, and follow, filling the loop, which can be seen in the lower left panel of Figure 9.

The NEQ C IV reaction to the heating is displayed on the first column of Figure 9. Except for a time delay at the beginning of the heat deposition in the reaction of the NEQ C IV population densities, NEQ C IV behaves similarly to the SE C IV at coronal heights, but in addition to the pressure fronts shown in SE at 29.0 s, C III is pushed to higher temperature regions in NEQ, and more C IV is created, adding material to forming ionization fronts in the NEQ case. The C IV population density at these coronal heights is low, and the effect of advection is low.

The clearest NEQ effect on C IV is the increase of C IV in the transition region around $z \approx 2$ Mm, evident as the black ribbon on the left panels of Figure 10. We observe an expansion of the region with time. To study this region better, we take a cutout of the right loop foot point, looking closer at four snapshots of the time evolution in this region. Velocity maps at times 6.0 s, 10.0 s, 30.0 s, and 90.0s, with contours of the temperature at 100 kK, 200 kK, and 500 kK in green, and the C IV ion fraction at 0.01 in red for SE, and in black for NEQ are plotted in Figure 11. At time $t = 6.0$ s the evaporation has just started, where we observe the evaporation velocity in blue just above $z = 2$ Mm; at the same time, about 50 km below, a downflow velocity emerges as well, in red here. The contours of the 0.01 NEQ C IV ion fraction are below 2.0 Mm at the loop foot point, enveloping the area with the downflow velocity. It is therefore the downflow velocity that influences the NEQ C IV ion fraction, pushing C IV ions down to lower regions of the atmosphere. The downflow velocity is between 10 km s^{-1} and 28 km s^{-1}, enough to get the C IV ions out of ionization equilibrium. The evaporation velocity influences regions of low C IV fractions; it therefore takes some time before we notice the influence of the evaporation velocity on the C IV ion fraction. As more C III ions are advected to higher temperature regions, more C III ions ionize to C IV, and we observe an increase of C IV along the loop, as shown by the black contour lines in Figure 11.

The downflow velocities are high enough to advect the C IV ions out of ionization equilibrium, and are also located at regions of the highest C IV ion fractions. Consequently a significant amount of C IV is pushed to lower regions, resulting in a downward spread in C IV, as shown in the 90.0 s snapshot of Figure 11. The 0.01 ion fraction contours of the NEQ C IV originally span a region of 180 km, and after 90.0 s span a region of 500 km, a result of high advection velocities in the region.

No matter how the population density of a particular ion behaves, what we would observe from the Sun is emission of spectral lines for the particular ions of interest. It is therefore of interest to see the effect of NEQ on the emissivity of spectral lines of these ions. The emissivity of the C IV 154.9 nm spectral line is displayed in Figure 10. The only visible change in emissivity is at transition region heights, where the emissivity emerges from a wider range in height, compared to the SE case, as reflected from the population densities in Figure 9.

3.3.2. Iron XII

The temperature at the nano-flare site becomes so high that in SE, Fe XII ionizes to Fe XIII instantaneously, which is shown as the low population density spot in the 0.1 s panel of Figure 9; the high population density ring is the remaining Fe XI ionizing to Fe XII. As the temperature increases along the loop at 1.5 s and 7.8 s, so does the feature in SE Fe XII. The dark low population density feature follows the loop structure, accompanied by the high population density envelope.

When the high temperature reaches the loop foot points, we see the highest population density of Fe XII at the loop foot points. Now, chromospheric material evaporates up along the loop, increasing the Fe XII population as the rise of pressure increases the electron density, resulting in evaporation fronts in the Fe XII population density, as shown in the 29.0 s panel.

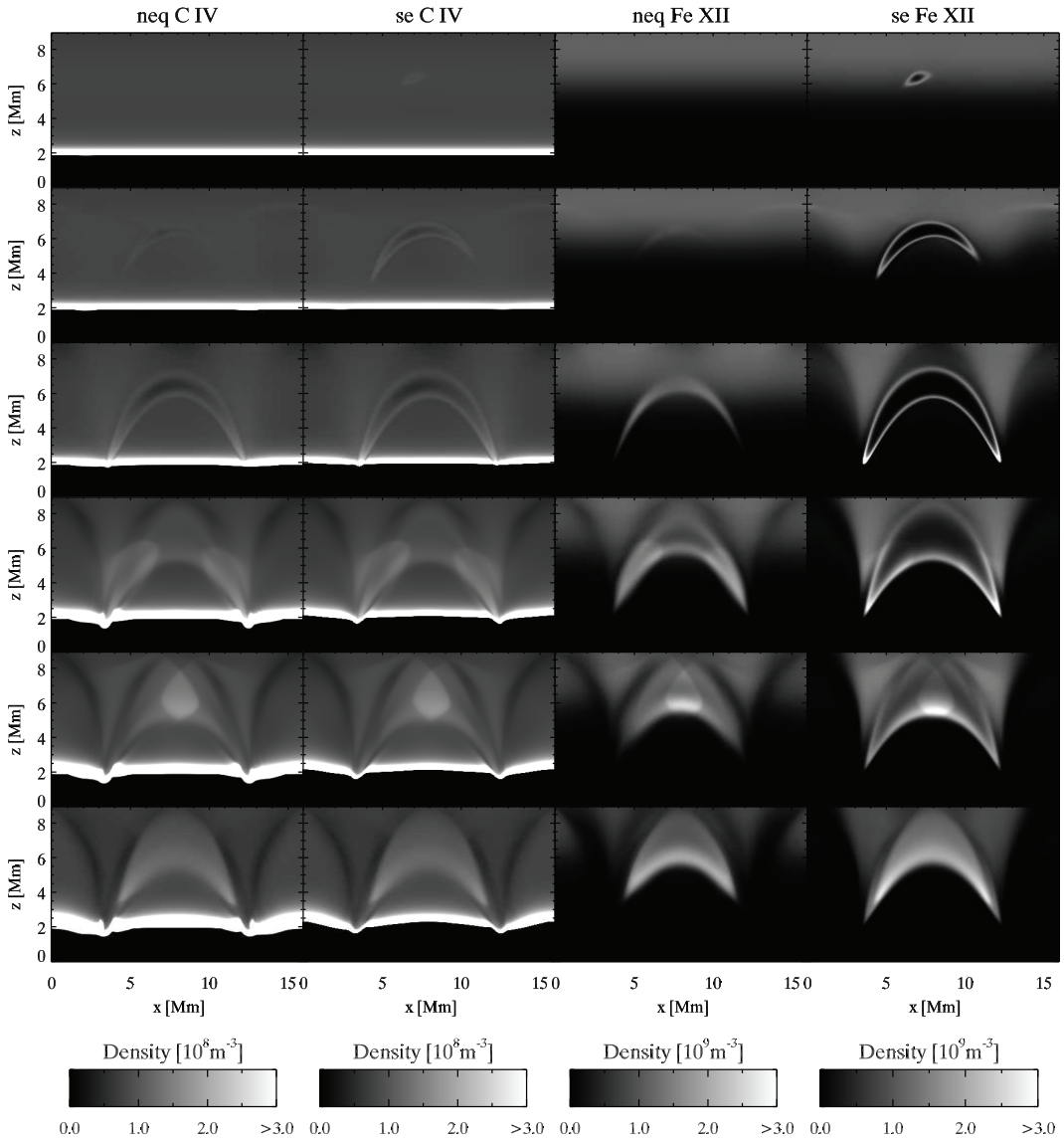

Figure 9. Time evolution of a two-dimensional model which is heated for 1 s at position $x = 9$ Mm, $z = 6.3$ Mm with 0.50 J m^{-3} over a region spanning 200 × 200 km^2. The panels show, from left to right, the NEQ C IV population density, SE C IV population density, NEQ Fe XII population density, and SE Fe XII population density.

As the ionization fronts meet at the loop apex, as seen in the 45.0 s panel of Figure 9, a high population density Fe XII blob forms. The event is caused by a collision of the two shock fronts in the gas, and in turn an increase in the temperature, causing new Fe XII ions to form, adding to the mix of Fe XII ions at the loop apex. Eventually the blob falls down along the loop legs, where each front moves back down the way it came, as shown in the 71.0 s SE panel.

The NEQ Fe XII reaction to the heating is displayed in the third column of Figure 9. There is no reaction to the temperature changes at 0.1 s in NEQ. This is because the ionization times are so high for the Fe ions; as can be seen in Figure 8 Fe XI takes some time to ionize to Fe XII.

Eventually we start to notice a change in the NEQ Fe XII population density, as shown in the 1.5 s panel of NEQ Fe XII. We see an increase in the Fe XII population density following

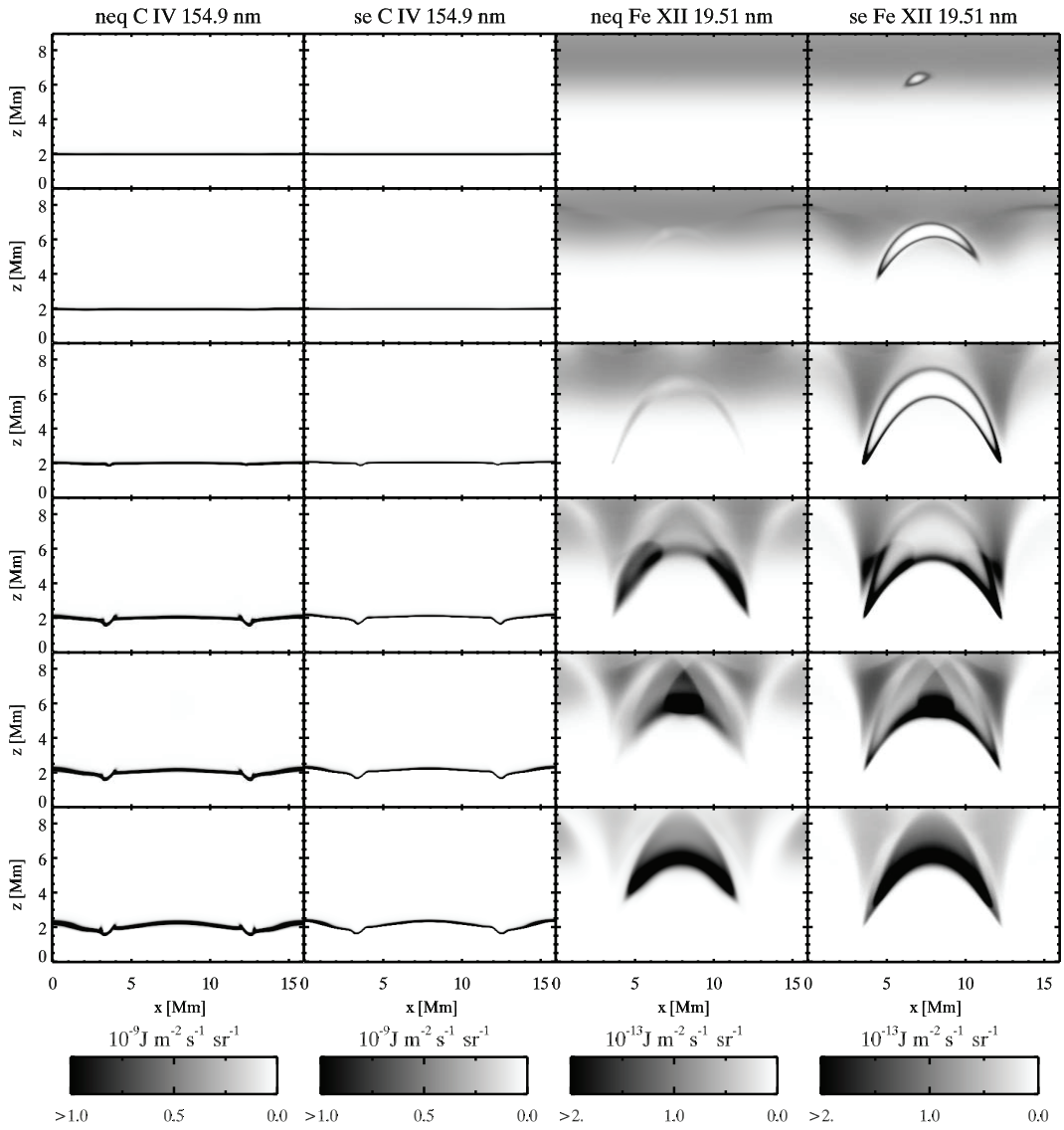

Figure 10. Emissivities of the C IV 154.9 nm line and the Fe XII 19.51 nm line, a result of the population densities presented in Figure 9.

the loop structure of the temperature, a consequence of Fe XI having by now enough time to ionize to Fe XII, as displayed in the 7.8 s panel of Figure 9.

As the temperature increase reaches the dense magnetic foot points in the chromosphere, emerging velocities affect the Fe XII population density through advection. In addition to pressure fronts, we see ionization fronts for Fe XII in NEQ, moving along with the evaporating material and being restricted by the loop structure, as displayed in the 29.0 s panel of Figure 9.

As the ionization fronts meet at the loop apex, the NEQ Fe XII population density behaves similarly to the SE case, and a high population density blob forms, eventually falling back down along the loop legs, as shown in the 71.0 s panel. The difference is that the blob is spread out along the entire loop due to the long recombination times and ionization times in the Fe ions, presented in Figure 8, causing a lag to the changes in the environment. The two fronts are wider, and fill the loop envelope more compared to the SE case. At the same time the loop structure of Fe XII density does not reach as deep into the atmosphere as the SE Fe XII density structure.

The differences between the SE and NEQ case are seen from the beginning of the experiment. Whereas the SE Fe XII ion

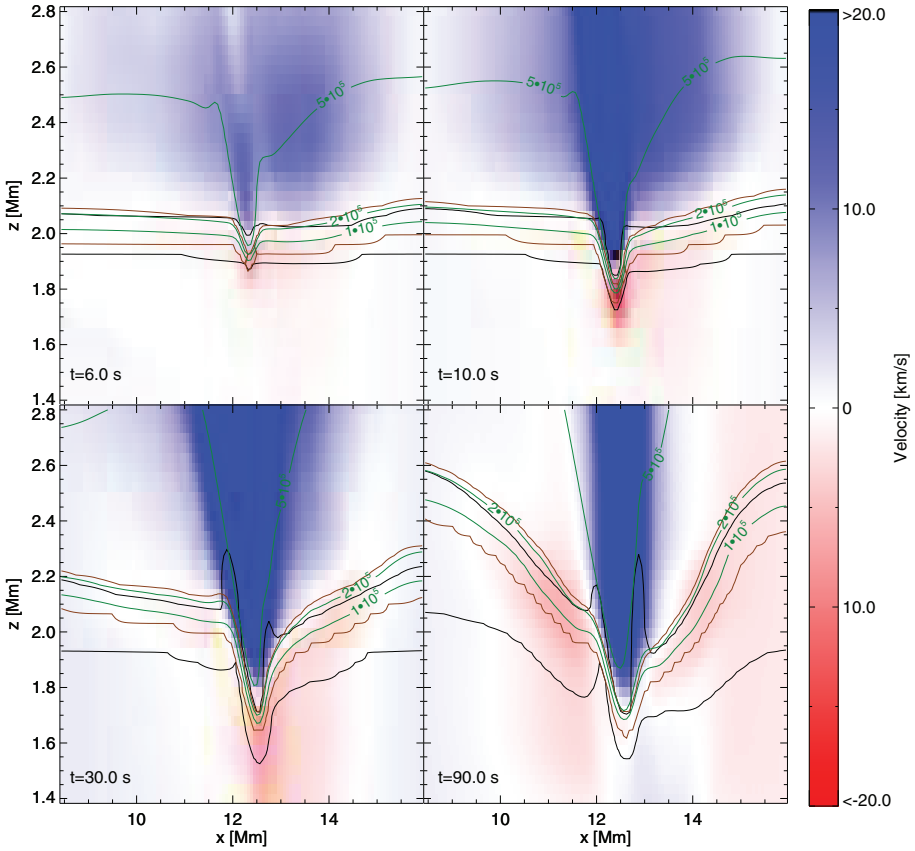

Figure 11. A closer look at C IV at transition region heights, specifically at the right loop foot point. Here we have chosen four different snapshots of the time evolution, where we present velocity maps at times 6.0 s, 10.0 s, 30.0 s, and 90.0s, with temperature contours at 100 kK, 200 kK, and 500 kK in green, and the C IV ion fraction at 0.01 in red for SE and in black for NEQ.

population density responds instantaneously to the changes in the environment, it takes some time in NEQ due to the time dependence in the rate equations. In SE, Fe XII has a higher population density and reaches deeper into the atmosphere, forming an envelope around the loop. This happens because in SE, Fe XII instantaneously reacts to the temperature increase, which becomes higher than the ionization temperature of Fe XII within the loop and therefore ionizes Fe XII to higher ionization stages. Since the ionization times are so high for the Fe ions, Fe XII takes a longer time to ionize to Fe XIII in NEQ, and we do not see this in the NEQ panels for Fe XII in Figure 9. As chromospheric gas is evaporated, advection becomes important for the NEQ Fe XII, forming ionization fronts along the loop, restricting the high Fe XII ion population density within the loop structure, while in SE the pressure fronts are also seen across the loop walls. In general, the population density of Fe XII ions there is much higher in SE than in NEQ, and reaches deeper into the atmosphere.

The emissivity evolution of the Fe XII 19.51 nm emission line mirrors that of the population densities. In general, the emissivity is much lower in NEQ than in SE, and originates from higher layers of the atmosphere. Here we see that advection is pushing the Fe XII ions to higher regions, in addition to the Fe XI ions which then ionize to Fe XII, making ionization fronts which are visible in the emission of the 19.51 nm line. In addition, the loop that forms after the ionization fronts collide is broader in NEQ. This is also shown in the emissivity of the 19.51 nm line and lives longer than in the SE case because of the long recombination time of the Fe XII ion.

A nano-flare in the corona will have an impact on the Fe XII population density, and in turn also on the emissivities of the Fe XII spectral lines, and will behave differently in NEQ and SE, due to the velocities and the long ionization and recombination times. Since C IV is more of a transition region ion, the ionization and recombination times are short in the corona, and the changes we observe in C IV happen mostly at transition region temperatures, where we see a clear deviation from SE, presented both in the population density of the ion and in the emissivity of the C IV 154.9 nm emission line.

4. CONCLUSION

With the latest developments in computing power and numerical solar physics, we are able to implement the time-dependent

rate equations into the three-dimensional numerical solar atmosphere model Bifrost. This would not be possible without the necessary tools and transition rate probabilities from the atomic diagnostics package DIPER. We have presented a method of implementing the rate equations into the numerical model, and described how the transition probabilities are collected and implemented in the solution of the rate equations.

We have shown that the rate equations are implemented correctly by comparing an SE solution to results from both DIPER and CHIANTI and the empirical atmosphere model Fal–C, and we are confident that the solution holds for all optically thin ions of choice, where DIPER provides a good model for the ionization states.

We test the implementation by creating a one-dimensional test scenario for the C IV ion, testing the effect of advection velocities in a static atmosphere. The results show how easy it is to disrupt the ionization equilibrium, even with a relatively low velocity of 1 km s^{-1} across a temperature gradient akin to that found by Joselyn et al. (1979b).

The implementation would not be possible without the assumption of an optically thin atmosphere. By calculating the optical depth of the ions studied here, we have made sure the assumption is valid. Ions originally assumed to be from optically thin regions of the atmosphere may be advected to regions where the assumption does not hold. Future studies on NEQ ionization should make sure the ions tested are actually optically thin.

We have studied the effect of a simplified nano-flare in the corona on the transition region C IV ion population density and the coronal Fe XII ion population density. We compared the SE and NEQ population densities and found that there are significant differences. The actual nano-flare does not play a significant role for the transition region C IV ion population density in the region of heat deposition, but the emerging chromospheric evaporation has an effect in the transition region through the emerging velocities, resulting in a widening of the high-density region in the vertical direction, where the emerging emission originates from a wider region of the atmosphere in NEQ than what is otherwise found in SE. The nano-flare has a direct effect on the Fe XII ion population density. In SE, the Fe XII ion population density instantaneously reacts to local changes in the environment, ionizing to higher stages. In NEQ, on the other hand, the long ionization times of the ions mean that the temperature has time to increase and then decrease due to thermal conduction, before they have time to ionize to higher stages. As thermal conduction along the magnetic field lines changes the temperature down toward the chromosphere, emerging velocities due to chromospheric evaporation make advection important in the rate equations, restricting the evolution of the Fe XII ion population density in NEQ while leading to formation of ionization fronts. In general, the ion population density of Fe XII is lower in NEQ than in SE, and originates from higher layers of the atmosphere than in the SE case.

The implementation in Bifrost is completely general, and can be run in one dimension, two dimensions, as well as three dimensions, and with any ions for which DIPER has data. We are able to synthesize emission from out of equilibrium ions and couple their evolution to that of the atmosphere. We have shown that the implementation of our NEQ solver behaves as expected and gives correct solutions of the rate equations. Through the use of simple test cases we have been able to confirm that SE is not a good approximation for C IV and Fe XII under the conditions of the simple test cases. The results are based on the underlying MHD model, so if the solar atmosphere is far from the atmosphere produced by Bifrost, the ionization results should only be carefully used when trying to invert observations. The test cases presented here are only one dimensional and two dimensional, but it is possible to do the same for more realistic three-dimensional models of the solar atmosphere. In a follow-up paper we will investigate a three-dimensional model, with a larger number of ions and a more realistic simulated solar atmosphere.

REFERENCES

Arnaud, M., & Rothenflug, R. 1985, A&AS, 60, 425
Asplund, M., Grevesse, N., Sauval, A. J., & Scott, P. 2009, ARA&A, 47, 481
Berger, T. E., de Pontieu, B., Schrijver, C. J., & Title, A. M. 1999, ApJL, 519, L97
Bradshaw, S. J., & Cargill, P. J. 2006, A&A, 458, 987
Bradshaw, S. J., & Klimchuk, J. A. 2011, ApJS, 194, 26
Bradshaw, S. J., & Mason, H. E. 2003a, A&A, 401, 699
Bradshaw, S. J., & Mason, H. E. 2003b, A&A, 407, 1127
Brekke, P. 1999, SoPh, 190, 379
Brekke, P., Wilhelm, K., Lemaire, P., et al. 1996, BAAS, 28, 879
Burgess, A., & Chidichimo, M. C. 1983, MNRAS, 203, 1269
Carlsson, M., & Leenaarts, J. 2012, A&A, 539, A39
Culhane, J. L., Harra, L. K., James, A. M., et al. 2007, SoPh, 243, 19
Dere, K. P., Landi, E., Young, P. R., et al. 2009, A&A, 498, 915
Fontenla, J. M., Avrett, E. H., & Loeser, R. 1993, ApJ, 406, 319
Griem, H. R. 1964, Plasma Spectroscopy (New York: McGraw-Hill)
Gudiksen, B. V., Carlsson, M., Hansteen, V. H., et al. 2011, A&A, 531, A154
Hansteen, V. 1993, ApJ, 402, 741
Hyman, A. 1979, in Proc. Third IMACS Int. Symp. Computer Methods for Partial Differential Equations, ed. R. Vichnevetsky & R. Stepleman (New Brunswick: IMACS), 313
Joselyn, J., Munro, R. H., & Holzer, T. E. 1979a, SoPh, 64, 57
Joselyn, J. A., Munro, R. H., & Holzer, T. E. 1979b, ApJS, 40, 793
Judge, P. G., & Meisner, R. W. 1994, in Proc. the Third *SOHO* Workshop, Solar Dynamic Phenomena and Solar Wind Consequences, ed. J. J. Hunt (ESA SP-373; Noordwijk: ESA), 67
Landi, E., Del Zanna, G., Young, P. R., et al. 2006, ApJS, 162, 261
Martínez-Sykora, J., Hansteen, V., & Carlsson, M. 2008, ApJ, 679, 871
Martínez-Sykora, J., Hansteen, V., & Carlsson, M. 2009, ApJ, 702, 129
Müller, D. A. N., Hansteen, V. H., & Peter, H. 2003, A&A, 411, 605
Müller, D. A. N., Peter, H., & Hansteen, V. H. 2004, A&A, 424, 289
Nordlund, A. 1982, A&A, 107, 1
Parker, E. N. 1988, ApJ, 330, 474
Peter, H., Gudiksen, B. V., & Nordlund, Å. 2006, ApJ, 638, 1086
Ralchenko, Y. 2005, MSAIS, 8, 96
Reale, F., & Orlando, S. 2008, ApJ, 684, 715
Shull, J. M., & van Steenberg, M. 1982, ApJS, 48, 95
Skartlien, R. 2000, ApJ, 536, 465

Paper II

Non–equilibrium ionization effects on the density line ratio diagnostics of O IV

Olluri, K., Gudiksen, B. V. and Hansteen, V.

ApJ, 767, 43 (2013)

The Astrophysical Journal, 767:43 (13pp), 2013 April 10 doi:10.1088/0004-637X/767/1/43

NON-EQUILIBRIUM IONIZATION EFFECTS ON THE DENSITY LINE RATIO DIAGNOSTICS OF O IV

K. Olluri[1,2], B. V. Gudiksen[1,2], and V. H. Hansteen[1,2]
[1] Institute of Theoretical Astrophysics, University of Oslo, P.O. Box 1029 Blindern, NO-0315 Oslo, Norway; kosovare.olluri@astro.uio.no
[2] Center of Mathematics for Applications, University of Oslo, P.O. Box 1053 Blindern, NO-0316 Oslo, Norway
Received 2012 November 21; accepted 2013 February 22; published 2013 March 22

ABSTRACT

The dynamic timescales in the solar atmosphere are shorter than the ionization and recombination times of many ions used for line ratio diagnostics of the transition region and corona. The long ionization and recombination times for these ions imply that they can be found far from their equilibrium temperatures, and spectroscopic investigations require more care before being trusted in giving correct information on local quantities, such as density and temperature. By solving the full time-dependent rate equations for an oxygen model atom in the three-dimensional numerical model of the solar atmosphere generated by the Bifrost code, we are able to construct synthetic intensity maps and study the emergent emission. We investigate the method of electron density diagnostics through line ratio analysis of the O IV 140.1 nm to the 140.4 nm ratio, the assumptions made in carrying out the diagnostics, and the different interpretations of the electron density. The results show big discrepancies between emission in statistical equilibrium and emission where non-equilibrium (NEQ) ionization is treated. Deduced electron densities are up to an order of magnitude higher when NEQ effects are accounted for. The inferred electron density is found to be a weighted mean average electron density along the line of sight and has no relation to the temperature of emission. This study shows that numerical modeling is essential for electron density diagnostics and is a valuable tool when the ions used for such studies are expected to be out of ionization equilibrium. Though this study has been performed on the O IV ion, similar results are also expected for other transition region ions.

Key words: atomic processes – magnetohydrodynamics (MHD) – methods: numerical – Sun: atmosphere – Sun: transition region – techniques: spectroscopic

1. INTRODUCTION

The upper chromosphere and lower corona are layers of the solar atmosphere with dynamic timescales shorter than the ionization equilibrium timescales of many ions dominant in the emission from this region. These long ionization and recombination times lead them to be found far from their equilibrium temperatures, and they can therefore no longer be trusted to reflect information about local quantities such as density and temperature.

Munro et al. (1971) presented a method of deriving electron densities directly from line intensity ratios of ions from the beryllium-isoelectronic sequence. In this method, one considers the ratio of the emissivity of a spectral line formed by a stable level transition to a spectral line formed by a metastable level transition, under statistical equilibrium (SE) conditions, assuming an identity between the emissivity ratio and intensity ratio. The beryllium-isoelectronic sequence and the boron-isoelectronic sequence are interesting in this context because the temperature variations of the level populations are negligible compared to the changes in ion concentration, and are therefore well suited for electron density diagnostics. Gabriel & Jordan (1972) give a detailed explanation and theoretical background for spectral line ratios and their diagnostics potential.

A common remark from these early works is that the calculations are done under equilibrium conditions where the ions are at their maximum concentration, flagging concern for the validity of the result under non-equilibrium (NEQ) conditions.

Loulergue & Nussbaumer (1974) studied C III intensity ratios, pointing out that line ratios are also critically dependent on temperature, making it difficult to uniquely determine electron densities.

By studying O IV line ratios, Flower & Nussbaumer (1975) pointed out that one must realize that an electron density determination based on the comparison of the observed *intensity* ratios and calculated *emissivity* ratios of an ion can be misleading. One should therefore compare observed intensity ratios with intensity ratios calculated by integrating the emissivities along the line of sight.

Raymond & Dupree (1978) studied electron density diagnostics through C III ratios in NEQ plasmas, solving the full time-dependent rate equations in a one-dimensional model with upflows and downflows through a large temperature gradient transition region. They conclude that the C III spectral lines are emitted from low temperature regions when NEQ effects are treated properly and downflow velocities are present. Electron densities are therefore underestimated when calculations are done assuming SE. On the other hand, outflow velocities do not change the intensity ratio and estimates of electron densities are possible. Evidence of similar results are predicted for O IV line ratios in the same paper. Feldman (1992) and Feldman et al. (1992) questioned the validity of electron density ratio diagnostics on short-duration burst in the transition region and corona, solving the time-dependent rate equations, but not including advection. They conclude that during flares, most of the transition region and coronal lines are affected by the fast changes of the atmospheric properties, and are therefore out of ionization equilibrium. This study includes the O IV ion, which we intend to study here.

Mason & Fossi (1994) wrote a thorough review paper, discussing the theoretical background, observations, and the accomplishments achieved through EUV spectroscopic diagnostics techniques. Nonetheless, they fail to acknowledge the many assumptions made in the process of carrying through the diagnostics. Among them are the assumption of an identity between the emissivity ratio and the intensity ratio, and a solar atmosphere in SE, both of which will be studied closer here.

Recent studies using line ratio diagnostics techniques have been performed by Feldman et al. (2008) in studying flaring

plasmas at the $T \approx 10$ MK range using EIS data (Culhane et al. 2007), but NEQ effects are ignored. Doyle et al. (2012) studied NEQ ionization effects (under the name of transient ionization) and the diagnostics potential of transition region spectral lines in dynamic events. They use a 0D burst model and do not include the advection term when solving the rate equations. Even with their simple model, they are able to show the importance of NEQ ionization when studying transition region intensities.

A general impression from the literature is that when the diagnostics techniques were developed in the 1970s, the scientists were aware of the complications and shortcomings of the method applied to a dynamic environment such as the solar atmosphere, despite a lack of observational support. But as data quality has improved, the possibly strong limitations of this diagnostic technique have increasingly been overlooked.

In the simplest case, the emissivity ratio method is generally used for two lines that have the same lower level but two different upper levels. By choosing spectral lines with a common level, one can make sure that the emission emerges from the same region, at least when SE conditions are assumed. An emissivity ratio can be used as a density diagnostic tool if one of the upper levels has a long spontaneous de-excitation time. In that case, the population at the upper level becomes dependent on both the collisional de-excitation and the spontaneous de-excitation, and so becomes a function of the collision rate, which for conditions in the solar atmosphere is proportional to the electron density. In addition, the collision rates are temperature dependent, and the emissivity ratio will also vary with temperature. Since the radiation does not come from a single point in space, but may originate anywhere along the line of sight, the observed intensity ratio of the two lines can be difficult to interpret. Others understand the resulting electron density to be the density at a particular temperature for which the comparing emissivity ratio is calculated at (Keenan et al. 2009). Yet some understand this value as the electron density in the volume where the contribution function for a particular spectral line peaks (Loulergue & Nussbaumer 1974). Another interpretation is that it is a weighted mean electron density over the line of sight (Munro et al. 1971). Since the line of sight often passes through the atmosphere where the temperature ranges from 10^4 K to 10^6 K and electron density ranges from 10^{10} m^{-3} to 10^{16} m^{-3}, all of the assumptions above could lead to seriously wrong and/or overly simplified estimates of the electron density.

To be able to observe the dynamic transition region, one needs high cadence, high spatial and high spectral resolution. These are all properties of the Interface Region Imaging Spectrograph (IRIS), with a planned launch in 2013 April. With IRIS, one will be able to observe the dynamic environment in the interface region, the chromosphere, and the transition region with such a high temporal resolution that NEQ effects on the emitting ions of the region will be evident. It is therefore crucial to understand how this will affect diagnostic properties. The O IV 140.1 nm and 140.4 nm spectral lines are within the IRIS wavelength coverage.

In this paper, we will study NEQ effects on the O IV line ratio, and the assumptions and limitations of the methods, by using three-dimensional numerical models of the solar atmosphere created with Bifrost (Gudiksen et al. 2011). The theoretical background for the line ratio method and the theory behind the assumptions of the deduced electron densities are explained in Section 2. A short description of the numerical code Bifrost is given in Section 3. In Section 4, the NEQ solver is described and the O IV system is presented. The electron density diagnostic results, an analysis of the contribution function, and the averaged mean electron densities are presented in Sections 5.1–5.3, respectively. A summary of the study is given in Section 6, together with the concluding remarks.

2. ELECTRON DENSITY THROUGH LINE RATIO DIAGNOSTICS

From the principle of detailed balance, we know that in the absence of external forcing, the processes of emission versus absorption will settle into an equilibrium. In an optically thin atmosphere, the description of the upward and downward rates becomes vastly simplified, and the intensity only depends on the density and temperature of the medium. Collisional excitation determines the population of excited states while spontaneous radiative de-excitation processes overwhelm the stimulated emission and collisional de-excitation processes,

$$n_u A_{ul} = n_l n_e C_{lu}(T), \tag{1}$$

where A_{ul} is the Einstein decay probability coefficient, $C_{lu}(T)$ is the collisional excitation rate at temperature T, n_e is the electron density, and n_l and n_u are the population numbers of the lower and upper levels of the transition, respectively. This is known as the corona approximation.

If the upper level of the transition has a long lifetime (small A_{ul}), the depletion process may be affected by an alternative collision loss rate as well, and Equation (1) has to be modified and now reads

$$n_u A_{ul} + n_u n_e C_{ul}(T) = n_l n_e C_{lu}(T), \tag{2}$$

where the second term on the left-hand side is of the same order or larger than the spontaneous de-excitation rate. In this case, the corona approximation breaks down and an electron density dependency is introduced. The emissivity

$$\epsilon_\nu = \frac{h\nu}{4\pi} n_u A_{ul} \tag{3}$$

is now electron density dependent through the population density n_u of the upper level. Taking the ratio of the emissivity of two transitions will then give a relation for the electron density, n_e, of the emitting region.

An example is if one takes the ratio of one transition where the corona approximation is valid and one where it fails, say the transition $g \rightarrow i$ and $g \rightarrow k$, where k has a long lifetime and has an alternative de-excitation loss rate to a level m. Under SE, the emissivity ratio is then

$$\frac{\epsilon_{\nu i}}{\epsilon_{\nu k}} = \frac{\nu_{gi}}{\nu_{gk}} \frac{C_{gi}(T)}{C_{gk}(T)} \left(1 + n_e \frac{C_{km}(T)}{A_{kg}}\right). \tag{4}$$

The emissivity ϵ is the contribution to the intensity, I_ν, at each point along the line of sight, and is given by

$$I_\nu = \int_0^s \epsilon_\nu ds. \tag{5}$$

It now follows directly that

$$\frac{I_i}{I_k} = \frac{\int_0^s \epsilon_i ds}{\int_0^s \epsilon_k ds}. \tag{6}$$

Taking ratios of measured intensity gives no direct electron density relation because of the integration of the emissivity along the line of sight. From an observer's point of view, there

is no way of knowing the emissivities along the line of sight in the solar atmosphere, so the practice is to assume an identity of the observed intensity ratio and the calculated emissivity ratio in SE (Flower & Nussbaumer 1975) at the temperature where the ionization fraction of the ion of interest peaks, and then deduce some electron density of the atmosphere. We will study this method in detail, and present the results in Section 5.1. Assuming that the intensity behaves like the emissivity, the ratio produces a value for the electron density, but it is unclear what this electron density represents. In the literature, it has been interpreted in a number of different ways, which we will study in Sections 2.1 and 2.2.

2.1. Contribution Functions and the Electron Density

Loulergue & Nussbaumer (1974) explain the deduced electron density from line ratio diagnostics as the electron density in the volume where the contribution function for a particular spectral line peaks.

The definitions of the contribution function vary as discussed by Magain (1986), but since the emission in the transition region and corona is only dependent on the density and temperature of the medium, the contribution function can be simplified (Aschwanden 2004) as

$$G(T, \nu_{ul}, n_e) = \frac{h\nu_{ul}}{4\pi} \frac{A_{ul}}{n_e} \frac{n_u^i}{n^i} \frac{n^i}{n}, \tag{7}$$

where n_u^i is the population density of level u in ionization degree i, n^i is the total population density of ionization degree i, and n is the population density of the given element of interest. Using the abundance $A_x = n/n_H$, where n_H is the hydrogen density, and the emissivity relation ϵ_ν from Equation (3), we can express the contribution function as

$$G(T, \nu_{ul}, n_e) = \frac{\epsilon_\nu}{A_x n_e n_H}. \tag{8}$$

2.2. Weighted Mean Electron Density

Munro et al. (1971) explained the deduced electron density from intensity ratios as a weighted mean electron density over the line of sight. Using this method with the emissivity of the spectral line of interest as the weight, the weighted mean average electron density becomes

$$\langle n_e \rangle = \frac{\int_0^s \epsilon n_e ds}{\int_0^s \epsilon ds}. \tag{9}$$

3. THE NUMERICAL MODEL

We investigate the method of spectral line diagnostics by constructing synthetic observations based on forward three-dimensional MHD models using the Bifrost code (Gudiksen et al. 2011), including NEQ ionization effects (Olluri et al. 2013). The model under consideration spans the solar atmosphere from the upper layer of the convection zone, 2.4 Mm below the photosphere, to the lower corona, 14.4 Mm above the photosphere. The Bifrost code solves the full radiative MHD equations on a staggered grid. In the photosphere and lower chromosphere, the radiative flux divergence is obtained using the methods of opacity-binning developed by Nordlund (1982) and solving three-dimensional scattering by methods developed by Skartlien (2000). In the chromosphere, non-LTE radiative losses are included according to Carlsson & Leenaarts (2012). In the transition region and corona, thermal conduction along magnetic field lines is included as described by Hansteen & Gudiksen (2005) and Gudiksen et al. (2011), and optically thin radiative losses are assumed. In essence, the code attempts to be as realistic as possible within the computational constraints of today's supercomputing facilities.

The particular experiment used for this study models the upper convection zone to the lower corona within a computational domain of $512 \times 512 \times 496$ grid points spanning $24 \times 24 \times 16$ Mm^3, with a uniform horizontal grid spacing of 47.6 km and a non-uniform grid spacing in the vertical direction. The non-uniform grid spacing in the vertical z direction is set up to resolve the strong gradients in the photosphere and chromosphere ranging from a minimum of 18 km in the photosphere to 80 km in the corona. A three-dimensional snapshot taken during the model run showing the magnetic field topology and the temperature structure of the transition region is presented in Figure 1.

The model is initially seeded with a magnetic field, which by the photospheric motions is rapidly stressed enough so that the dissipation of magnetic energy maintains coronal temperatures in the upper part of the computational domain. The model has an average unsigned flux of 48 G in the photosphere, at $z = 0$ Mm. The magnetic field is concentrated at two locations in the photosphere of opposite polarity, placed diagonally in the computational box.

4. NON-EQUILIBRIUM IONIZATION OF OXYGEN

We have constructed a 14-level atomic model for the oxygen atom using DIPER (Judge & Meisner 1994), which have a database of transition rate probabilities collected from various sources such as the NIST spectroscopy database (Ralchenko 2005), CHIANTI 5.2 (Landi et al. 2006) along with many others (see the DIPER reference guide for a complete list of sources[3]), and proceed by solving the rate equations as described in Olluri et al. (2013):

$$\frac{\partial n_i}{\partial t} + \nabla \cdot (n_i \mathbf{u}) = \sum_{j \neq i}^{N_l} n_j P_{ji} - n_i \sum_{j \neq i}^{N_l} P_{ij}, \tag{10}$$

where n_i is the population density of ion level i, N_l is the total number of levels in the model atom, P_{ij} is the transition rate coefficient between level i and level j, and $\mathbf{u}$ is the macroscopic velocity. Operator splitting is used to solve the equation in two steps: first, the continuity equation on the left-hand side is forwarded in time using a first-order upwind scheme, after which this solution is used to solve the time-dependent population balance. By the optically thin approximation, the remaining equations are reduced to a linear set $\mathbf{n} = \mathbf{A}^{-1}\mathbf{n}^*$, with an $N_l \times N_l$ rate matrix $\mathbf{A}$ where the elements $A_{ii} = (1 + \Delta t \sum_{j \neq i} P_{ij})$ and $A_{ij} = -\Delta t P_{ji}$. $\mathbf{n}^*$ are the advected population densities. We have tested the validity of the optically thin approximation on the O IV 140.1 nm and 140.4 nm spectral lines used for the study here. The optical depths are below one and the approximation holds.

The rate equations are solved at every time step in the simulation, using the temperature, advection velocity, and mass density at each grid point. This way, the solution of the rate

[3] New improved ionization and recombination rates are available (Dere et al. (2009) and references therein), which effect the ionization equilibrium (Bryans et al. 2006). These data were not available with the DIPER 1.0 version used for this work, and are therefore not accounted for.

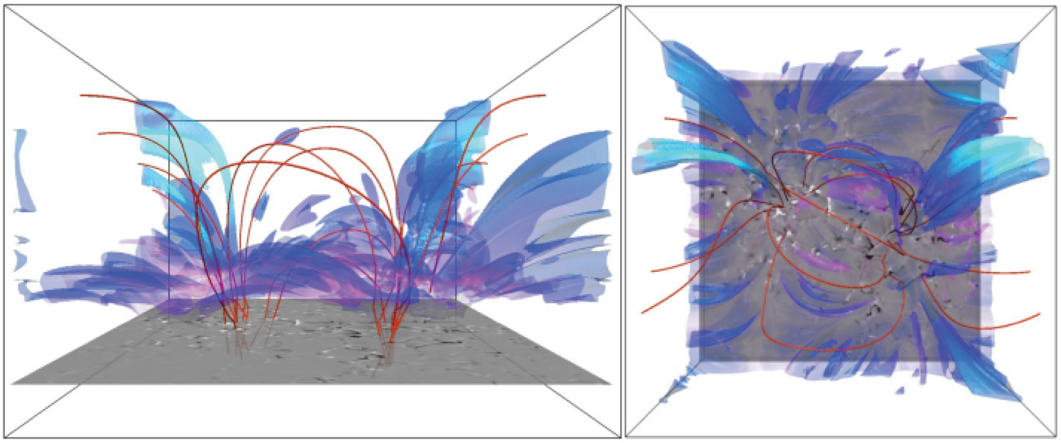

Figure 1. Three-dimensional snapshot of the three-dimensional MHD model, in an "xz" view in the left panel and an "xy" view in the right panel. The gray-scale slice represents the strength of the magnetic field, with opposite magnetic field concentration along the diagonal as seen on the right panel. The isosurface represents the temperature at 10^5 K, where the color scale indicates the plasma density, with the low plasma density in light blue to the high density plasma in pink. Some selected magnetic field lines are shown in red, giving an indication of the magnetic field topology in the corona.

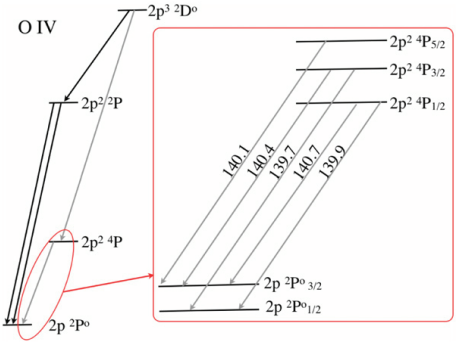

Figure 2. Grotrian diagram of the O IV levels in the atomic model on the left, where the black arrows represent allowed transitions and the gray arrows represent forbidden transitions. A blowup of the O IV $2p^2\,P^o - 2p^2 4P$ multiplet is shown on the right.

equations is at all times coupled to the overall dynamics of the synthetic atmosphere. All the levels of the O IV ion in the atomic model are presented in a Grotrian diagram in Figure 2, where the black arrows represent allowed transitions and the gray arrows represent forbidden transitions. A blowup of the O IV $2p^2\ P^o - 2p^2\ 4P$ multiplet is shown on the right. The $2p^2 4P$ levels are metastable, and all the transitions between O IV $2p^2\,P^o$ and $2p^2\,4P$ are forbidden. Line pairs of these transitions are common in electron density diagnostics (Nussbaumer & Storey 1982; Keenan et al. 2009) because of the difference in the spontaneous decay rate of each line. In this paper, we will study the ratio

$$\text{ratio} = \frac{2s^2 2p^2\, P_{3/2} - 2s 2p^2\, {}^4P_{5/2}}{2s^2 2p^2\, P_{3/2} - 2s 2p^2\, {}^4P_{3/2}}, \qquad (11)$$

which represents the O IV 140.1 nm to the O IV 140.4 nm line ratio, which have spontaneous decay rates of 1162.87 s^{-1} and 289.456 s^{-1}, respectively.

5. RESULTS

We let the simulation run for 20 minutes solar time to reach a semi-equilibrium. That equilibrium is not to be understood as SE for the ions, but rather as an equilibrium that results for the ionization stages, when averaging over a large spatial volume. It is not the distribution of the ionization stages in a single column of the atmosphere because these columns can vary significantly over time. The distribution in a single column depends on the history of both advected ion populations and heating and cooling of the plasma, which all are very intermittent in time. The ion fractions for the whole simulated volume are as presented in the form of probability density functions (PDFs) in Figure 3: the out of ionization equilibrium results are plotted in black, and what the equivalent would be in SE are plotted in red. We see that the oxygen ion distributions are far from collisional ionization equilibrium.

The O II ion fraction distribution is moved to lower temperatures by two processes: advection of O II and O III by downward velocities, where it accumulates because of the long recombination times to O II as well as recombination of O III ions to O II ions. The O III ion fraction distribution covers a wider temperature region because O IV recombines to O III after being advected to lower temperature regions as well as O II ionizing as a result of upward velocities, when they are advected to higher temperature regions. Because of the long recombination times of O III, O III accumulates at low temperatures and the ion fraction distribution gains a tail toward lower temperatures. The same is the case for O IV; O V ions recombine after being advected to lower temperature regions as well as ionization of O III as a result of upward velocities, where they are advected to higher temperature regions. We see that the ion fraction distribution is for the most part to lower temperatures for these three ions compared to their SE distribution. This is mainly caused by high recombination times of the ions at low temperatures. Low ionization times above equilibration temperatures cause these ions to ionize to higher ionization stages.

The O V ion fraction is much greater in NEQ than in SE, and the whole distribution is shifted to higher temperatures. While

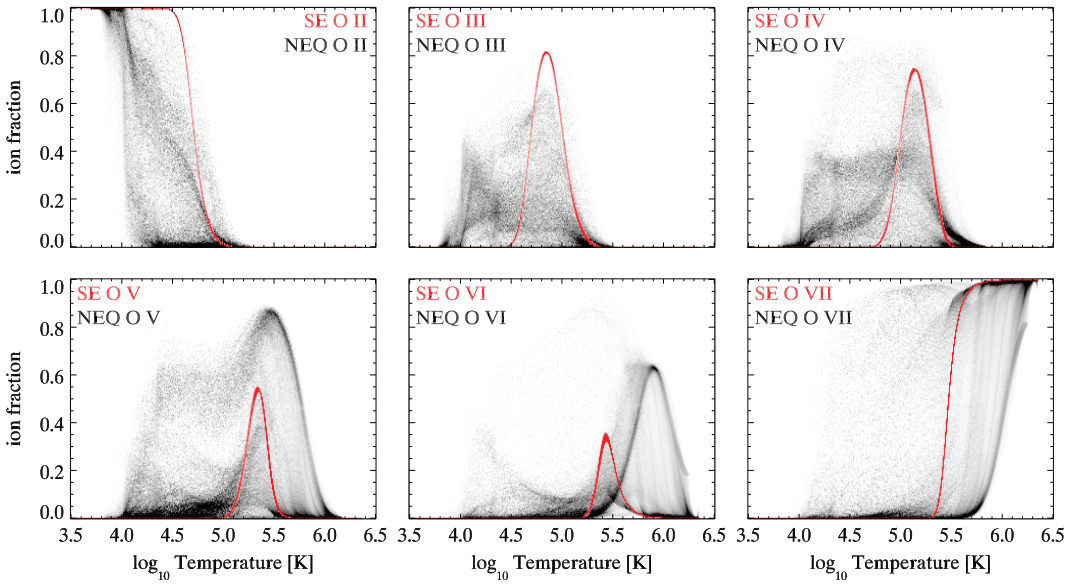

Figure 3. PDFs of the ion fractions for the ions included in the 14 level atomic model of oxygen, going from O II to O VII. The black PDFs are results from the solution of the time-dependent rate equations, showing the ions out of ionization equilibrium, while the overplotted red PDFs are the statistical equilibrium solutions.

oxygen ions in lower ionization stages were mostly affected by the downward velocities, we here see a result of upward advection, as the distribution of O V ion fractions is spread at a large temperature range, from $\log_{10} T = 4.0$ to $\log_{10} T = 6.2$. The high ion fraction of O V at low temperatures is caused by O VI being advected to lower temperature regions and recombining to O V, while the high O V ion fraction at the higher temperatures is caused by upward velocities and the long ionization times of O V at these temperatures. The overall greater ion fraction of O V is mainly caused by O IV ions being advected to higher temperature regions, and therefore ionizing to O V. The same behavior is seen for O VI and O VII, where upward advection velocities have shifted the distributions to higher temperature regions. The long ionization times at these temperatures cause an accumulation of the ion fractions, causing a higher maximum ion fraction of the ions in NEQ compared to the SE distribution.

Let us continue by examining how this affects the line ratio diagnostics using the O IV 140.1 nm to the O IV 140.4 nm line ratio.

5.1. Electron Density through Line Ratio Diagnostics

We have created synthetic intensity maps of the O IV 140.1 nm and 140.4 nm spectral lines. The 140.1 nm line is shown in Figure 4, both in SE and NEQ. From the intensity maps alone, we can see the that the ionization equilibrium plays an important role. The intensity mainly emerges from the center of the computational domain in SE, while in NEQ it is distributed more evenly. Based on this difference, we can expect the intensity ratio to be different in NEQ compared to SE.

We have used DIPER to calculate the emissivity ratio for the O IV 140.1 nm to the O IV 140.4 nm line:

$$\text{ratio} = \frac{\epsilon(2s^2 2p^2\, P_{3/2} - 2s2p^{2\,4}P_{5/2})}{\epsilon(2s^2 2p^2\, P_{3/2} - 2s2p^{2\,4}P_{3/2})} \qquad (12)$$

at the SE peak temperature of the O IV ion fraction, at $\log_{10} T = 5.15$. This is plotted in the top right panel of Figure 5. In the top left panel of Figure 5, we have plotted the electron density at $\log_{10} T = 5.15$ from the simulation. This is the electron density that one assumes is the result of the ratio diagnostics when using the emissivity ratio plotted in the top right panel of Figure 5.

The intensity ratio from the 140.1 nm to the 140.4 nm line in SE results in the electron density displayed in the middle left panel of Figure 5. This electron density is almost identical to the electron density from the simulation, meaning that if the population densities were in SE, then the method of line ratio diagnostics would succeed in reproducing the desired electron density.

The intensity ratio from the NEQ case results in the electron density displayed in the bottom left panel of Figure 5. This electron density is very different from the electron density from the simulation. This means that when the ion is out of ionization equilibrium, which the O IV clearly is, as seen in Figure 3, combined with line-of-sight effects, the method of line ratio diagnostics is of restricted use when it comes to reproducing the desired electron density. The differences in the deduced electron densities are displayed in the bottom right panel of Figure 5. There is up to an order of magnitude difference between the electron density from an SE atmosphere compared to the NEQ atmosphere.

The vertical velocity at $\log_{10} T = 5.15$ is plotted in the middle right panel of Figure 5. The features in the velocity map cannot be linked in a simple way to the features in the electron density map, and there is no evidence that the velocity at the peak temperature has any relation to the deduced electron density. The velocity affects the population densities of the ions through advection, moving ions to higher layers of the atmosphere, allowing ions to ionize to higher ionization degrees, but also to lower denser regions of the atmosphere where ions recombine

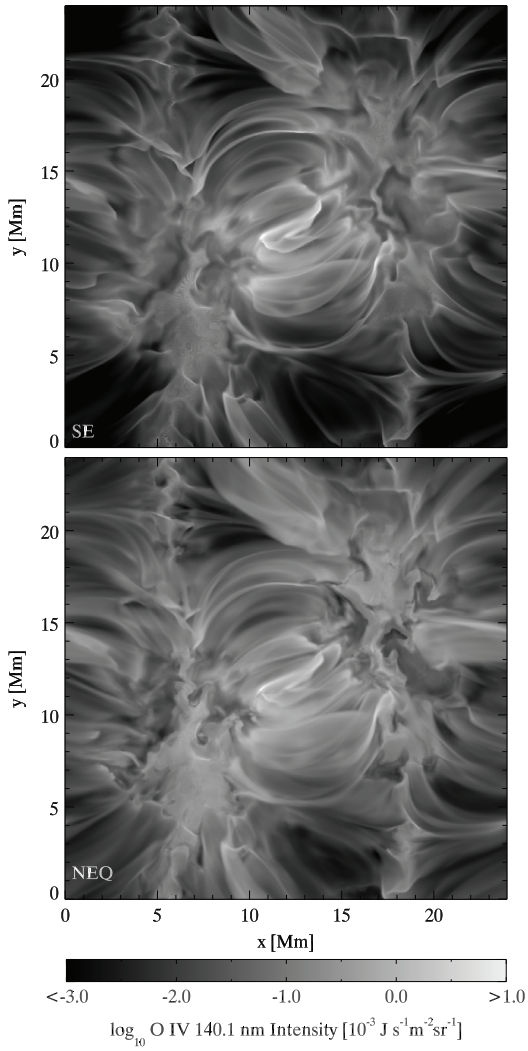

Figure 4. Synthetic intensity maps from the O IV 140.1 nm spectral line, from a statistical equilibrium atmosphere in the top panel and from an atmosphere for which the full time-dependent rate equations are solved, resulting in non-equilibrium ionization in the bottom panel.

to lower ionization degrees. It is therefore not only the velocity at the peak temperature of ionization O IV that will affect the ionization degree, but the changing velocity throughout the different layers of the atmosphere.

Solving the time-dependent rate equations can potentially have two possible outcomes. Ions can be removed from out of ionization equilibrium and/or each ion can also get out of excitation equilibrium. Since both of these scenarios can affect the intensity ratio, and thus the electron density derived, it is of interest to study which is the dominant effect leading to the inferred electron density.

In the top panel of Figure 6, we have plotted the ionization and recombination times for the O IV ion at $n_e = 10^{14}$ m^{-3} as a function of temperature. Both ionization and recombination times are high, which means that when O IV ions are moved to regions of either lower or higher temperatures, it takes some time before the ion can ionize or recombine, and can therefore easily get out of ionization equilibrium, as reflected in Figure 3.

In the bottom panel of Figure 6, we have plotted the population and depopulation times of the levels within the O IV ion at $n_e = 10^{14}$ m^{-3} as a function of temperature. These times are low, resulting in approximately instantaneous equilibration within the ion when the ion is advected to lower or higher temperature regions. We therefore expect the inferred electron density diagnostics from the bottom left panel of Figure 5 to be caused mainly from O IV being out of ionization equilibrium.

We test this by forcing the level populations within the O IV ion to be in excitation equilibrium through

$$n(\mathrm{O\,IV}\ i)^{\mathrm{neq}}_{\mathrm{ex}} = \frac{n(\mathrm{O\,IV}\ i)^{\mathrm{se}}}{n(\mathrm{O\,IV})^{\mathrm{se}}} n(\mathrm{O\,IV})^{\mathrm{neq}}, \quad (13)$$

where $n(\mathrm{O\,IV})^{\mathrm{neq}}$ is the NEQ population density of O IV, $n(\mathrm{O\,IV})^{\mathrm{se}}$ is the SE population density of O IV, and $n(\mathrm{O\,IV}\ i)^{\mathrm{se}}$ is the level population of level i from the SE solution. This means that we find the population fraction of each level within O IV in SE and multiply this with the NEQ O IV population density, resulting in a population density of each level in excitation equilibrium, but out of ionization equilibrium, $n(\mathrm{O\,IV}\ i)^{\mathrm{neq}}_{\mathrm{ex}}$. With these new results, we do density diagnostics using the emissivity ratio from Figure 5 and find a new electron density. This is plotted in the left panel of Figure 7. In the right panel of Figure 7, we have plotted the ratio between the electron density derived from out of excitation equilibrium of O IV (from the bottom left panel of Figure 5) and the electron density derived from excitation equilibrium of O IV. This ratio is very close to unity at every grid point, with an rms = 1.002. We conclude that the electron density derived through line ratio diagnostics is mainly caused by O IV being out of ionization equilibrium, and that the excitation NEQ is unimportant in this context.

In the next sections, we investigate the different interpretations of inferred electron density from the NEQ atmosphere and investigate its origin.

5.2. Contribution Functions and the Electron Density

From Section 2.1, we know that the electron densities deduced from line ratios can be explained as the electron density from the peak of the contribution function for the given lines. We investigate this by calculating the contribution functions of the 140.1 nm and 140.4 nm spectral lines from our synthetic atmosphere.

We have plotted the contribution functions of five arbitrary columns in a snapshot of the simulation in Figure 8. These columns are marked with numbering in the density images in Figure 5, where the numbers 1–5 represent the row of panels here, from left to right. In the top two rows of panels, the contribution functions are plotted for the lines investigated here. The blue line is the contribution function for the SE solution and the black line for the NEQ solution. The bottom two rows of panels show the electron density and temperature for the respective column. One of the interpretations of the electron density deduced from the intensity ratio is that it reflects the electron density where the contribution function peaks. As we can see from the contribution functions plotted in Figure 8, only one has a clear distinct peak, while most have several peaks from a wide electron density range. If we disregard the multiple peaks

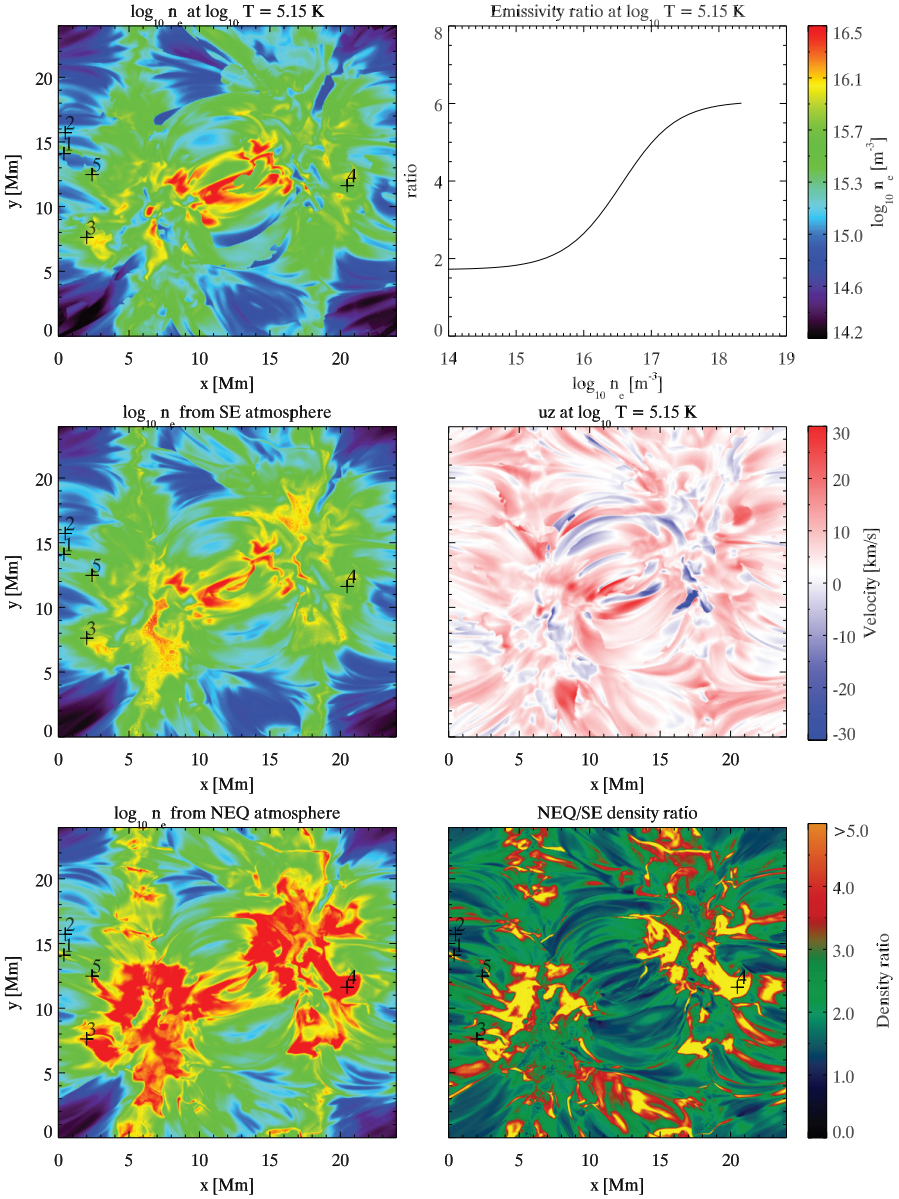

Figure 5. Electron density at $\log_{10} T = 5.15$ from the simulation in the top left panel. The emissivity ratio of the 140.1 nm on 140.4 nm line ratio from DIPER at $\log_{10} T = 5.15$ is shown in the top right panel. The electron density deduced from the DIPER emissivity ratio for an SE atmosphere is shown in the left middle panel and from an NEQ atmosphere is shown in the bottom left panel, and the ratio on these two deduced electron densities is shown in the bottom right panel. The vertical velocity at $\log_{10} T = 5.15$ is shown in the middle right panel. The density images in the left panels and the density-ratio image in the bottom right panel have five positions marked with numbers, indicating the positions of the columns of Figure 8, where the numbers 1–5 represent the row of panels of Figure 8, from left to right.

and just look at the peak with the highest value, then the two lines involved in the ratio diagnostics peak at different electron densities.

We have plotted the electron densities deduced from the peak of the contribution functions along each column in the computational domain in Figure 9. The results from the SE solutions are plotted in the top panels and the results from the NEQ solution are plotted in the bottom panels. In SE, the contribution functions for the 140.1 nm and 140.4 lines seem to peak at electron densities similar to the SE results from Figure 5. Nonetheless, the contribution function peak for the two lines gives different electron densities, as displayed in the ratio plot

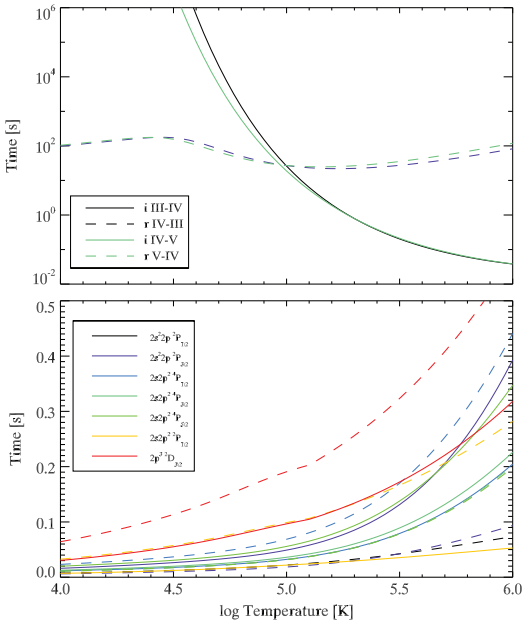

Figure 6. Ionization (–) and recombination (- -) times for the O IV ion at $n_e = 10^{14}$ m^{-3} as a function of temperature are plotted in the top panel. Including only collisional transitions, the population (–) and depopulation (- -) times of each level within the O IV ion are plotted in the bottom panel. The population and depopulation times are low enough to keep O IV in excitation equilibrium.

in the top right panel of Figure 9. The contribution functions from the NEQ solutions peak at electron densities similar to the equilibrium results.

This happens because the contribution function is inversely proportional to the electron density (see Equation (8)). We have plotted the electron density from the simulation together with the emissivities, both in SE and NEQ, in Figure 10. As we can see from the plot, the NEQ emissivities are shifted to lower heights of the atmosphere due to advection and high recombination times of the O IV ions discussed in Section 5. At these heights, the electron densities are large compared to the SE emissivities, which peak at lower electron densities located at higher layers of the atmosphere.

Because of the nature of the definition of the contribution function, the contribution function falls off rapidly in value as the electron density increases, and the NEQ effects on the contribution functions from the emissivities rapidly vanish. Because of this, the inferred electron densities from the peak of the contribution functions are similar when comparing NEQ and SE contribution functions.

There are still some differences between the electron densities deduced from the 140.1 nm contribution function peak and the 140.4 nm contribution function peak in NEQ. Nonetheless, if there was a way of knowing the contribution function along the line of sight, one would be able to derive the electron density at the peak temperature.

5.3. Weighted Mean Averaged Electron Density

From Section 2.2, we know that the electron densities deduced from line ratios can be explained as a weighted mean electron

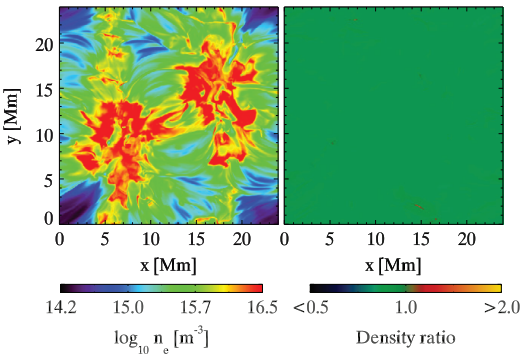

Figure 7. Electron density derived using line ratio diagnostics, from O IV in excitation equilibrium and out of ionization equilibrium in the left panel. The ratio between the electron density derived from out of excitation equilibrium O IV (from the bottom left panel of Figure 5) and the electron density derived from excitation equilibrium O IV is plotted in the right panel, which is unity at close to every grid point.

density of the respective spectral lines involved in the line ratio. We investigate this by calculating the weighted mean averaged electron densities from our synthetic atmosphere, using the emissivities of the 140.1 nm and 140.4 nm spectral lines, in SE and NEQ, as weights.

Weighted mean averaged electron densities are plotted in Figure 11. In the top left panel is the $\langle n_e \rangle^{SE}_{140.1}$, in the top middle panel is the $\langle n_e \rangle^{SE}_{140.4}$, and the ratio of these two is shown in the top right panel. In the bottom left panel is the $\langle n_e \rangle^{\mathrm{NEQ}}_{140.1}$, in the bottom middle panel is the $\langle n_e \rangle^{\mathrm{NEQ}}_{140.4}$, and the ratio of these two is shown in the bottom right panel. We see that the SE $\langle n_e \rangle$ are very similar to the ones deduced through line ratio diagnostics in SE. Also, there are only small differences between the 140.1 nm and the 140.4 nm results. The NEQ $\langle n_e \rangle$ are also very similar to the electron densities deduced from the NEQ intensity ratios. This is because the NEQ effects are included in the averaging due to the NEQ emissivity weights, and the effect is not repressed as it was for the contribution functions in Section 5.2.

There are some differences between the 140.1 nm and 140.4 nm NEQ emissivity weights used, as displayed in the density ratio in the bottom right panel, due to different NEQ effects on the $2s^2 2p^2\, ^3P_{3/2}$, $2s2p^2\, ^4P_{5/2}$, and $2s2p^2\, ^4P_{1/2}$ levels forming the two spectral lines.

Since the intensity ratio should give a weighted mean electron density (Munro et al. 1971), we plot the intensity ratio from the five columns used for the contribution functions in Figure 8 as a function of the four averaged mean electron densities for the respective columns from Figure 9 in Figure 12. In the same plot are also the emissivity ratios in SE (red) and NEQ (blue) for the given column. We see that the resulting intensity ratio for the given column does not always correlate with the emissivity ratio of the column, but if we group the intensity ratio for the NEQ intensities with the resulting NEQ weighted mean electron densities for the column, then the correlation improves. This correlation is also valid for the SE results.

This method gives electron densities similar to the electron densities at the formation temperature of $\log_{10} T = 5.15$ for both SE and NEQ conditions. Since there is no way of knowing the electron density where the contribution function peaks in advance, this method unfortunately cannot be used to find

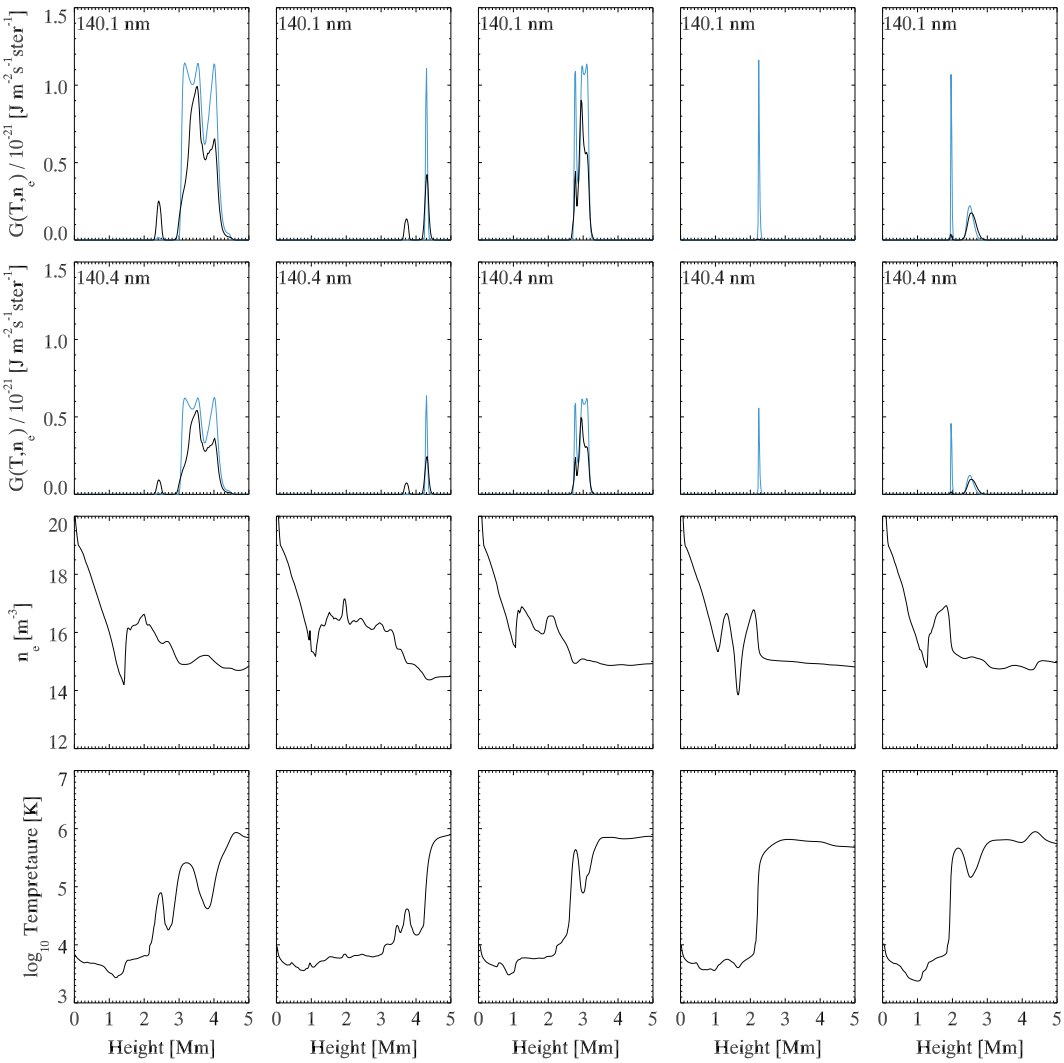

Figure 8. Contribution functions of five arbitrary columns in a snapshot of the simulation. Each column is marked with a "+" in Figure 5 and a number from 1 to 5, indicating each column of panels here, from left to right. The contribution functions for the 140.1 nm and 140.4 nm lines are plotted in the top two rows of panels. The blue line is the contribution function for the SE solution and the black line for the NEQ solution. The bottom two rows of panels show the electron density and temperature for the respective column.

the electron density at the formation temperature of the ion investigated.

6. SUMMARY AND CONCLUSION

We have studied the spectral line electron density diagnostics technique using the O IV 140.1 nm and 140.4 nm spectral lines. If the assumption of the O IV ion being in ionization equilibrium was valid, then the technique would be able to reproduce the desired result, which is to find the electron density at a given temperature, when assuming an identity between the intensity ratio and the emissivity ratio. But when solving the full time-dependent rate equations for an oxygen model atom, we find that all oxygen ions are out of ionization equilibrium. A high ion fraction of all ions is found at both lower and higher temperatures than their equilibration temperature.

Focusing on the O IV ion, we see a high ionization fraction stretching all the way down to below $\log_{10} T = 4$, and up to temperatures as high as $\log_{10} T = 5.8$. Since most of the low temperatures come from a lower region of the solar atmosphere, the electron densities from these regions are high. We therefore expect the emission from NEQ O IV ions to arise from regions of higher electron densities compared to the SE case.

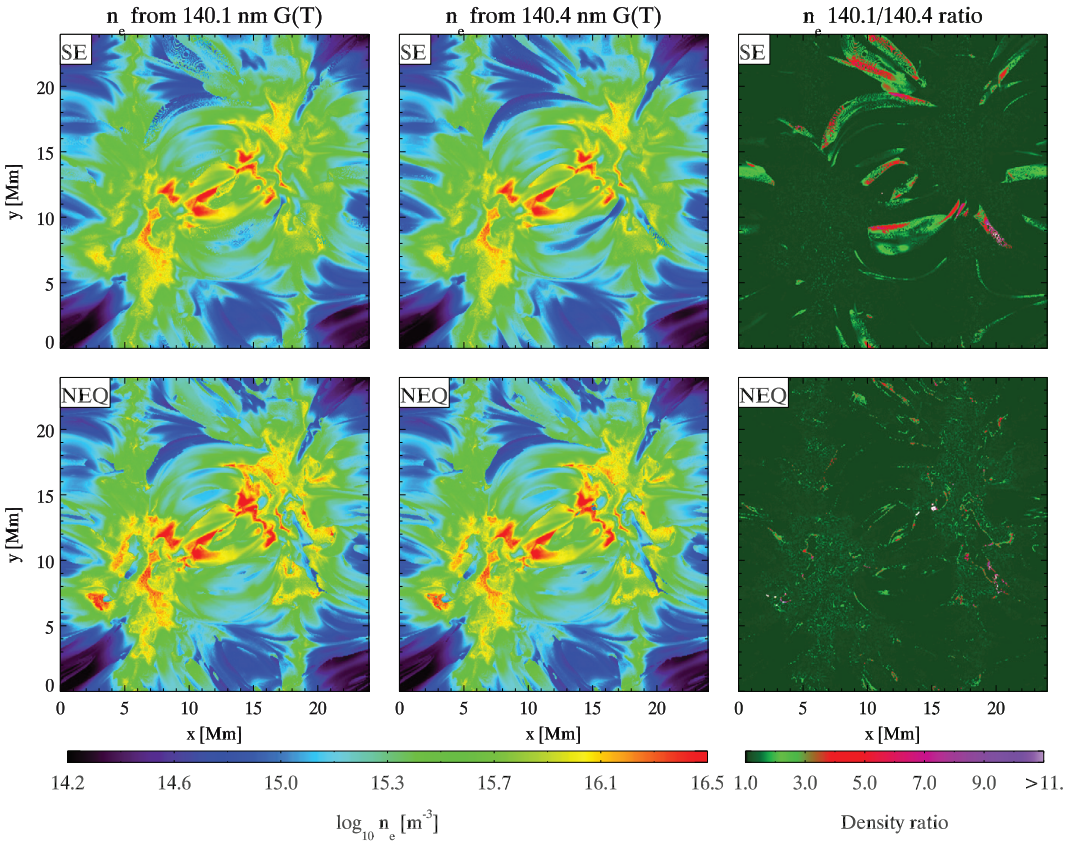

Figure 9. Electron densities deduced from the peak of the contribution functions along each column in the computational domain. The results from the SE solutions are plotted in the top right and middle panels, and the results from the NEQ solution are plotted in the bottom right and middle panels. The respective electron density ratios are plotted in the left column of panels.

Emissivity ratios are constructed for a specific temperature, using spectral lines that are sensitive to electron density variations, and not so sensitive to temperature variations. We have constructed an emissivity ratio curve for the 140.1 nm to 140.4 nm spectral lines at the equilibration temperature of O IV, $\log_{10} T = 5.15$. Because the O IV ion is out of ionization equilibrium, the electron density obtained with this method is not consistent with the electron density at $\log_{10} T = 5.15$. One could imagine that the error in the deduced electron density was due to the O IV ion being out of excitation equilibrium, but we show that the change in intensity, and therefore the erroneous electron density, is caused by the ion being out of ionization equilibrium.

The electron density derived using the line ratio technique is plotted in the left column of Figure 13, where we have created PDFs of the derived electron densities as function of the electron density at $\log_{10} T = 5.15$. The derived electron density can be up to one order of magnitude different than the electron density at $\log_{10} T = 5.15$, when out of equilibrium effects are accounted for. When SE is assumed, the PDF is linear.

We investigate if the derived electron density is the electron density for the peak of the contribution function. Given that the intensity ratio results in a single electron density and the contribution functions give two differing electron densities for each line, this method is inconsistent. We are not able to reproduce the electron densities from the NEQ O IV line ratio by this method as presented in the right column of panels in Figure 13. The reason for this is the definition of the contribution

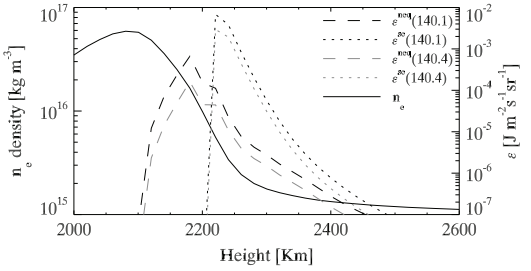

Figure 10. Electron density (whole) is plotted together with the NEQ emissivities (dashed) and the SE emissivities (dotted) as a function of the height in the simulation, where black represents the 140.1 nm line and gray the 140.4 nm line. The figure shows results from column four of Figure 8 where the differences between NEQ and SE inferred densities are large. As we can see from this plot, the NEQ emissivities are shifted to lower regions of the atmosphere and have lower peak values compared to the SE emissivities.

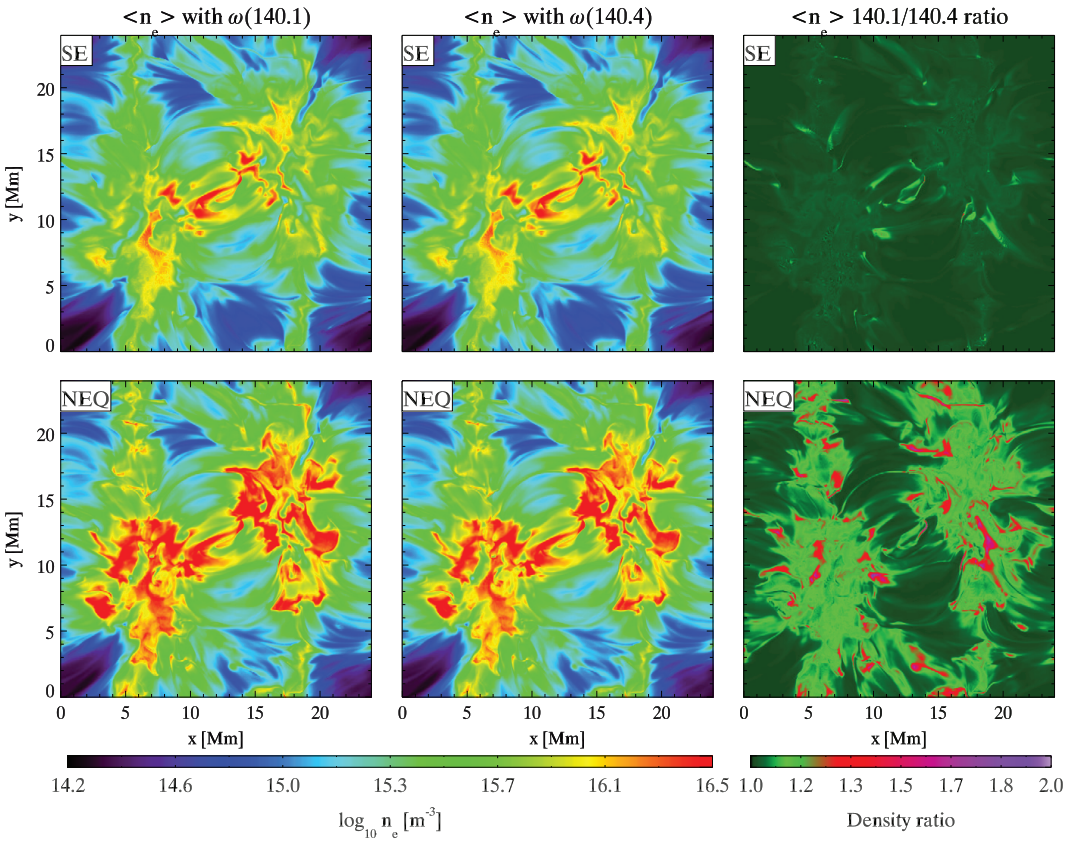

Figure 11. Weighted mean electron densities. In the top left panel is the $\langle n_e \rangle^{\rm SE}_{140.1}$, in the top middle panel is the $\langle n_e \rangle^{\rm SE}_{140.4}$, and the ratio of these two is shown in the top right panel. In the bottom left panel is the $\langle n_e \rangle^{\rm NEQ}_{140.1}$, in the bottom middle panel is the $\langle n_e \rangle^{\rm NEQ}_{140.4}$, and the ratio of these two is shown in the bottom right panel. We see that the SE $\langle n_e \rangle$ are very similar to the ones deduced through line ratio diagnostics in SE. Also, there are only small differences between the 140.1 nm and 140.4 nm results. The NEQ $\langle n_e \rangle$ are also very similar to the electron densities deduced from the NEQ intensity ratios, but there are some differences between the 140.1 nm and 140.4 nm emissivity weights used, as displayed in the density ratio in the bottom right panel.

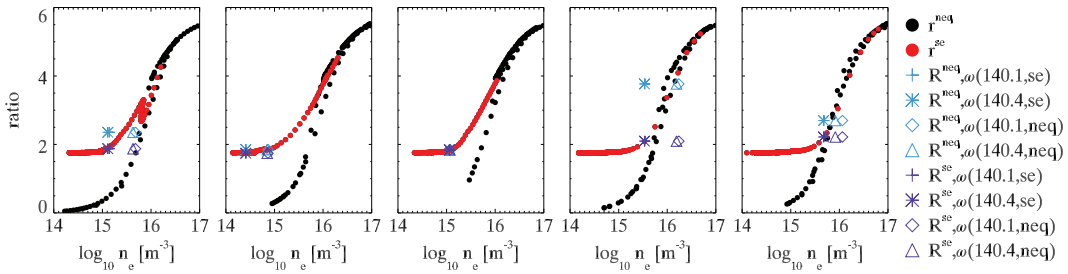

Figure 12. Emissivity ratios (r) from the five columns from Figure 8 as a function of the electron density along the column in black (NEQ) and red (SE). The purple symbols represent the intensity ratio (R) for the given column in SE as a function of the four $\langle n_e \rangle$. The blue symbols represent the intensity ratio (R) for the given column in NEQ as a function of the four $\langle n_e \rangle$. The four $\langle n_e \rangle$ are from the top four panels of Figure 11. ω represents the weight for given spectral lines (140.1 nm, 140.4 nm) and under given conditions (SE, NEQ).

function, which is inversely proportional to the electron density. Because of this, the NEQ effects entering the contribution function through the emissivity rapidly vanish as the electron density increases. Because of this, the contribution functions where we have used NEQ emissivities and the contribution functions where we have used SE emissivities result in similar electron densities. However, if we were able to know where the contribution function peaks, then we would be able to find the electron density at the peak temperature. The results of the contribution functions also show that the contribution

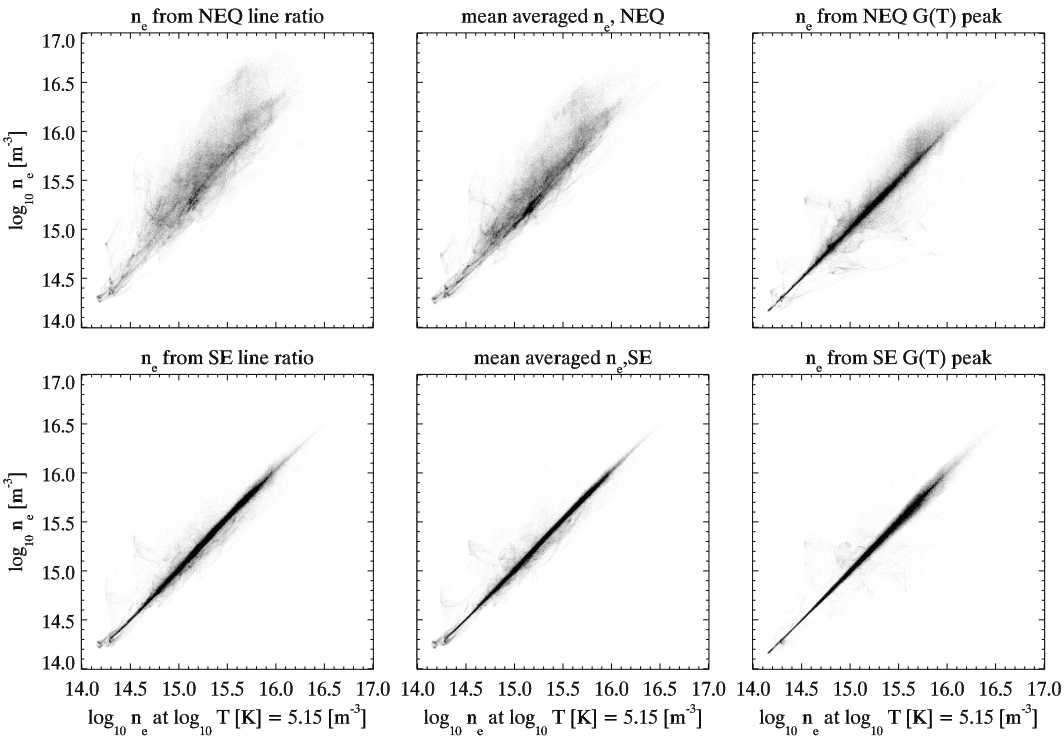

Figure 13. Deduced electron densities as a function of the electron density at $\log_{10} T = 5.15$ in the computational domain. The top panels are the results from the NEQ atmospheres and the bottom panels from SE atmospheres. In the left column of panels are the electron densities deduced from the emissivity ratio at $\log_{10} T = 5.15$, in the middle column of panels are the averaged mean electron densities when weighting with the 140.1 nm emissivity, and in the right column of panels are the electron densities from the peak contribution function of the 140.1 nm line.

function is wide. We have a contribution to the intensity from different heights along the column, from a wide range in electron densities, so the contribution to the intensity comes from several non-uniform electron density slabs along the column we investigate. Therefore, the resulting electron density from the intensity ratio cannot be the electron density from where the contribution function peaks.

We have investigated the weighted mean averaged electron densities from our synthetic atmosphere by using the emissivities of the 140.1 nm and 140.4 nm lines as weights for the electron density from the simulation. The resulting weighted mean electron densities are very similar to the one derived from the line ratio and reproduce the NEQ results when NEQ emissivities are used as weights, as well as the SE results for SE emissivity weights. This consistency is due to the fact that the NEQ effects do not disappear in the averaging of the electron density along each column due to the weighting by the NEQ emissivities. However, in NEQ, there is a slight difference in the derived electron densities when the 140.1 nm emissivity is used as weights compared to when the 140.4 nm emissivity is used, due to NEQ effects of the different O IV levels involved in the transitions forming the spectral lines, but this difference is less than a factor of two.

In the middle column of panels in Figure 13, we have plotted PDFs of the weighted mean averaged electron densities derived using the 140.1 nm emissivity as a weight, as a function of the electron density at $\log T\,[\mathrm{K}] = 5.15$. By comparing the PDFs plotted in Figure 13, we can conclude that the best explanation for the electron density derived using line ratio diagnostics is a weighted mean electron density of the particular spectral lines involved in the ratio. We interpret this as the electron density where the intensity emerges from, and it is not related to a particular temperature, as the emissivity ratio states.

With the advanced, highly realistic solar atmosphere model Bifrost, we have access to a synthetic solar atmosphere, which makes it possible to study the solar atmosphere as a whole, from the photosphere to the corona, giving us an appropriate tool to understand the emerging emission throughout the line of sight. This makes it possible to test diagnostics techniques and studies of emerging emission.

This study shows that numerical modeling is essential to electron density diagnostics and is a valuable tool when the ions used for such studies are expected to be out of ionization equilibrium. Even though the study has been performed on the O IV ion, similar results are expected for other transition region ions as well.

With the results in mind, we advise to move away from the understanding that the results of electron density diagnostics give information of the electron density at a particular

temperature. This technique of line ratio analyses for electron density diagnostics is not related to the temperature: rather, it gives information about the electron density of the region where the emission emerge from.

If the lines used for line ratio diagnostics are out of ionization equilibrium, such as the O IV 140.1 nm and 140.4 nm used here, then the resulting electron density would not be the electron density at a specific temperature. The method therefore cannot be used when the spectral lines are out of ionization equilibrium. This can be avoided by choosing spectral lines that are in SE for the line ratio diagnostics. In SE, the ions are in equilibrium with their environment. The emission emerging from these ions can therefore give direct information about the local electron density and temperature, and the method of line ratio diagnostics results in the electron density at the temperature of interest. By carefully investigating the ionization times and recombination times of the ions in advance, and finding these times to be sufficiently lower than the dynamic timescales of the region of formation in the solar atmosphere, one can make sure that the ions forming the spectral lines are in SE. This is the only way one can diagnose the electron density at a particular temperature.

REFERENCES

Aschwanden, M. J. 2004, Physics of the Solar Corona. An Introduction (Chichester: Praxis Publishing Ltd.)

Bryans, P., Badnell, N. R., Gorczyca, T. W., et al. 2006, ApJS, 167, 343

Carlsson, M., & Leenaarts, J. 2012, A&A, 539, A39

Culhane, J. L., Harra, L. K., James, A. M., et al. 2007, SoPh, 243, 19

Dere, K. P., Landi, E., Young, P. R., et al. 2009, A&A, 498, 915

Doyle, J. G., Giunta, A., Singh, A., et al. 2012, SoPh, 280, 111

Feldman, U. 1992, ApJ, 385, 758

Feldman, U., Laming, J. M., Mandelbaum, P., Goldstein, W. H., & Osterheld, A. 1992, ApJ, 398, 692

Feldman, U., Landi, E., & Doschek, G. A. 2008, ApJ, 679, 843

Flower, D. R., & Nussbaumer, H. 1975, A&A, 45, 145

Gabriel, A. H., & Jordan, C. 1972, in Case Studies in Atomic Collision Physics Vol. 2, ed. E. McDaniel & M. R. C. McDowell (Amsterdam: North-Holland), 209

Gudiksen, B. V., Carlsson, M., Hansteen, V. H., et al. 2011, A&A, 531, A154

Hansteen, V. H., & Gudiksen, B. 2005, in ESA Special Publication, Vol. 592; Solar Wind 11/SOHO 16, Connecting Sun and Heliosphere, ed. B. Fleck, T. H. Zurbuchen, & H. Lacoste (Noordwijk: ESA), 483

Judge, P. G., & Meisner, R. W. 1994, in Solar Dynamic Phenomena and Solar Wind Consequences, the Third SOHO Workshop, ed. J. J. Hunt (ESA Special Publication, Vol. 373; Noordwijk: ESA), 67

Keenan, F. P., Crockett, P. J., Aggarwal, K. M., Jess, D. B., & Mathioudakis, M. 2009, A&A, 495, 359

Landi, E., Del Zanna, G., Young, P. R., et al. 2006, ApJS, 162, 261

Loulergue, M., & Nussbaumer, H. 1974, A&A, 34, 225

Magain, P. 1986, A&A, 163, 135

Mason, H. E., & Fossi, B. C. M. 1994, A&ARv, 6, 123

Munro, R. H., Dupree, A. K., & Withbroe, G. L. 1971, SoPh, 19, 347

Nordlund, A. 1982, A&A, 107, 1

Nussbaumer, H., & Storey, P. J. 1982, A&A, 115, 205

Olluri, K., Gudiksen, B. V., & Hansteen, V. H. 2013, AJ, 145, 72

Ralchenko, Y. 2005, MSAIS, 8, 96

Raymond, J. C., & Dupree, A. K. 1978, ApJ, 222, 379

Skartlien, R. 2000, ApJ, 536, 465

Paper III

Synthesized spectra of optically thin emission lines produced by the Bifrost stellar atmosphere code, including non equilibrium ionization effects: A study of the intensity, non-thermal linewidths and Doppler shifts

Olluri, K., Gudiksen, B. V., Hansteen, V. and De Pontieu, B.

Submitted to ApJ (2013)
